3-22-2018

Control, Characterization, and Cooling of an Ultra-Compact Combustor

Kevin J. DeMarco

Control, Characterization, and Cooling of an Ultra-Compact Combustor

THESIS

Kevin J. DeMarco, Second Lieutenant, USAF

AFIT-ENY-MS-18-M-250

DEPARTMENT OF THE AIR FORCE
AIR UNIVERSITY

AIR FORCE INSTITUTE OF TECHNOLOGY

Wright-Patterson Air Force Base, Ohio

AFIT-ENY-MS-18-M-250

CONTROL, CHARACTERIZATION, AND COOLING OF AN ULTRA-COMPACT COMBUSTOR

THESIS

Presented to the Faculty

Department of Aeronautics and Astronautics

Graduate School of Engineering and Management

Air Force Institute of Technology

Air University

Air Education and Training Command

in Partial Fulfillment of the Requirements for the

Degree of Degree of Master of Science

Kevin J. DeMarco, BS

Second Lieutenant, USAF

March 2018

AFIT-ENY-MS-18-M-250

CONTROL, CHARACTERIZATION, AND COOLING OF AN ULTRA-COMPACT COMBUSTOR

Kevin J. DeMarco, BS
Second Lieutenant, USAF

Committee Membership:

Marc D. Polanka, PhD
Chairman

Mark F. Reeder, PhD
Member

Major Levi Thomas, PhD
Member

Abstract

An Ultra-Compact Combustor (UCC) is novel alternative to axial flow combustors commonly used in gas turbine engines. The UCC offers multiple benefits to engine design. First, the UCC aims to increase the thrust-to-weight ratio of an aircraft gas turbine engine by decreasing the size, and thus weight, of the engine's combustor. This is done by utilizing a Circumferential Cavity (CC) wrapped around the main core flow which hosts the combustion event, allowing a shortened combustor length. Second, within the CC, the combusting mixture is subjected to a high centrifugal loading which aids combustion by improving both flame propagation and residence time. Finally, the architecture of the UCC allows a unique cooling scheme to be employed for the Hybrid Guide Vane (HGV). The primary objective of this research was to obtain improved performance of the combustor via improved control over the flow splits and distribution within the combustor. The combustion dynamics were investigated both computationally and experimentally to find the design space were successful operation was established. The secondary objective was to design a film cooled HGV by controlling the mainstream flow and directing a portion of it into the vane.

Combustor performance was improved by redesigning the outer ring and back plate to improve control of the fuel and air injection and subsequent mixing with the goal of maximizing the fuel burned within the CC. Evaluations using Computational Fluid Dynamics (CFD) were implemented to help guide the design and understand the combustion dynamics. The outer ring and back plate were then manufactured and tested to compare with the original design. These components allowed a new level of control over the UCC never before examined which was then characterized

by developing an operating profile for the various controllable aspects. The redesign and unprecedented controllability allowed the UCC to operate at previously unobtainable equivalence ratios and produce a nominal 15% increase in exit temperatures. Similarly, CFD was utilized to guide the design of a film cooled HGV which drew in compressor air at the stagnation region of the airfoil as the coolant. Using CFD the effects of the required internal supports on flow dynamics and cooling effectiveness were explored. The final manufactured HGV was then prepared for future experimental testing and evaluation.

Acknowledgements

I would first like to thank my advisor, Dr. Marc Polanka, for all his guidance, having the patience to deal with me, and of course the many hours of reviewing the countless versions of my papers. Thank you for providing me with the opportunity to contribute to this research project.

I would like to thank Maj. Bohan for taking the extra time in the lab to help me finish a test, teach me CFD, or discuss ideas. Thank you for being willing to stay after hours as well as give me advice over the past year. He was not just a partner in the lab, but a mentor and friend.

I would like to thank both Dr. Chiping Li at the Air Force Office of Scientific Research and Dr. Drew Caswell at the Air Force Research Lab for sponsoring my research. Their contributions have allowed the AFIT UCC to conduct research which is both state of the art and novel.

I would like to thank the AFIT model shop and AniMaL Lab teams for manufacturing countless components for the UCC. Without the guidance and support from both teams none of the research presented in this paper would have been possible.

I would also like to thank my parents, Kevin and Kim DeMarco, for their continuous support. They have always provided me with the best opportunities and motivated me to always do my best. I would not be where I am today without their guidance.

Finally, I would like to thank my fiancée, Jen McBrine, for putting up with my stress and stubbornness while keeping me motivated and optimistic. I appreciate all the sacrifices she has made for me and my education.

Kevin J. DeMarco

Table of Contents

Page

Abstract iv

Acknowledgements vi

List of Figures ix

List of Tables xiv

List of Abbreviations xv

List of Symbols xvi

I. Introduction 1

1.1 Research Objectives 2

II. Background 5

2.1 Fundamentals of Combustion 5
2.2 Compact Combustors 8
2.2.1 G-Loading Effects on Combustion 11
2.3 Flame Stabilization 15
2.4 Film Cooling 18
2.5 Additive Manufacturing 21
2.6 Infrared Thermography 22
2.7 Particle Imaging Velocimetry 25

III. Baseline UCC Design 27

3.1 Facilities 27
3.2 Test Rig 30
3.3 Operation 39
3.4 Repeatability 41
3.5 Baseline Results 45

IV. Circumferential Cavity Redesign 52

4.1 6-Step Ring 52
4.1.1 CFD Evaluation 55
4.1.2 Experimental Results 56
4.2 12-Step Ring 59
4.2.1 CFD Evaluation 61
4.2.2 Comparison to Baseline Design 63
4.2.3 Fuel and Airflow Split Study 70

Page

4.3 Back Plate Injection 79
4.3.1 Experimental Results 81

V. UCC Film Cooling 92

5.1 Design and Manufacturing 93
5.2 Film Cooling Design CFD Evaluation 100
5.2.1 CFD Setup and Settings 101
5.2.2 CFD Results 105
5.3 Experimental Setup 113

VI. Conclusions 116

6.1 Cavity Redesign Conclusions and Recommendations 116
6.2 UCC Control Conclusions and Recommendations 118
6.3 Film Cooling Conclusions and Recommendations 120

Appendix A. IR Thermography Correlation Code 123

Bibliography 135

List of Figures

Figure		Page
1.	UCC and Traditional Combustor Length Comparison	1
2.	TVC and HGC Schematics	8
3.	TVC Geometry	10
4.	HGC Geometry	10
5.	Observed Flame Speed Compared to Centrifugal Force	11
6.	Bubble Transport Theory	12
7.	Instantaneous Temperature Contours at Various Centrifugal Loadings	14
8.	Equivalence Ratio at Blowout as a Function of Centrifugal Loading	15
9.	Vee Gutter Flow Schematic	16
10.	Channel Designs Tested by Lapsa and Dahm	17
11.	Backward Facing Step Shadographs	18
12.	Film Cooling Schematic	19
13.	Selective Laser Sintering Technique	22
14.	PIV Setup	26
15.	PIV Post-Processing	26
16.	COAL Lab UCC	27
17.	Fuel Flow Controllers	29
18.	UCC Exhaust Box	29
19.	AFIT UCC Cross-section	30
20.	Variable Diffuser Design	31
21.	Variable Diffuser Actuation System	32

Figure Page

22. Original UCC Cavity Injection Parts 34

23. Fuel Buildup on CC Outer Diameter 35

24. Original UCC Back Plate 35

25. Original UCC HGV With Tail Cone 36

26. UCC HGV Position and Dimensions 37

27. UCC Cavity and Exit Plane Thermocouples 37

28. Thermocouple Rake Radial Positions 38

29. UCC Control Station 40

30. 7.62 cm Air Line Fluctuation 42

31. 3.81 cm Air Line Fluctuation 43

32. Total Air and Average Cavity Temperature Fluctuations 44

33. Baseline $\frac{1}{2}$ Cavity CFD Generated Contours 47

34. Baseline Average Cavity Temperature vs. Total Air Mass Flow 48

35. Baseline Experimental Exit Temperature Profiles 51

36. 6-Step UCC Cavity Outer Ring 53

37. 6-Step Ring Dimensions 54

38. 6-Step Ring Print Error 55

39. 6-Step Ring $\frac{1}{2}$ Cavity Tangential Velocity Contours 56

40. 6-Step PIV Schematic 57

41. 6-Step PIV Setup and Equipment 58

42. 6-Step $\frac{1}{2}$ Cavity CFD Contours 59

43. 12-Step UCC Cavity Outer Ring 60

44. 12-Step Ring Dimensions 61

Figure Page

45. 12-Step Ring $\frac{1}{2}$ Cavity Tangential Velocity Contours 62

46. 12-Step Ring $\frac{1}{2}$ Cavity Temperature Contours 63

47. Average Cavity Temperature vs. Cavity Equivalence Ratio 65

48. $\frac{1}{2}$ Cavity Temperature vs. Total Air Mass Flow 66

49. 12-Step Design Exit Temperature Profiles Compared to Baseline 69

50. 12-Step Fuel Split Evaluation Plot 72

51. Required Pressure Differential Map, $\dot{m}_{in} = 0.108kg/s$ 75

52. Average Exit Temperature Operating Map, $\dot{m}_{in} = 0.108kg/s$ 75

53. Required Pressure Differential Map, $\dot{m}_{in} = 0.060kg/s$ 77

54. Required Pressure Differential Map, $\dot{m}_{in} = 0.120kg/s$ 77

55. Average Exit Temperature Operating Map, $\dot{m}_{in} = 0.060kg/s$ 78

56. Average Exit Temperature Operating Map, $\dot{m}_{in} = 0.120kg/s$ 78

57. Redesigned UCC Back Plate With Fuel Injectors 80

58. Case 2 Average Exit Temperatures 10% Back Plate Fuel, $\dot{m}_{in} = 0.108kg/s$ 83

59. Case 3 Average Exit Temperatures 20% Back Plate Fuel, $\dot{m}_{in} = 0.108kg/s$ 83

60. Case 4 Average Exit Temperatures 30% Back Plate Fuel, $\dot{m}_{in} = 0.108kg/s$ 84

61. Case 6 Average Exit Temperatures 10% Back Plate Fuel, $\dot{m}_{in} = 0.108kg/s$ 85

62. Case 7 Average Exit Temperatures 20% Back Plate Fuel, $\dot{m}_{in} = 0.060kg/s$ 85

Figure Page

63. Case 8 Average Exit Temperatures 30% Back Plate Fuel, $\dot{m}_{in} = 0.060kg/s$ 86

64. Case 10 Average Exit Temperatures 10% Back Plate Fuel, $\dot{m}_{in} = 0.120kg/s$ 87

65. Case 11 Average Exit Temperatures 20% Back Plate Fuel, $\dot{m}_{in} = 0.120kg/s$ 88

66. Case 12 Average Exit Temperatures 30% Back Plate Fuel, $\dot{m}_{in} = 0.120kg/s$ 88

67. Average Exit Temperature Full Back Plate Operating Map, $\dot{m}_{in} = 0.108kg/s$ 90

68. Average Exit Temperature Full Back Plate Operating Map, $\dot{m}_{in} = 0.060kg/s$ 90

69. Average Exit Temperature Full Back Plate Operating Map, $\dot{m}_{in} = 0.120kg/s$ 91

70. Cross-Section of UCC Showing HGV Location 92

71. Vane Surface Pressure Distributions 93

72. Internal Vane Structure 94

73. Cooling Hole Locations 95

74. First HGV Internal Structure Design 96

75. Rectangular Internal Support Design 97

76. Circular Internal Support Design 98

77. HGV Printing Problem 99

78. Additively Manufactured HGV With Cooling Schemes 100

79. HGV CFD Test Domain 101

80. HGV CFD Grid 102

81. Surface Pressure Distributions 106

82. Vane Overall Effectiveness Contours For Each Case 108

Figure Page

83. Vane Overall Effectiveness Contour For Case 4 110

84. Vane Heat Flux Contours 112

85. Coolant Hole Effects on Heat Flux Contours 112

86. HGV Instrumentation Ports 114

87. IR Thermography Setup 115

88. IR Correlation Code Save Folder 123

89. File For Surface Thermocouple Locations 123

90. File For Surface Thermocouple Temperatures 124

91. Selecting The First IR File 127

92. IR Correlation Curve 131

93. Output Profiles 134

94. Output Files 134

List of Tables

Table		Page
1.	Cavity Temperatures for Repeated Cases	44
2.	Baseline Test Cases	45
3.	Baseline Cavity Temperatures	48
4.	Baseline Exit Properties	49
5.	12-Step Ring Test Cases	64
6.	Exit Temperature Profile Characteristics	67
7.	12-Step Fuel Split Evaluation Cases	71
8.	12-Step Airflow Split Test Points	74
9.	Back Plate Fuel Injection Cases	81
10.	HGV Cooling Schemes by Vane	94
11.	HGV CFD Cases	101
12.	HGV CFD Inlet Boundary Conditions	104
13.	Coolant Hole Blowing Ratios	107
14.	Cooling Configuration Impact	111

List of Abbreviations

Abbreviation		Page
AFIT	Air Force Institute of Technology	1
UCC	Ultra-Compact Combustor	1
HGV	Hybrid Guide Vane	3
AFRL	Air Force Research Lab	5
CFD	Computational Fluid Dynamics	5
TVC	Trapped Vortex Combustor	8
HGC	High-G Combustor	8
CC	Circumferential Cavity	9
IR	Infrared	22
PIV	Particle Imaging Velocimetry	25
COAL	Combustion Optimization and Analysis Laser	27
SST	Shear Stress Transport	45
FGM	Flamelet Generated Manifold	46
GRI	Gas Research Institute	46
PDF	Probability Distribution Function	46

List of Symbols

Symbol		Page
ϕ	Equivalence Ratio	5
$\dot{m}_f/\dot{m}_a$	Fuel to Air Ratio	5
MW	Molecular Weight	6
S_L	Turbulent Flame Speed	6
α	Thermal Diffusivity	7
$\dot{m}_a/\dot{m}_f$	Air to Fuel Ratio	7
$\bar{\dot{m}}'''_F$	Average Volumetric Mass Production Rate	7
ρ_u	Unburned Gas Density	7
S_T	Turbulent Flame Speed	7
$\dot{m}$	Mass Flow Rate	7
$\bar{A}$	Time Averaged Flame Surface Area	7
u'_{rms}	Root Mean Squared Velocity Fluctuation	7
τ_r	Residence Time	8
g	Gravitational Acceleration, 9.82 m/s^2	12
S_B	Bubble Velocity	13
F_c	Centrifugal Force	13
T_s	Surface Temperature	19
T_∞	Freestream Temperature	19
T_{ci}	Coolant Temperature	19
ϕ_{eff}	Overall Effectiveness	19
R_{cond}	Conductive Resistance	20
t	Material Thickness	20

Symbol		Page
k_{cond}	Thermal Conductivity	20
A	Area	20
R_{conv}	Convective Resistance	20
h_{conv}	Convective Heat Transfer Coefficient	20
Bi	Biot Number	20
$E_{b\lambda}$	Spectral Blackbody Emissive Power	23
h	Planck's Constant, $6.626 \cdot 10^{-34}$ J·s	23
c_0	Speed of Light in a Vacuum, $2.998 \cdot 10^{8}$ m/s	23
λ	Wavelength	23
k	Blotzmann's Constant, $1.381 \cdot 10^{-23}$ J/K	23
T	Temperature	23
ϵ	Emissivity	23
$\dot{m}_{core}$	Core Air Mass Flow Rate	32
$\overline{U}_{core}$	Average Core Velocity	32
ρ	Density	32
U	Velocity	33
U_τ	Friction Velocity	33
κ	Von Kármán Constant	33
y	Height	33
ν	Kinematic Viscosity	33
ΔP	Pressure Differential	33
T_{max}	Maximum Temperature	39
T_{avg}	Average Temperature	39
T_{in}	Inlet Air Temperature	39

Symbol		Page
$\dot{m}_{in}$	Total Air Mass Flow Rate	45
ϕ_{cav}	Cavity Equivalence Ratio	45
ϕ_{Global}	Global Equivalence Ratio	45
$\dot{m}_{cav}$	Cavity Air Mass Flow Rate	45
$\dot{m}_f$	Fuel Mass Flow Rate	45
r	Radius	46
V_{tan}	Tangential Velocity	46
ρ_c	Coolant Density	107
V_c	Coolant Velocity	107
ρ_∞	Freestream Density	107
V_∞	Freestream Velocity	107

CONTROL, CHARACTERIZATION, AND COOLING
OF AN ULTRA-COMPACT COMBUSTOR

I. Introduction

In the aerospace industry weight is gold; therefore aircraft gas turbine engines are assessed by their thrust-to-weight ratio. Most engineers work to improve this ratio by increasing the thrust of the engine. However, another way to increase thrust-to-weight is by reducing the weight of the engine. The Air Force Institute of Technology (AFIT) has been investigating means to accomplish this by replacing the traditional axial combustor with an Ultra-Compact Combustor (UCC). A UCC reduces the engine weight by decreasing the length of the combustor as shown in Figure 1. This is accomplished by burning inside the combustor circumferentially instead of axially. In an axial combustor the residence time is achieved by having a combustor long enough to contain the flame.

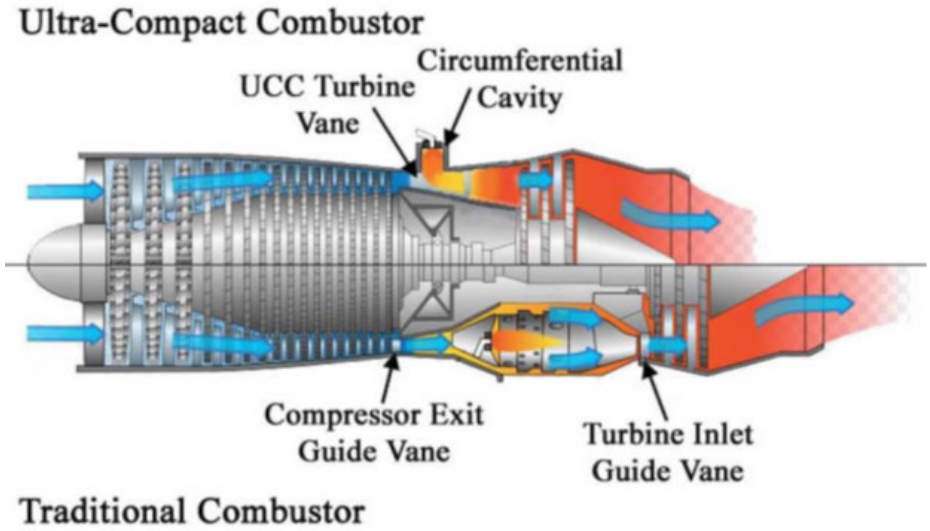

Figure 1. UCC and Traditional Combustor Length Comparison [1]

Burning circumferentially in the UCC means the combustor is not limited by the flame length as the path the fuel is burning is circular, and thus could arguably be modeled as infinite in length. The circumferential burning also creates a centripetal acceleration, and thus a centrifugal loading on the burning fuel-air mixture. The centrifugal loading causes buoyancy forces on the mixture where the heavier reactants are forced to the outside of the combustion cavity while the lighter products migrate toward the center and exit the circumferential cavity. According to Lewis [2, 3] and Briones [4] the increased centrifugal loading created an increase in the flame propagation rate.

Current UCC designs, such as the design by Cottle [5], have been successful in burning in a circumferential cavity. While the flow had a bulk tangential velocity, the velocity was not high enough to generate a centrifugal loading which fully gained the increased flame propagation benefits. Tests to increase the centrifugal loading using higher air flow rates resulted in flame stabilization problems. Another limitation of the current UCC design is operating at high equivalence ratios. The flow dynamics within the cavity were inadequate at mixing the air and fuel at high equivalence ratios. This resulted in a build up of fuel along the outer diameter of the circumferential cavity and a reduction in combustor performance.

1.1 Research Objectives

The first objective of this research was to increase the centrifugal loading within the circumferential cavity which would improve the the flame propagation benefits that the UCC utilizes. The centrifugal loading within the circumferential cavity is dictated by the radius and tangential velocity of the cavity. For the UCC the cavity radius is fixed, therefore the only way to increase the centrifugal loading is to increase the tangential velocity within the cavity. One mechanism to accomplish this

is to increase the injection velocity of the air and fuel. However, increasing this value too far results in the primary combustion zone being pushed outside the cavity or blowing out the flame all together. An alternative is to modify the geometry of the circumferential cavity in a way that the cavity centrifugal loading can be increased while the primary combustion zone remains within the circumferential cavity over a wide range of equivalence ratios.

The second objective was characterizing the control that the redesigned circumferential cavity introduced by developing an operating profile. Turbine engine components require a combustor that can operate over a wide throttle range at high efficiency. The engine is then targeted to operate such that the engine operates mainly in regions of high efficiency. Thus, evaluation of the effects of different UCC control parameters is necessary to establish the combustor's performance over a range of conditions. The UCC operating map would indicate the combustor's flameout limits, control limits, and preferred flow conditions during operation.

The final objective was to manufacture a film cooled hybrid guide vane (HGV) for integration into the UCC. In gas turbine engines the combustor operates at pressures above atmospheric resulting in temperatures which are hot enough to melt the downstream vanes. To enable a UCC to operate at engine pressures, a film cooled version of the HGV needs to be designed and manufactured. The UCC geometry allow this film cooling scheme to be unique in that the coolant flow does not need to be ducted around the combustor, but instead it is ingested through the HGV stagnation regions. Control of this flow within the vane is critical to achieve the maximum cooling effectiveness.

The next five chapters detail the support and progress of completing these three objectives. First, Chapter II covers the necessary background and literature guiding this research. Chapter III discusses the design and performance of the previously

existing UCC test rig. Subsequently, Chapter IV discusses the redesign of UCC components and characterization of the performance and controls of this new design. Chapter V discusses the design, manufacturing, and implementation of a film cooled HGV. Finally, Chapter VI summarizes the results for all three objectives and suggest areas of future research.

II. Background

As discussed in Chapter 1 a major goal of aircraft engine design is to reduce weight, and a UCC is one solution to achieve this objective. Therefore, the Air Force Research Lab (AFRL) and AFIT have studied UCC technology extensively for over a decade. Multiple design iterations of the test rig based on previous research and computational fluid dynamics (CFD) results have been completed resulting in the current full annular UCC test rig. The current work on the UCC includes improving the fuel distribution within the combustion cavity at fuel rich equivalence ratios, modifying the combustor's geometry to maintain the primary zone within the combustion cavity over a wide range of equivalence ratios, and incorporating film cooling into the HGV of the UCC. This next iteration of improvements to the UCC requires an understanding of fundamentals of combustion, compact combustors, flame stabilization, film cooling, and infrared thermography. This chapter focuses on previous research related to these topics in Sections 2.1, 2.2, 2.3, 2.4, and 2.6 respectively, establishing the knowledge base for fuel distribution, combustion cavity development, and film cooling integration in the UCC.

2.1 Fundamentals of Combustion

Traditional jet engine combustors are axial and their design is based on fundamental combustion principles to burn a given amount of fuel within the combustor length. These fundamental parameters include equivalence ratio, residence time, flame speed, and flame length. Equivalence ratio, ϕ, is calculated through Equation 1 and characterizes the combustion as either rich, lean, or stoichiometric. Fuel rich combustion, $\phi > 1$, indicates that the fuel to air ratio, $(\dot{m}_f/\dot{m}_a)$, is higher than the stoichiometric fuel to air ratio, $(\dot{m}_f/\dot{m}_a)_{stoic}$. Fuel lean combustion, $\phi < 1$, indicates that the

fuel to air ratio is lower than the stoichiometric fuel to air ratio. And stoichiometric combustion, $\phi = 1$, indicates that the fuel to air ratio is at stoichiometric.

$$\phi = \frac{\left(\frac{\dot{m}_f}{\dot{m}_a}\right)}{\left(\frac{\dot{m}_f}{\dot{m}_a}\right)_{stoic}} \tag{1}$$

The stoichiometric ratio is specific to the fuel and determined by balancing the fuel and air chemical reaction. Thus stoichiometric combustion ideally results in all the reactants being burned resulting in the highest temperature. Equation 2 shows the ideal general hydocarbon chemical equation from Turns [6]. Using the molecular weight, (MW), of the fuel and air, $(\dot{m}_f/\dot{m}_a)_{stoic}$ can be found using Equation 4 meaning $(\dot{m}_f/\dot{m}_a)_{stoic}$ is only a function of the fuel used.

$$C_xH_y + a(O_2 + 3.76N_2) \Longrightarrow xCO_2 + \left(\frac{y}{2}\right)H_2O + 3.76N_2 \tag{2}$$

$$a = x + \frac{y}{4} \tag{3}$$

$$\left(\frac{\dot{m}_f}{\dot{m}_a}\right)_{stoic} = 4.76a\frac{MW_{air}}{MW_{fuel}} \tag{4}$$

Lean and rich combustion results in nonreacted oxygen or fuel respectively. Both result in lower temperatures than stoichiometric combustion, however most traditional jet engines operate mainly at lean equivalence ratios. This is done to assure combustion is completed within the combustor and does not extend into the first stage of the turbine [7].

Flame speed is a key component to flame stability as it dictates blowoff. There are two types of flame speeds, laminar and turbulent. A laminar flame speed, S_L, occurs in laminar flames, such as a candle or a bunsen burner. This is the velocity at which a laminar flame propagates through a fuel-air mixture, which is specific to the

fuel. Laminar flame speed is defined by Equation 5 where α is the thermal diffusivity, $(\dot{m}_a/\dot{m}_f)$ is the air to fuel ratio, $\bar{\dot{m}}'''_F$ is the average volmetric mass production rate, and ρ_u is the unburned gas density. However, the inside of a jet engine combustor is a turbulent environment with high mixing and flow velocity gradients. This causes the flame in this region to propagate at its turbulent flame speed. Turns [6] defines turbulent flame speed, S_T, as "the velocity at which unburned mixture enters the flame zone in a direction normal to the flame". The turbulent flame speed is therefore dependent on the surface area of the flame and is defined in its most basic form with Equation 6 where $\dot{m}$ is the reactant mass flow rate and $\bar{A}$ is the time averaged surface area of the flame. The flame surface area is difficult to quantify as it is wrinkled and distorted from the turbulence within the flow. However, the turbulent flame speed can be related to the laminar flame speed using Equation 7 if the root mean squared of the velocity fluctuation of the flow, u'_{rms}, is known [6].

$$S_L = \sqrt{-2\alpha\left(\frac{\dot{m}_a}{\dot{m}_f} + 1\right)\frac{\bar{\dot{m}}'''_F}{\rho_u}} \tag{5}$$

$$S_T = \frac{\dot{m}}{\bar{A}\rho_u} \tag{6}$$

$$S_T = 3.5 S_L \left(\frac{u'_{rms}}{S_L}\right)^{0.7} \tag{7}$$

Flame length is important for combustor design as the flame needs to remain within the combustion chamber or risk damaging turbine components. The flame length is ultimately the axial distance between the flame base and the furthest stoichiometric location within the flame. According to Turns [6], this distance is dependent on the momentum flux of the injected fuel, the density of the injected fuel, the diameter of the injector port, and the stoichiometry of the fuel. A combustor must be designed with an axial length that contains the flame over a range of the

aforementioned parameters. However, it is important to note that flame length is not the only factor that drives the combustor length. The combustor must provide enough time for the fuel and air to mix and then react to completion. This time is referred to as residence time, τ_r, and is the time that the reactants are within the combustion chamber. The higher the residence time, the more complete the reaction. Therefore, traditional combustors must be long to provide high residence times for complete combustion.

2.2 Compact Combustors

Traditional combustors are designed such that the residence time allows for complete combustion. Therefore reducing the length outright would result in incomplete reactions entering the turbine. Two major designs which fundamentally change the combustor and allow the reduction of engine combustor size are the Trapped Vortex Combustor (TVC) and High-G Combustor (HGC), represented in Figure 2 (a) and 2 (b), respectively. A TVC uses a forebody and afterbody to generate and trap a vortex within which the combustion occurs. A representative TVC design is shown in Figure 3 by Hsu et al. [8]. The bulk air, left to right in Figure 3, flows past the forebody and along the outer diameter of the combustor. Within the cavity, fuel and air were injected from the afterbody opposite direction of the bulk air. This created

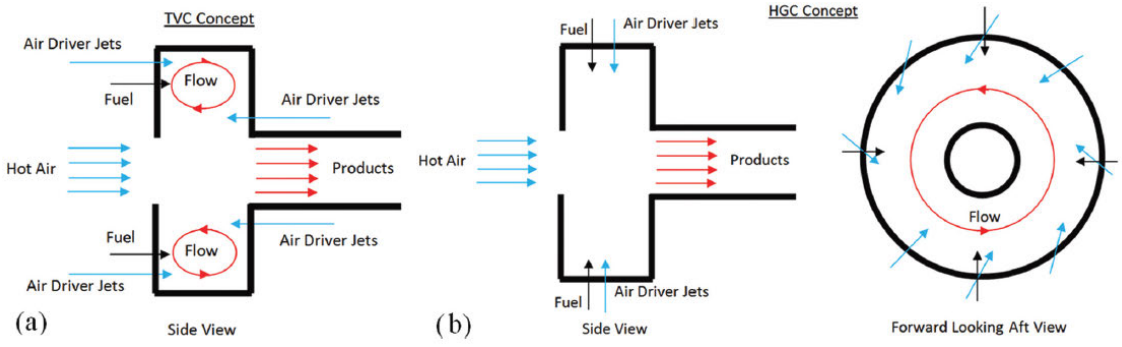

Figure 2. TVC (a) and HGC (b) Schematics [4]

a shear layer at the edge of the cavity and a recirculating region within the cavity. The aim of the TVC was to use this recirculating region, or trapped vortex, to both stabilize the flame and keep the primary combustion within the cavity.

A HGC relies on the principles developed by Lewis [2, 3] and uses centrifugal forces to apply a g-loading to the fuel-air mixture within a combustion cavity. Lewis theorized that the increased g-loading enhanced combustion and his work will be discussed in Section 2.2.1. This means that a HGC requires an increased g-loading on the combustion mixture, which was done by swirling the flow circumferentially. An example of a HGC is shown in Figure 4. Similar to the TVC, the HGC has bulk air traveling axially, left to right in Figure 4, and a separate flow that enters a recessed cavity, referred to as the Circumferential Cavity (CC). The air entering the CC is injected at an angle that promotes a tangentially dominated bulk flow velocity to create circumferential swirl, and thus a centrifugal loading on the mixture. The lighter reaction products then migrate toward the center of the cavity where they enter the core air flow and exit the combustor.

The HGC design also increases the residence time of the fuel within the CC. Normally residence time is dependent on the mixture velocity and the combustor length. Because the flow is traveling circumferentially the reactants experience an infinite length. The g-loading within the CC cause the heavier unburned gases to migrate to the outer diameter of the cavity while the less dense products are displaced toward the center where they exit the combustor. This means the unburned gases remain within the cavity until they are burned completely. Therefore, residence time for a HGC is theoretically independent on the mixture velocity and the combustor length, but dependent on the mass distribution of the mixture within the CC. In reality, especially at high equivalence ratios, as new reactants are injected into the cavity there becomes a buildup on the outer diameter which results in some unburned

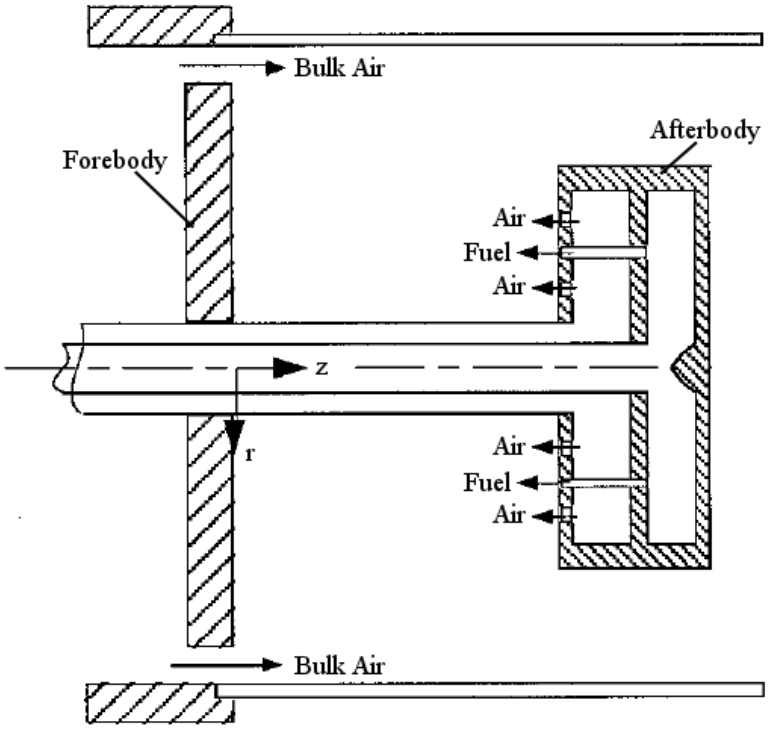

Figure 3. TVC Geometry (adapted from Hsu et al. [8])

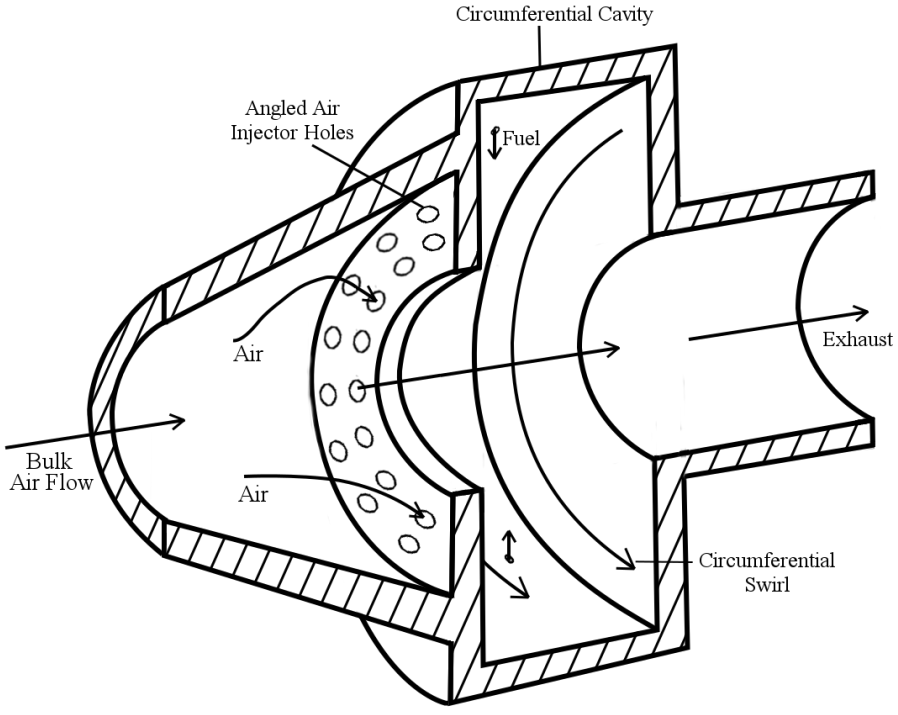

Figure 4. HGC Geometry

gases being pushed out of the cavity. This was seen in the study conducted by Cottle et al. [9] where not all the fuel was being burned even at lean equivalence ratios, discussed further in Chapter III, Section 3.2. However the fuel was still broken up and combustion started in a 25 mm axial length. Overall residence time is able to be maintained in HGC due to circumferential burning even though the axial length is shorter than a traditional combustor.

2.2.1 G-Loading Effects on Combustion.

The effects of centrifugal loading, or g-loading, on combustion was studied experimentally by Lewis [2, 3] and later computationally using CFD by Briones et al. [4]. Lewis [2, 3] conducted tests within a combustion centrifuge examining the effects of centrifugal forces on flame propagation. Using propane-air mixture, Lewis saw a trend between the flame-propagation rate and applied centrifugal force, shown in Figure 5.

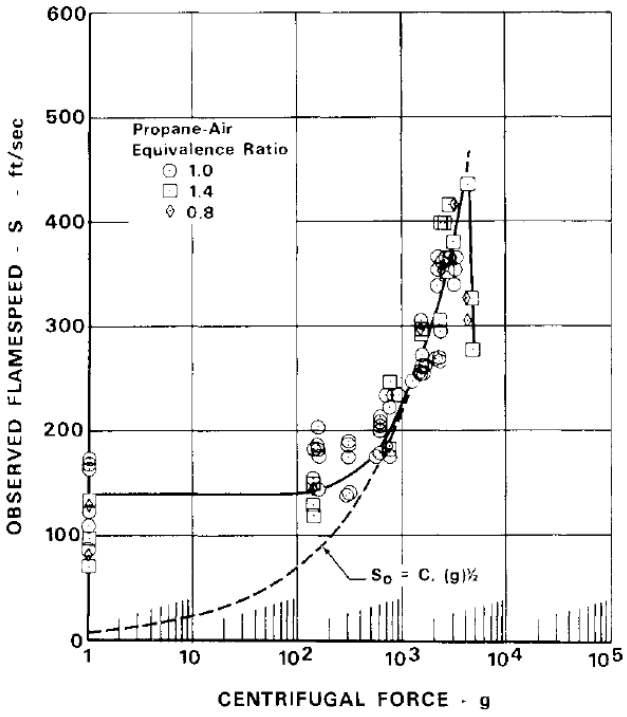

Figure 5. Observed Flame Speed Compared to Centrifugal Force [3]

Lewis noted that with a centrifugal force below 200 g's, where g is the acceleration due to gravity, there is no effect on the flame-propagation. However, at centrifugal forces above 500 g's the flame-propagation increased proportional to the square root of the centrifugal force. Then at 3500 g's the flame-propagation abruptly decreases until blowout. Lewis proposed the bubble transport theory to explain how the flame can propagate at a speed above its turbulent flame speed, a diagram of the theory is shown in Figure 6.

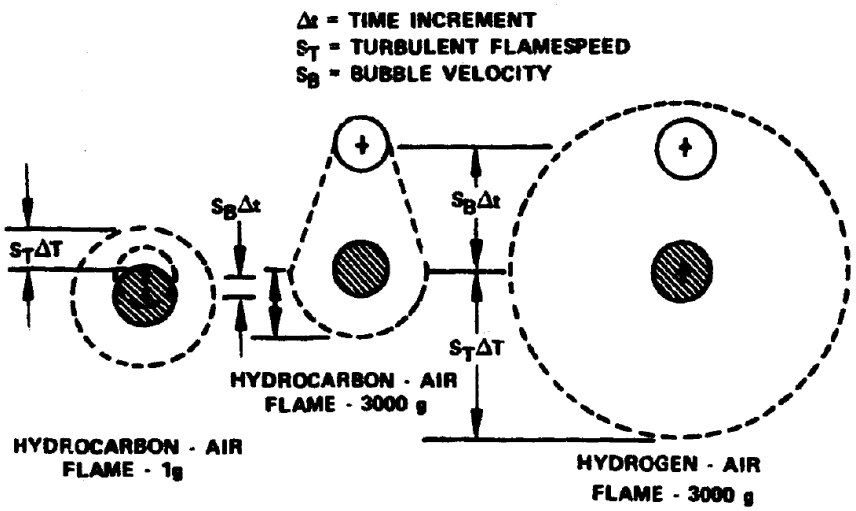

Figure 6. Bubble Transport Theory [2]

The cross-hatched circles are flame bubbles immersed in the fuel-air mixture, depicted by the dashed circles. Under normal flame conditions, indicated in the left diagram, the flame bubble stays within the fuel-air mixture while the flame progresses at its turbulent flame speed. Once a centrifugal force above 500 g's is added, the flame bubble progresses to the front of the fuel-air mixture, and advances the flame front as shown in the middle diagram, causing the flame to progress at the bubble velocity. In order to determine the bubble velocity, the bulk flow velocity due to the combustion expansion must be subtracted from the measured observed flame speed. Doing this for the data in Figure 5 resulted in a relationship between between bubble velocity,

S_B and centrifugal force, F_c, which Lewis approximated as Equation 8 when F_c was greater than 500 g's.

$$S_B = 1.25 F_c^{1/2} \tag{8}$$

However, if the turbulent flame speed is greater than the bubble velocity, the flame will appear unaffected by the centrifugal force and progress at the turbulent flame speed, as depicted in the right diagram. This means that the flame progression was dictated by the turbulent flame speed and bubble velocity, and the flame front progressed at the higher of the two.

Briones et al. [4] conducted a CFD study on the work done by Lewis [2, 3] and ultimately agreed with his findings in that flame propagation increases with centrifugal forces, however Briones theorized that this was done by a mechanism other than the bubble transport theory. Figure 7 shows the instantaneous temperature contours for centrifugal loadings of 1 g, 395 g's, 1000 g's, 2000 g's, and 3000 g's 8 ms after ignition. The flame front can be seen as the higher temperature region and has progressed further at higher centrifugal loadings, except the 3000 g's case, for the same amount of time, 8 ms. This indicates that the flame propagation velocity increased with centrifugal loading until a point where it decreased. Excluding the 3000 g's case, the flame front shapes are all similar with the fastest flame exhibiting a more corrugated flame structure as opposed to a wrinkled flame structure. The peak flame propagation velocity was determined to be at a centrifugal loading of 2500 g's. Above which the level of corrugation breaks up the flame causing the flame front to locally quench and slow down, which is shown in the 3000 g's case in Figure 7.

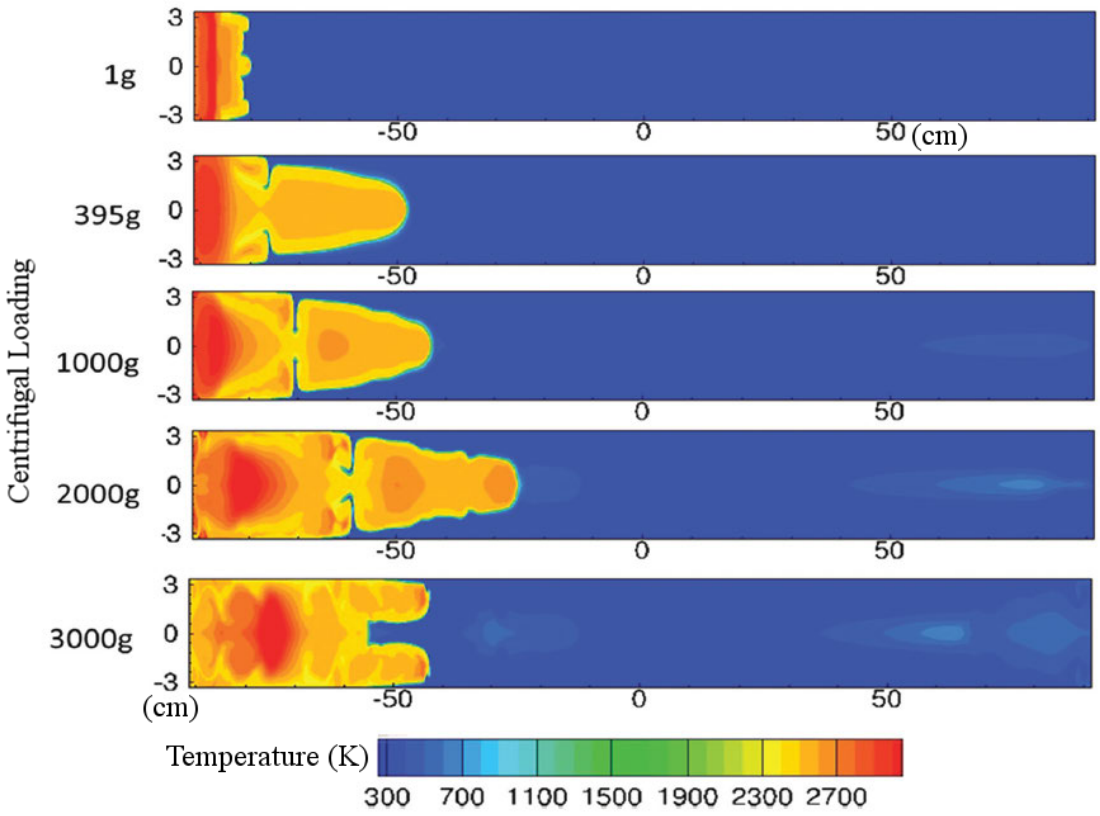

Figure 7. Instantaneous Temperature Contours at Various Circumferential Loadings [4]

While the increased flame propagation was explained by Lewis [2, 3] with the bubble transport theory discussed earlier in this section, Briones [4] explained it with increased Rayleigh-Taylor instabilities due to the centrifugal forces. It is important to note that although the explanations differ, the results of the studies conducted by both authors agree and show that flame propagation increases with centrifugal loading, which is the basis of a HGC design.

In an effort to confirm the centrifugal loading limit established by Lewis [2, 3], Zelina et al. [10] studied the centrifugal loading required to achieve blowout at various equivalence ratios. The results, represented in Figure 8, showed that lean blowout is dependent on the centrifugal loading and there exists a region in which a stable flame exists. The maximum centrifugal loading before blowout occurs near stoichiometric

conditions and is between 7000 g's to 8000 g's. This supports the data reported by Although Lewis [2, 3] reported an inflection point at 3500 g's, his data shown in Figure 5 supports blowout at a centrifugal loading around 8000 g's.

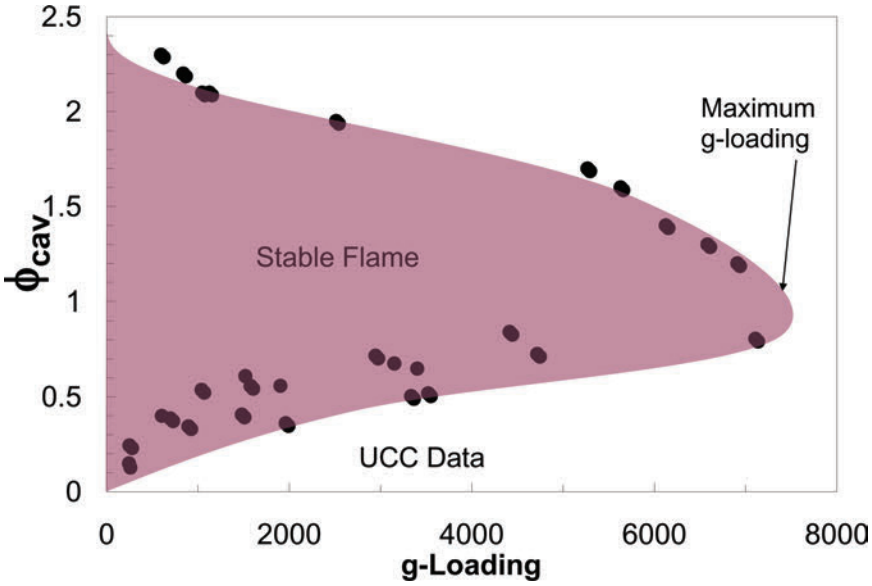

Figure 8. Equivalence Ratio at Blowout as a Function of Circumferential Loading [10]

2.3 Flame Stabilization

Flame stabilization is required for sustained combustion within a jet engine combustor. Common methods at producing flame stabilization is the use of bluff bodies inside the combustor or swirlers at the inlet of the combustor. These methods both anchor the flame at a desired point and allow the heat of the products to ignite the incoming reactants. Bluff bodies, such as vee gutters shown in Figure 9, create a recirculating region downstream of the body which acts as the flame anchor. Williams [11] noted that the hot reactants are brought into the recirculating region and act as a continuous ignition source for the incoming products. This means that the flame blows out when the ignited gases does not transfer enough heat back into the recirculating region to ignite the next volume of unburned mixture. Swirlers at

the combustor inlet create swirl within the incoming air flow which improves mixing between the fuel and air while acting as a flame stabilizer. Driscoll et al. [12] says the mixing improvement is due to the flame being lifted off the fuel injector which allows air to mix at the flame base. The flame stabilization established by swirl is due to the existance of an internal recirculating region with a low enough velocity to anchor a flame.

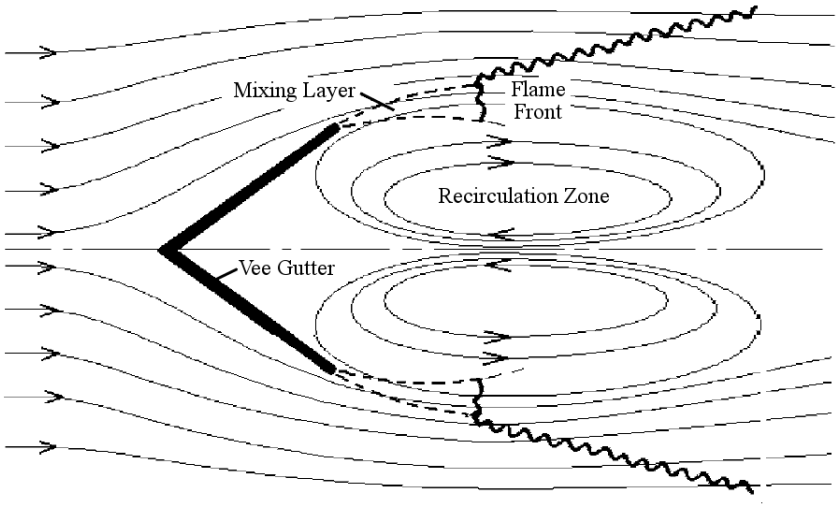

Figure 9. Vee Gutter Flow Schematic (adapted from Mattingly et al. [7])

Due to the geometry of the UCC the introduction of a bluff body within the CC or swirlers at the CC inlet would result in a reduction of cavity flow velocity. This is undesirable as a reduction in cavity flow velocity results in a reduction of centrifugal loading, however flame stabilization is still needed. Therefore an alternate method for establishing recirculating regions within the CC to act as flame anchors is required.

Lapsa and Dahm [13, 14] evaluated the novel approach of stabilizing a flame using a backward facing step. They set up three different channels, shown in Figure 10 and injected premixed fuel-air mixture from the left side of the channel and ignited the mixture within the step. The goal was to use the recirculating region developed by the step to anchor a flame. The geometry in Figure 10 (a) was used as a control

where the g-loading remained 1 g independent of flow velocity. Geometry (b) and (c) experienced different g-loadings, varying from 28.5 g's to 2850 g's, depending on the flow velocity. In all three geometries a recirculation region was established behind the steps, as shown in Figure 11. Geometry (b) experienced negative centrifugal forces which kept the reactants and products separated, minimizing any large scale turbulence. Therefore the mixing in Geometry (b) was drvien by the small turbulence structures. Geometry (c) experienced positive centrifugal forces which experienced centrifugal pumping. Lapsa and Dahm define centrifugal pumping as a region of mixing where the "reactants [are] being driven into the reaction zone and the products [are] being driven into the unreacted freestream" [14]. Centrifugal pumping caused vigorous mixing of the flow and increased with centrifugal force causing the flame to fully span the channel earlier upstream.

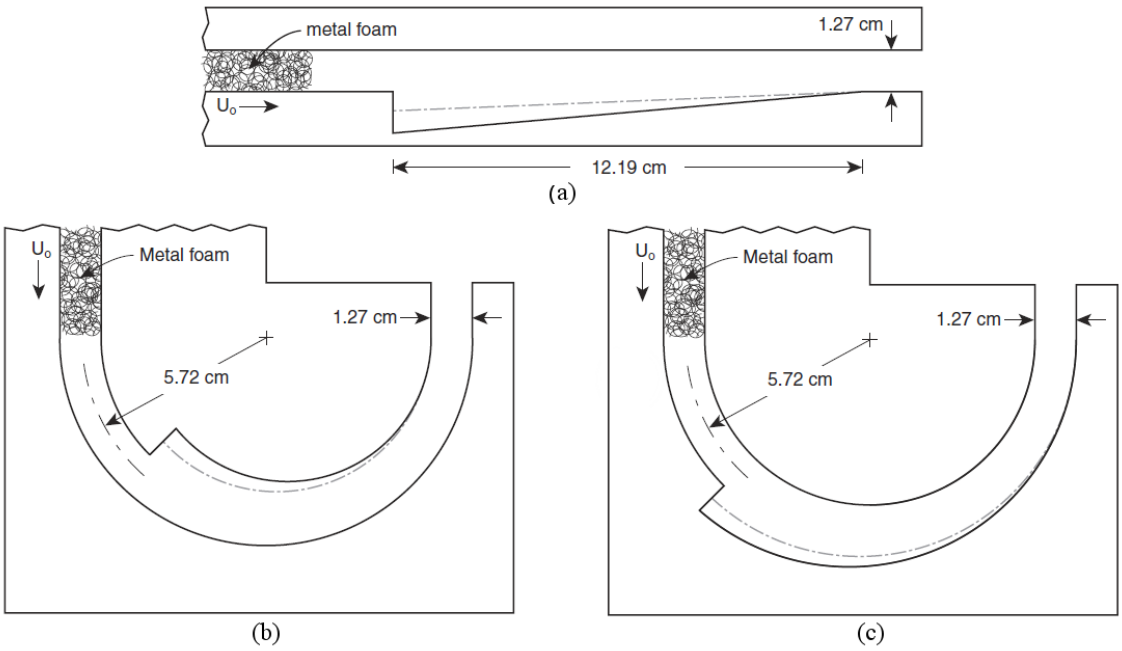

Figure 10. Channel Designs Tested by Lapsa and Dahm [13]

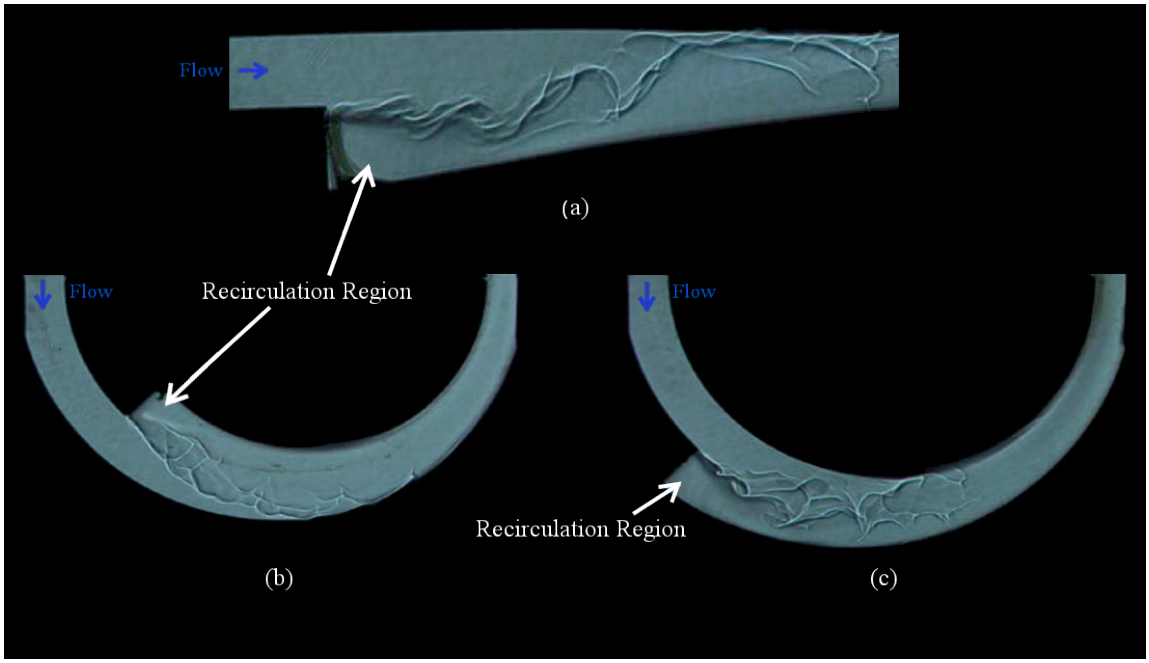

Figure 11. Backward Facing Step Shadographs (adapted from Lapsa and Dahm [13])

The geometry of Figure 10 (b) cannot be incorporated into the UCC as the inner diameter surface of the circumferential cavity is open so that the products can exit into the core flow. The mixing being dominated by small turbulence structures is also undesirable as combustion relies on mixing. Figure 10 (c) is not only desirable in that there is vigorous mixing but the geometry is also able to be easily incorporated into the UCC as the backward facing step sits on the outer diameter. More on the development and implementation of backward facing steps into the UCC will be discussed in Chapter IV, Section 4.1.

2.4 Film Cooling

In modern day turbine engines the hot gases leaving the combustor are commonly above the melting point of the materials making up the turbine blades. To keep the blades immediately following the combustor intact, film cooling is often used. Film cooling provides a thin film of cooler air to act as a barrier between the hot

exhaust gases, as shown in Figure 12. This cooling air is pulled from the compressor, bypassing the combustor, and injected through holes or slots on the airfoil surface. The cooling air traveling though the internal structure and film cooling holes of the airfoil act to cool the blade surface. Once ejected out of the film cooling holes, the cooling air creates a film over the airfoil surface that reduces the heat transfered to the blade surface from the exhaust gases.

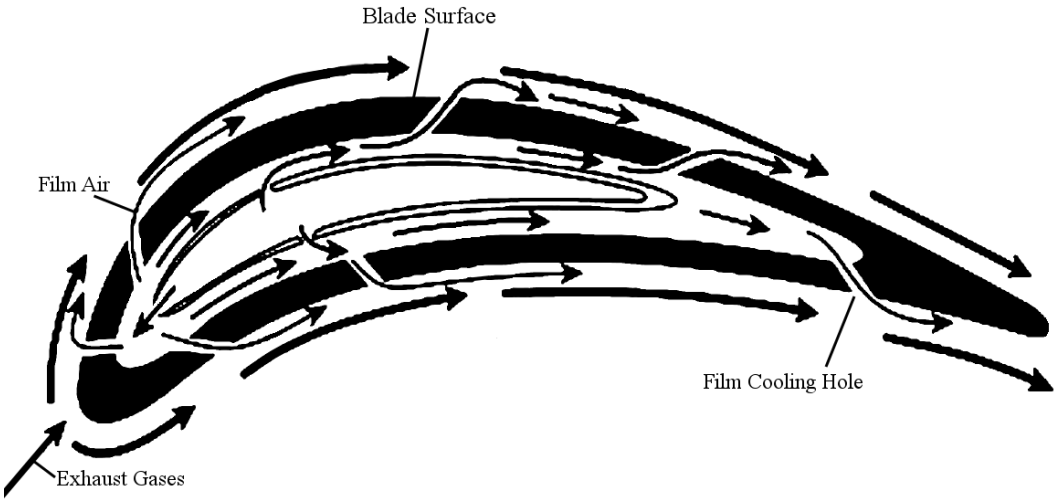

Figure 12. Film Cooling Schematic (adapted from Bogard and Thole [15])

There are many studies on differing film cooling hole schemes which vary the hole diameter, shape, angle, location, and number, such as the study by Dittmar et al. [16], which aim to develop the most efficient film cooling scheme. Many schemes are evaluated through its surface temperature profile and/or overall effectiveness. The surface temperature profile is determined using a measurement technique such as infrared thermography which will be discussed in Section 2.6. This provides the surface temperature, T_s, at many points along the evaluated surface. Combining this with the freestream exhaust temperature, T_∞, and the internal coolant temperature, T_{ci}, the overall effectiveness, ϕ_{eff}, profile for the film cooling scheme can be calculated using Equation 9.

$$\phi_{eff} = \frac{T_\infty - T_s}{T_\infty - T_{ci}} \tag{9}$$

The overall effectiveness is useful as it is a nondimensional parameter that takes into account the cooling done by the film externally, internally, and through the holes. The theoretical minimum value of overall effectiveness is zero and occurs when the airfoil surface temperature is equal to the freestream temperature. The theoretical maximum value is one and occurs when the coolant temperature and the airfoil surface temperatures are equal. According to Bogard [17], overall effectiveness for cooled airfoils is typically 0.6. The overall effectiveness can be calculated along the whole surface to evaluate the film cooling scheme for modification to reduce surface hot spots or for comparison to other film cooling schemes.

Film cooling problems involve both conduction and convection heat transfer. The effects of both mechanisms are quantified through their resistances. The conductive resistance, R_{cond}, is defined as:

$$R_{cond} = \frac{t}{k_{cond} A} \tag{10}$$

where t is the material thickness, k_{cond} is the thermal conductivity, and A is the surface area. The convective resistance, R_{conv}, is defined as:

$$R_{conv} = \frac{1}{h_{conv} A} \tag{11}$$

where h_{conv} is the convective heat transfer coefficient.

The importance between these two parameters is then quantified with the Biot number, Bi, which is a nondimensional parameter defined as:

$$Bi = \frac{R_{cond}}{R_{conv}} = \frac{h_{conv} t}{k_{cond}} \tag{12}$$

The Biot number is therefore a ratio between the conductive and convective resistances. Values less than 0.1 indicate negligible temperature gradients through the conducting surface. This allows an understanding of which mechanism is more impactful to the heat transfer problem.

2.5 Additive Manufacturing

Complex geometries, such as those used in film cooling, are difficult to manufacture. Technological advancements have increased the availability and usability of additive manufacturing to create complex designs with internal features. Additive manufacturing involves joining the build material layer by layer until a completed part is constructed [18]. A common method of this process is selective laser sintering, shown in Figure 13, which utilizes a bed of metal particles as the build material. A laser is then used to sinter the particles together to form a single layer, once complete a recoater blade places a new layer of particles over the built part, the process is then repeated until the part is completed. This method allows parts to be created with complex internal structures.

Additive manufacturing allows parts to be created with complex internal structures, however there are certain aspects of the process which must be taken into account when designing a part to be additively manufactured. First, the part cannot contain large overhangs or cantilevers as these structures can become deformed. A solution to this is to add support structures which are then machined off the printed part. This requires that traditional tooling can access those supports. The second consideration is the size of the build platform. The build platform has a specific width and depth, and can only move vertically within a certain range. This creates a maximum build volume which the designed part must remain within, as the part is build on the build platform. The final aspect to consider is the build resolution. Surface

features and holes must be sized within the resolution of the printer and particulate, or these feature may not be incorporated into the printed part. With these aspects considered, additive manufacturing can produce parts with complex features which are impossible using only traditional, subtractive manufacturing techniques.

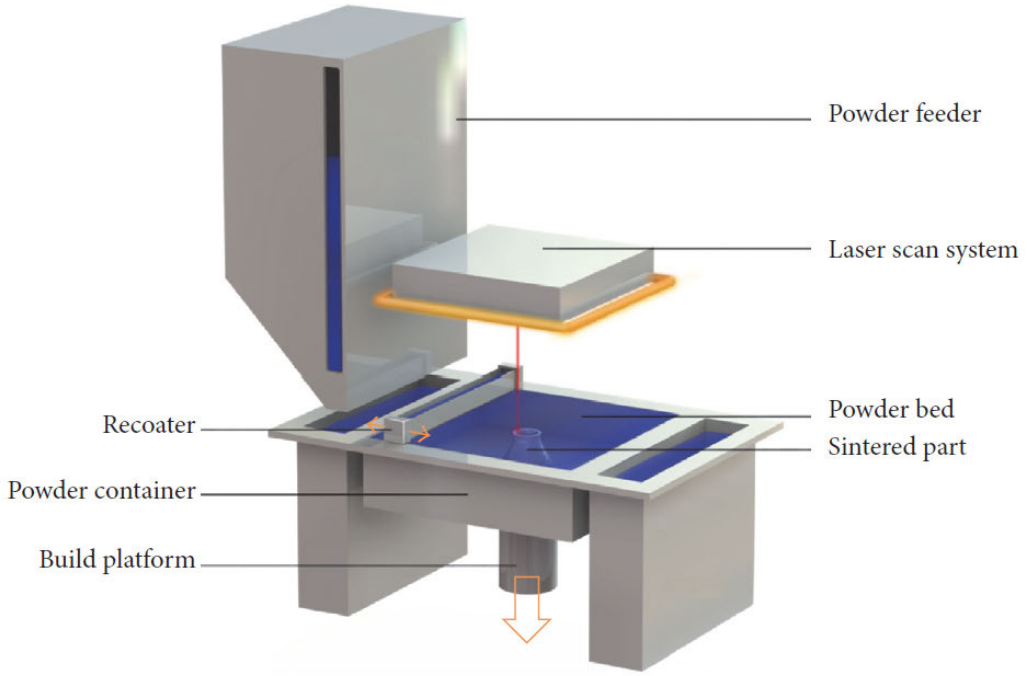

Figure 13. Selective Laser Sintering Technique (adapted from Hofland et al. [19])

2.6 Infrared Thermography

Infrared (IR) thermography is a widely accepted and commonly used technique for evaluating film cooling schemes. Accurate profiles of the surface temperature are captured with an IR imaging device, such as an IR camera. The camera captures the IR emission off the surface which is defined for a blackbody by Planck's Law:

$$E_{b\lambda} = \frac{2\pi h c_0^2}{\lambda^5 \left[exp\left(\frac{hc_0}{\lambda k T} \right) - 1 \right]} \tag{13}$$

where $E_{b\lambda}$ is the spectral blackbody emissive power, h is Planck's constant, c_0 is the speed of light in a vacuum, λ is the wavelength of emission, k is Boltzmann's constant, and T is the emitting surface's temperature. Most materials are not blackbodies and thus their emissivity, ϵ, is less than one and must be taken into account. Incorporating the surface's emissivity and simplifying Equation 13, Planck's Law becomes:

$$E_\lambda = \epsilon E_{b\lambda} = \frac{C_1}{\lambda^5 \left[exp\left(\frac{C_2}{\lambda T}\right) - 1 \right]} \tag{14}$$

with constants C_1 and C_2 defined as:

$$C_1 = 2\pi h c_0^2 = 3.742 \cdot 10^8 \qquad \mathrm{W}\cdot\mu\mathrm{m/m}^2 \tag{15}$$

$$C_2 = \frac{h c_0}{k} = 1.439 \cdot 10^4 \qquad \mu\cdot\mathrm{K} \tag{16}$$

When using IR thermography, the IR camera measures E_λ within the IR wavelength band and the surface temperature is the desired unknown. Therefore, Equation 14 can be rearranged to solve for T:

$$T = \frac{C_2}{\lambda ln\left(\frac{\epsilon C_1}{\lambda^5 E_\lambda} + 1\right)} \tag{17}$$

The difficulty with Equation 17 is that the surface emissivity is normally unknown and varies with respect to λ. Another problem is that the emission detected by the IR camera is not only the emission off the desired surface. The surrounding heated gases emit their own radiation which may or may not be reflecting off the test surface and adding to the emission recorded by the IR camera. Also, the camera is most likely viewing the test surface through a window, and thus the transmissivity of the window must also be incorporated.

Martiny et al. [20] discussed a calibration technique for IR thermography systems, called *in situ* calibration, to account for the additional environmental effects on the recorded emission profile. *In situ* calibration requires embedding one or more thermocouples on the test surface and measuring the surface temperature. The measured temperatures were then correlated to the recorded emission intensity at the location of the thermocouple. Doing this using either multiple thermocouples or varying the surface temperature resulted in a calibration curve between the recorded emission intensity and temperature which was used to convert the surface emission profile to a surface temperature profile. For *in situ* calibration the recorded surface temperatures must cover the entire range of interest. Schulz [21] noted that the accuracy of the thermocouple is based on its position on the test surface and its orientation with respect to surface and flow temperature gradients. An inaccurate thermocouple location will provide an incorrect calibration curve which may result in large temperature discrepancies. Therefore it is important to use multiple thermocouples for IR calibration to reduce the location uncertainty as well as allow for the removal of thermocouples located in high temperature gradients.

Another calibration technique was developed by Ochs et al. [22] called semi *in situ* calibration. Unlike *in situ* calibration, semi *in situ* calibration takes a pre-calibration of the test environment at ambient temperature. The test rig was setup with any objects that will be within the optical path of the IR camera's detector and a reference object in place of the test object. This reference object was painted with the same paint as the test object. This way the reference object's surface closely matches that of the test object. The reference object's temperature was measured by an embedded thermocouple and varied using a heater within the temperature range of interest. The readings from the IR camera were then calibrated with the measured thermocouple temperature. The reference object was then replaced with the desired

test object and the calibration from the reference object was used. The current design of the UCC makes incorporating a heater for a reference test object difficult, and thus *in situ* calibration was used and will be discussed more in Chapter III.

2.7 Particle Imaging Velocimetry

Particle Imaging Velocimetry (PIV) is a non-intrusive, optical flow visualization technique which uses lasers to obtain instantaneous velocity measurements. According to Adrian [23], the standard PIV setup consists of a double-pulsed Nd:Yag laser, optics, seed particles, and a CCD camera, as shown in Figure 14. The laser is directed through optics to create a laser sheet within the area of interest. This laser sheet is the plane which the velocity measurements are taken. Adding additional laser sheets can allow for 3D velocity measurements, however only 2D measurements were used in the UCC and are discussed here. Seed particles are released into the flow upstream of the laser sheet. The selection of seed particles is important as the particles must be sufficiently small to accurately track the flow field and represent the flow dynamics, while large enough to be imaged. This results in particles which are a few microns in diameter being used to seed the flow. The seed particles then travel through the flow and intersect the laser sheet where a CCD camera images the particles flowing through the laser sheet. The camera must be synchronized with the laser so the particles are illuminated when the image is taken. Two separate images are taken at the same time, however one has a longer exposure than the other.

The two recorded images are then sent through a post-processing procedure outlined in Figure 15. First, each image is divided into a grid, for increased resolution an overlapping grid can be used. Each grid cell is called an interrogation spot and the particle images in each spot of first image are compared with those in the second image. This allows particles to be traced and velocity vectors established. The veloc-

ity vectors of the particles in each interrogation spot are averaged and the resulting vectors are considered those of the flow field.

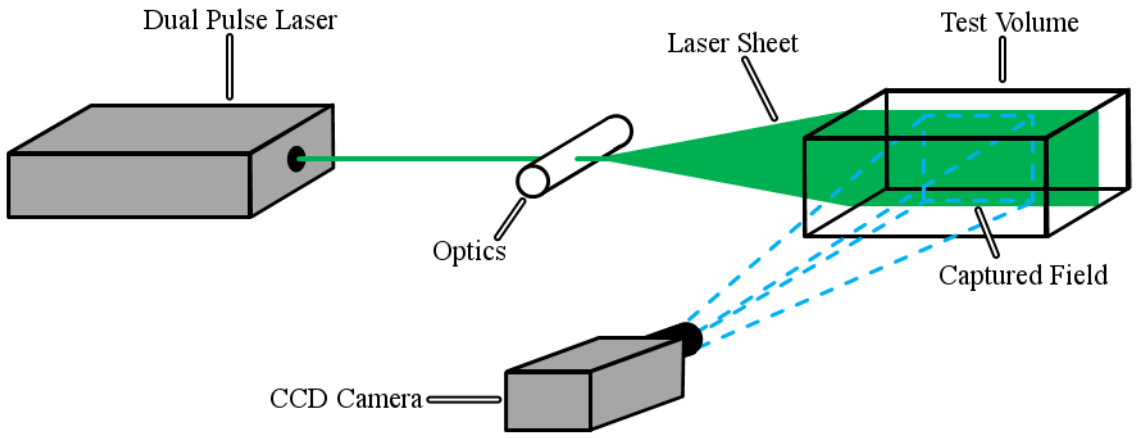

Figure 14. PIV Setup

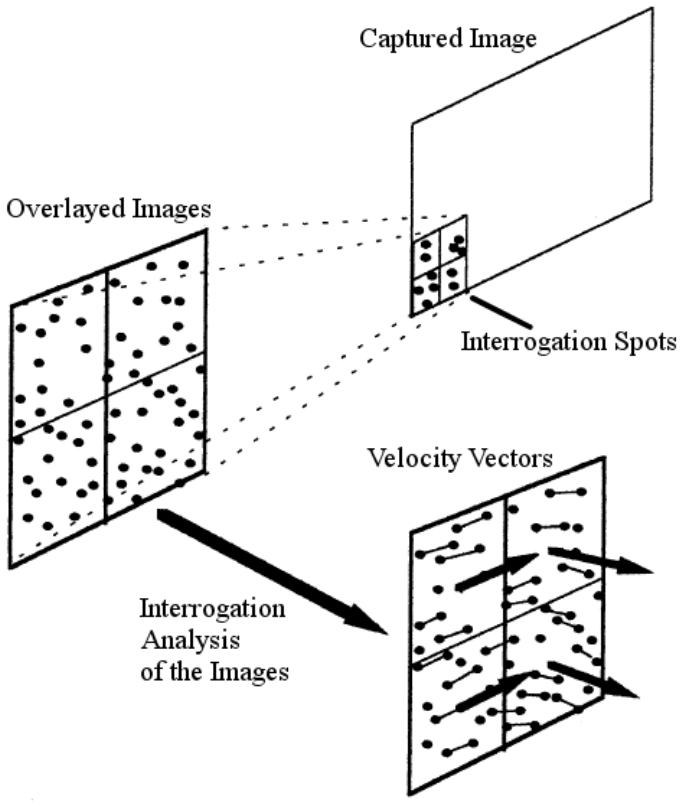

Figure 15. PIV Post-Processing (adapted from Adrian [23])

III. Baseline UCC Design

The Combustion Optimization and Analysis Laser (COAL) Laboratory at AFIT was set up by Parks [24] and Wilson [25] and houses both the UCC, shown in Figure 16, and the necessary equipment to support testing. This chapter covers the facilities, existing UCC as studied by Cottle [5], operation of the UCC, and repeatability in Sections 3.1, 3.2, 3.3, and 3.4, respectively. Section 3.5 then establishes a baseline set of results with Cottle's design for comparison with the component modifications that were developed to achieve the objectives of this research. These improvements will be discussed in Chapter IV.

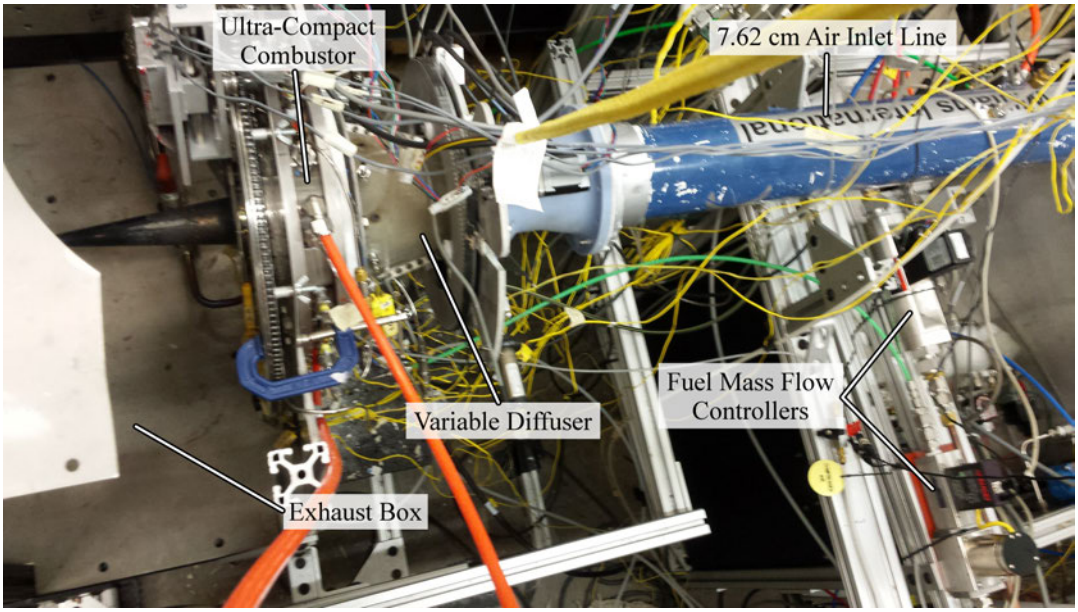

Figure 16. COAL Lab UCC

3.1 Facilities

The COAL lab had air flow supplied by two separate air feeds, COAL Lab air and shop air. COAL Lab air supplied by an Ingersol Rand H50A-SD 50 hp compressor and an air dryer, to remove any condensation, directly to the COAL Lab into a 7.62 cm line, the blue pipe in Figure 16. Shop air was supplied by two Ingersol Rand 50 hp

compressors to all AFIT labs. In the COAL Lab, this air was routed into a 3.81 cm line. Both air supplies were controlled by Flowserve MaxFlo 3 valves and monitored by FT2 Fox Thermal Instruments flow meters. The flow meters were calibrated by the manufacturer to $\pm 1\%$ and controlled through LabView.

The fuels used in the COAL lab were ethylene and propane, both of which were stored in an exterior fuel farm. The ethylene was stored in a gaseous state and was routed to an ethylene torch used to ignite the CC, with the flow controlled by an 8-channel, digital MKS type 647C controller. The igniter mixed 25.0 SLPM of air with 3.5 SLPM of ethylene, then initiated combustion of this mixture using an automotive spark plug. The flame traveled out the igniter where it ignited the propane and air mixture in the CC. Once combustion within the CC was initiated, the ethylene flow was closed off and combustion was maintained using propane. The propane was stored in four 150 gal tanks as a liquid. Once the tanks were opened, the propane flowed to two Zimmerman LPG electric heaters which vaporized the propane before being routed into the COAL lab with flow controlled by a four channel 0154 Brooks mass flow controller, shown in Figure 17. The propane was then directed to fuel plugs, which were bolts with a through hole in the center, and into the circumferential cavity. For the fuel flow split study, discussed in Section 4.2.3, and tests with the redesigned back plate, discussed in Section 4.3, an Alicat MCR-250SLPM-D-40X55 mass flow controller was added, and is shown in Figure 17. The Alicat mass flow controller was controlled through LabView and allowed for independent control over a second fuel flow into the cavity.

The exhaust of the UCC vented into the exhaust box shown in Figure 18. An exhaust duct was fed directly into the exhaust box. The duct was connected to two fans and then exited out the roof. The mass flow rate traveling through the duct was about 0.24 kg/s of air, which was over twice the amount through the UCC. This

caused a low pressure region in the exhaust box which pulled in surrounding air and UCC exhaust gases. This system kept emission gases out of the lab environment.

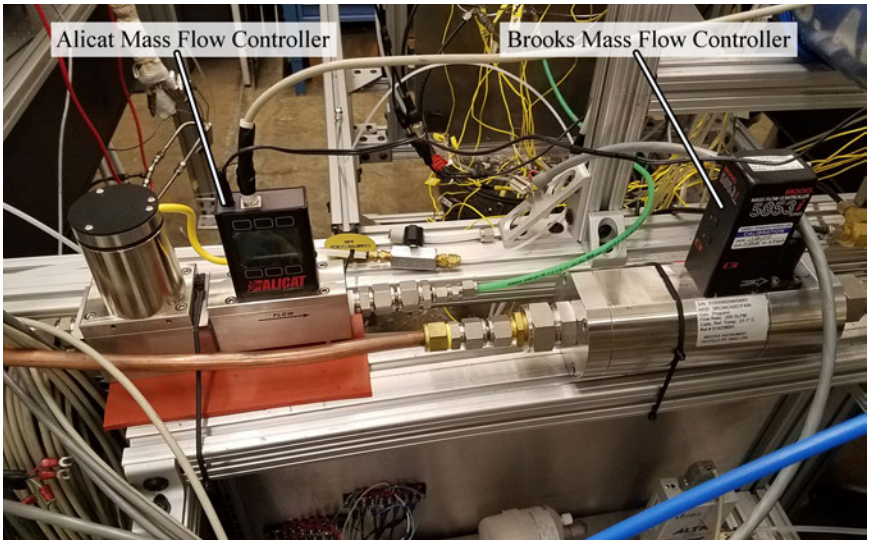

Figure 17. Fuel Flow Controllers

Figure 18. UCC Exhaust Box

3.2 Test Rig

The COAL Laboratory houses the UCC designed by Cottle [5], which is shown in Figure 19. Air flow, supplied by the 7.62 cm line, entered the rig on the left in Figure 19 and was split into either the CC or the core flow by a variable diffuser designed by Bohan et al. [26]. Air entering the CC entered through air injection holes on the front plate. Within the cavity gaseous propane was injected from the outer diameter.

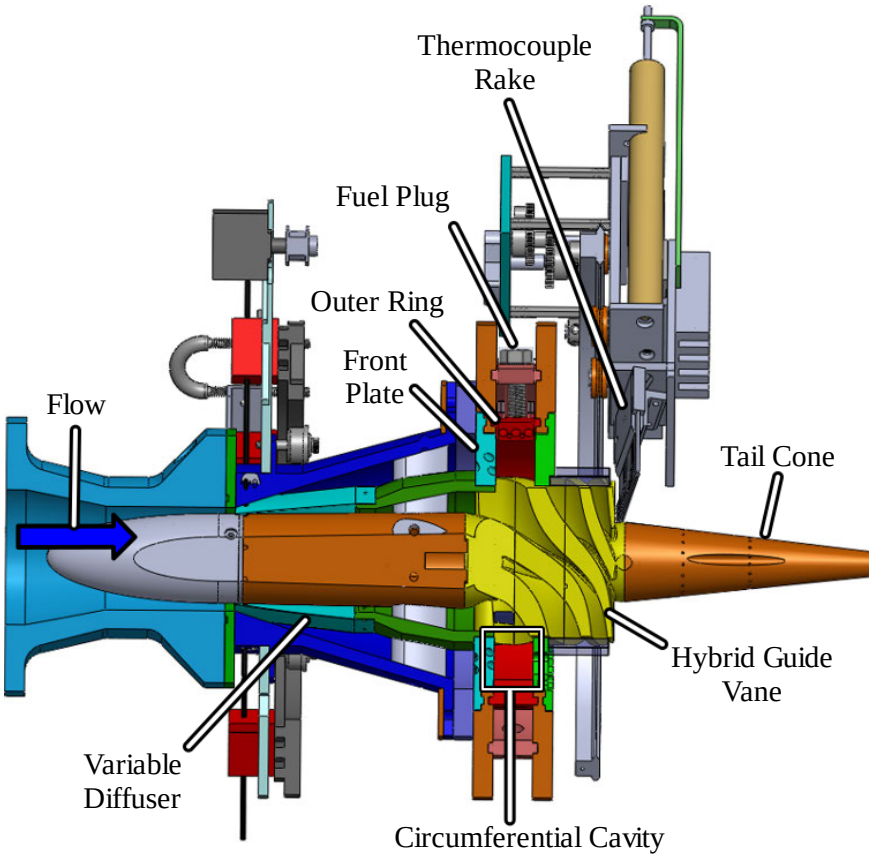

Figure 19. AFIT UCC Cross-section

The variable diffuser controlled the airflow into the CC and the core by regulating the inlet areas into each. The variable diffuser, shown in Figure 20, consisted of support vanes, feathers, push rods, an outer housing, and an actuation system. The feathers were eight stainless steel sheets 0.178 mm thick which overlapped and were

held in place by the support vanes. The upstream side of each feather was connected to three push rods which entered through the outer housing, which was sealed with an o-ring. The push rods were then connected to the actuation system and moved radially to bend the feathers, opening or closing the diffuser.

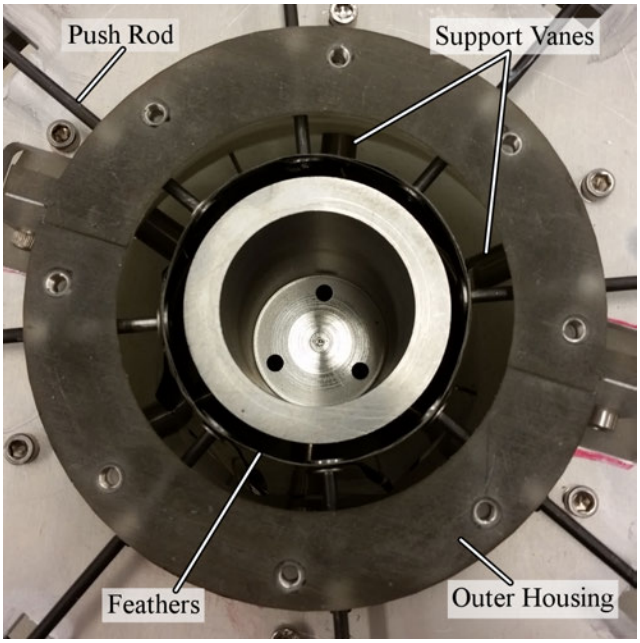

Figure 20. Variable Diffuser Design (adapted from Bohan et al. [26])

The diffuser actuation system, shown in Figure 21, included blocks, a scroll gear, and a stepper motor. While one end of the push rods were connected to the feathers, the other was connected to a block. The block then contacted a scroll gear which only allowed the block and push rod assembly to move radially. The scroll gear was connected to a stepper motor using a timing belt which allowed rotation of the gear. The stepper motor used pulses which moved the diffuser feathers radially in 0.01 mm increments. Movement was controlled by a Raspberry Pi Model 2 connected to an Arduino and a grblShield. The commanded position of the variable diffuser was input in "Universal G-Code Sender", which is an open-source Java program that sent a g-code command to an Arduino. The Arduino converted the command to

the grbl language and sent it to the grblShield which converted the command to pulses and moved the motor. A linear position sensor then completed the loop by giving feedback to the LabView data acquisition system confirming the position of the variable diffuser.

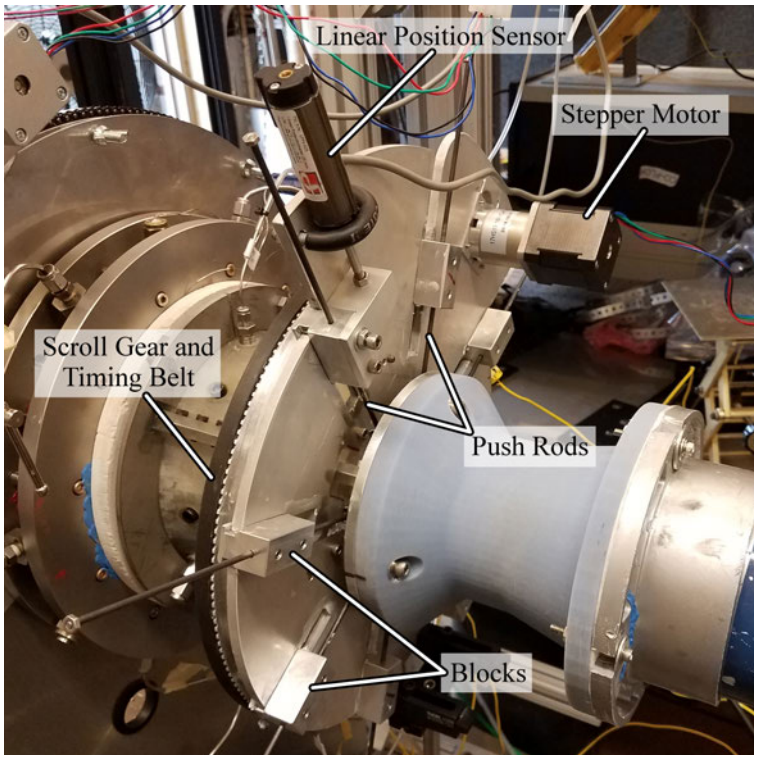

Figure 21. Variable Diffuser Actuation System

The required position of the variable diffuser to obtain a specific air mass flow rate through the core was determined by using the pressure differential between static and total pressure of the core flow within the diffuser. The desired core mass flow rate, $\dot{m}_{core}$, was first converted to an average core velocity, $\overline{U}_{core}$, by using the density of the flow, ρ, area of the core passage, A, and Equation 18.

$$\overline{U}_{core} = \frac{\dot{m}_{core}}{\rho A} \tag{18}$$

Then, using a fully developed turbulent profile assumption, the following equations were used to estimate the required velocity flow entering the pitot tube:

$$\frac{U - \overline{U}_{core}}{U_\tau} = \frac{1}{\kappa} \tag{19}$$

$$\frac{U}{\overline{U}_{core}} = \frac{1}{\kappa} ln\left(\frac{yU_\tau}{\nu}\right) + B \tag{20}$$

where U is the velocity of the flow entering the pitot tube, U_τ is the friction velocity, κ is the Von Kármán constant, y is the height of the pitot tube from the wall, ν, and B is a constant. Finally, the pressure differential, ΔP, which resulted in this velocity, and thus the desired airflow split, was then obtained using Bernoulli's equation:

$$\Delta P = \frac{U^2 \rho}{2} \tag{21}$$

This process was simplified by creating a MATLAB script which took the incoming air mass flow rate and calculated the necessary pressure differentials for a variety of airflow splits. The variable diffuser was then moved until the required pressure differential, and thus the desired airflow split, was obtained. Due to the variable diffuser operating on a pressure balance within the system, the range of obtainable pressure differentials, and thus airflow splits, varied depending on the total air mass flow and the combustion dynamics within the CC, which limited the airflow splits the diffuser could obtain during operation. This diffuser operating range with respect to total air mass flow is studied and discussed in Section 4.2.3.

When this research investigation initiated, the CC was in Cottle's orientation [5]. This baseline CC was contained axially upstream by the front air driver plate, radially outward by the outer ring, axially downstream by the back plate, and was open to the HGV radially inward. Cottle's cavity design supplied air to the CC only through the air injection holes on the front plate of the cavity, shown in Figure 22 (a), while fuel

was introduced from the outer ring of the cavity, shown in Figure 22 (b). The front plate had 48 air injection holes angled at 55° in order to promote the circumferential motion of the cavity flow. Fuel was injected radially from six equally spaced ports around the outer diameter of the CC. The injected fuel hit a baffle, shown in Figure 22 (c), and exited out of the holes shown in Figure 22 (d) which dispersed the fuel as it entered the cavity. The slow moving fuel was well dispersed, but due to the perpendicular injection it slowed the cavity flow, reducing the centrifugal loading. The results reported by Cottle et al. [9] also showed an inadequate amount of air along the outer diameter for combustion which caused a build up of fuel on the outer diameter, as shown in Figure 23.

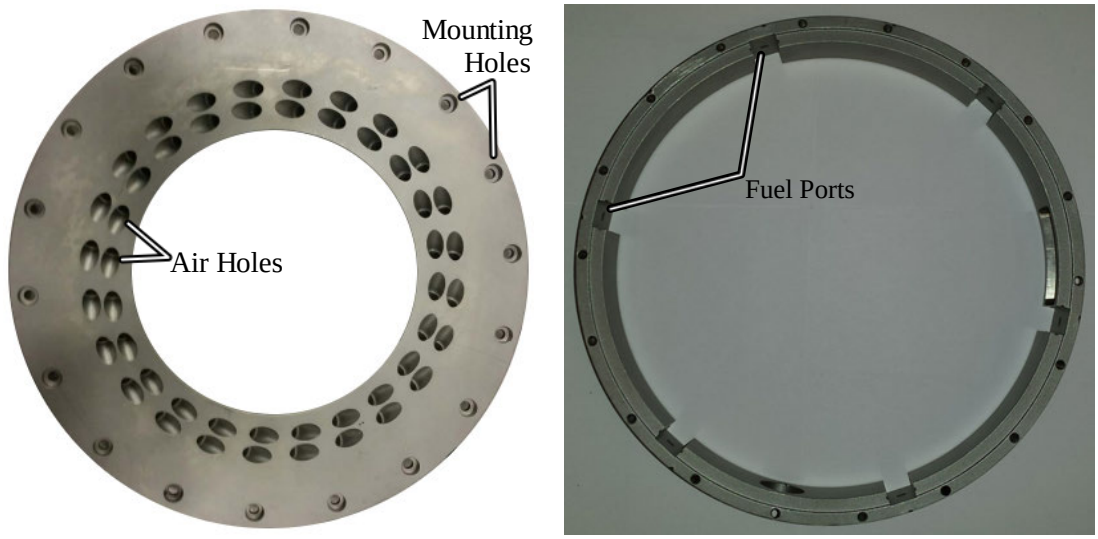

(a) Front Air Driver Plate

(b) Outer Ring

(c) Fuel Baffle

(d) Fuel Inlet Holes

Figure 22. Original UCC Cavity Injection Parts

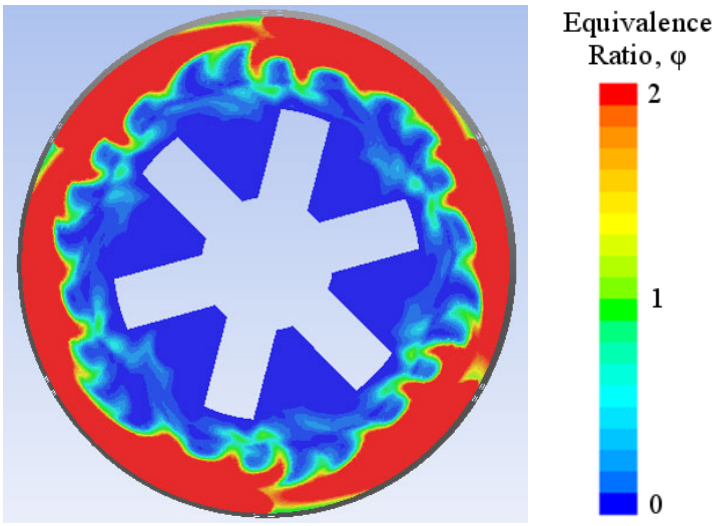

Figure 23. Fuel Buildup on CC Outer Diameter [9]

The back plate, shown in Figure 24, acted to contain combustion and prevent the cavity flow from traveling axially. The back plate also contained a 1.85 cm tall 80° cutout and pathways for instrumentation. The 80° cutout was designed to fit a quartz window for viewing combustion within the CC allowing flow diagnostic techniques such as those discussed in Section 2.7. The instrumentation pathways allowed thermocouples to be routed into the CC which measured combustion temperatures at the $\frac{1}{4}$, $\frac{1}{2}$, and $\frac{3}{4}$ cavity axial locations.

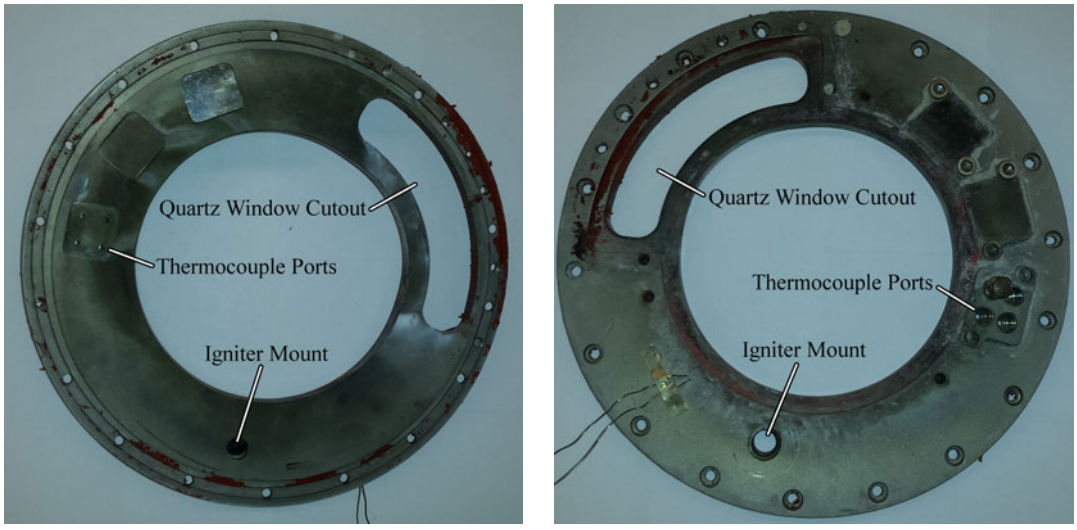

(a) Cavity Side (b) Exterior Side

Figure 24. Original UCC Back Plate

The core flow completely bypassed the CC, and directly entered the HGV shown in Figure 25. The HGV was first designed by Bohan [1] and built by Wilson et al. [27]. As shown in Figure 26, the outer radius of the HGV was exposed to the CC starting 1.22 cm axially from the HGV leading edge which allowed the combustion products to exit the CC and enter the HGV where they mixed with the core flow. The mixture of core and cavity flow then continued through the HGV until it exited the UCC test rig as exhaust. The HGV was 10.16 cm long, 10.80 cm in diameter, and consisted of six solid, stainless steel vanes. The vanes aimed to turn the combustion products to 70° off axial in preparation for a turbine stage. The HGV also acted as a secondary reaction zone where combustion was completed.

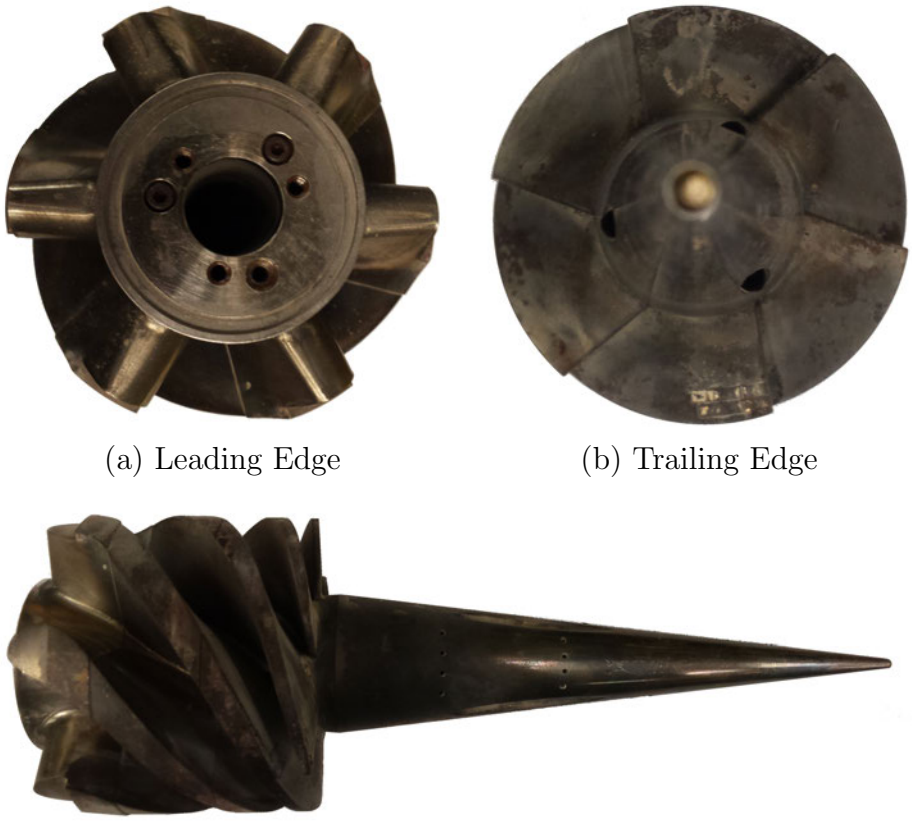

(a) Leading Edge

(b) Trailing Edge

(c) Side

Figure 25. Original UCC HGV With Tail Cone

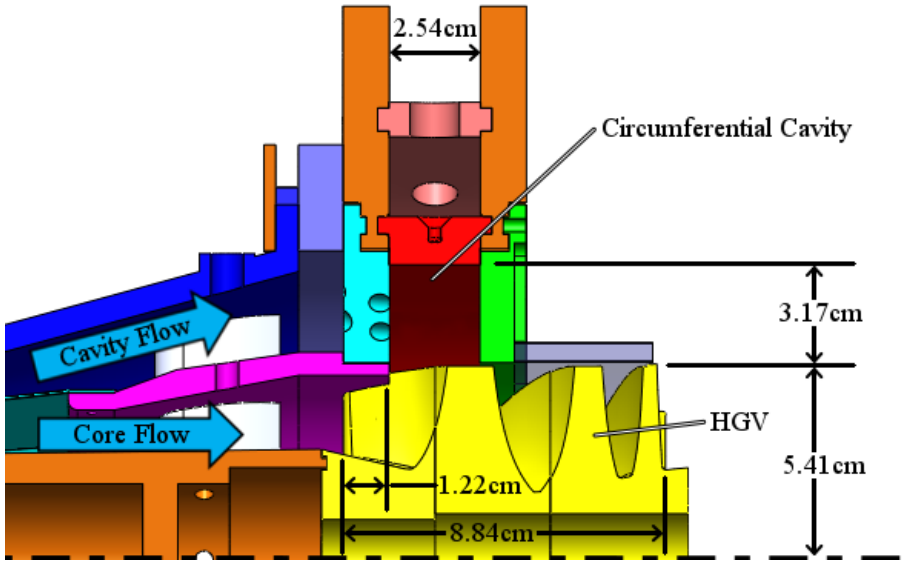

Figure 26. UCC HGV Position and Dimensions

Thermocouples were used within the cavity and at the exit plane for temperature measurements, shown in Figure 27. Within the cavity, six K-type thermocouples were used at three axial locations: one at $\frac{1}{4}$ cavity (front of the cavity), four at $\frac{1}{2}$ cavity (middle of the cavity), and one at $\frac{3}{4}$ cavity (back of the cavity). These thermocouples used the Omega K-type thermocouple factory calibration of $\pm 0.75\%$ or $\pm 2.2°C$, whichever was greater, and were recorded through LabView at 10Hz.

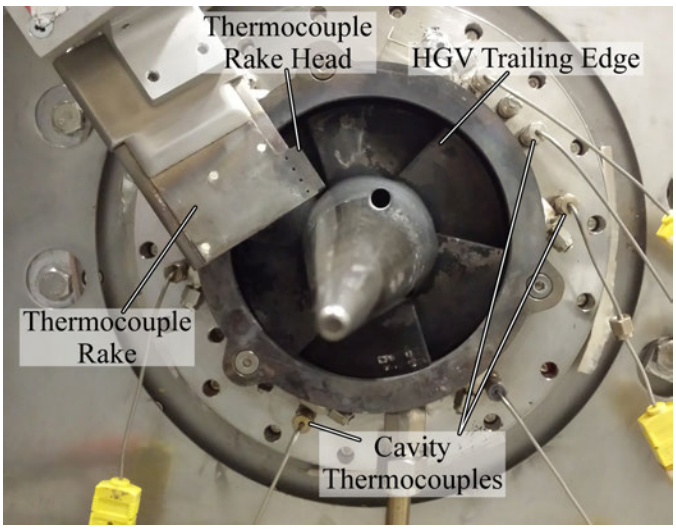

Figure 27. UCC Cavity and Exit Plane Thermocouples

At the exit plane of the UCC was a thermocouple rake, designed by Bohan and Schmiedel, which consisted of four B-type thermocouples aligned into the flow 6.5 mm axially downstream of the vane trailing edge which were moved both radially and circumferentially. Movement of the thermocouple rake head was controlled by a similar system as the variable diffuser, through a Raspberry Pi Model 2. For the rake a g-code file was used and uploaded to "Universal G-Code Sender", which is a program used to connect the Raspberry Pi to the thermocouple rake motors. The g-code would run through a script which moved the thermocouple rake radially and circumferentially. Radial measurements were taken in 4.8 mm increments, as shown in Figure 28, every 10° over an 80° circumferential arc. The thermocouples used the Omega B-type thermocouple factory calibration of ±0.5°C, and were monitored and recorded using LabView at a data rate of 10 Hz.

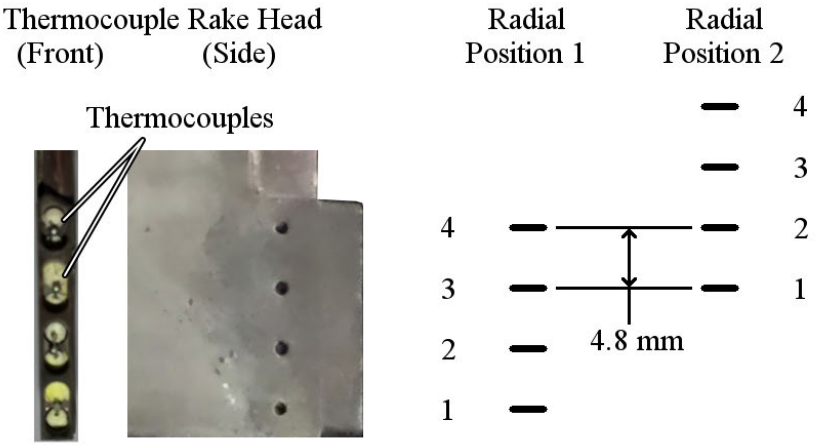

Figure 28. Thermocouple Rake Radial Positions

The recorded temperatures were post-processed using a MATLAB script which averaged the temperatures for each thermocouple at each position and then built a contour map of the exit plane temperature profile. This temperature profile showed what a turbine blade would experience if this combustor was used on an engine. The ideal profile for the cavity has the highest temperatures at mid cavity and away

from the walls which reduces the heat load to the walls and prevents them from melting [28, 29]. The code also calculated the pattern factor of the exit profile using Equation 22 where T_{max} is the peak temperature on the exit profile, T_{avg} is the average temperature of the exit profile, and T_{in} is the temperature of the inlet air before combustion.

$$PatternFactor = \frac{T_{Max} - T_{avg}}{T_{avg} - T_{in}} \tag{22}$$

3.3 Operation

Operation of the UCC was controlled from the work station shown in Figure 29. On the top left was the 8-Channel MKS which controlled the air and ethylene mass flow rate to the igniter through Channels 1 and 5, respectively. For ignition, the igniter air was set to 25.0 SLPM and the ethylene was set to 3.5 SLPM. The center left contained the Air flow readouts which showed the commanded flow rate, small numbers on the bottom, and the actual flow rate, large number, displayed as the percent of the maximum mass flow rate capable through the line. Each monitor corresponded to a different air feed line; the left screen displayed the 7.62 cm line, which was the main air flow, the center screen displayed the 3.81 cm line, which was the outer ring air flow and was used for the designs discussed in Chapter IV, and the right screen displayed the 1.90 cm line, which was not used by the UCC. The commanded percent can be converted to airflow by multiplying by 0.006 kg/s for the 7.62 cm line or 0.003 kg/s for the 3.81 cm line.

The bottom left monitor accessed the LabView program and data acquisitions system. The LabView program controlled the air and fuel solenoids, igniter spark, air mass flow rate through each air line, and fuel mass flow rate through the Alicat mass flow controller. The program user interface displayed the thermocouple mea-

surements, diffuser position in mm, thermocouple rake position in degrees and mm, and actual mass flow rates in kg/min. LabView was used to record the air mass flow rates, fuel mass flow rate, diffuser position, and thermocouple rake position at a rate of 1 Hz, while all temperature measurements were recorded at a rate of 10 Hz.

Figure 29. UCC Control Station

The top right of the workstation displayed camera views of the test rig for visual observation. On the center right was the Raspberry Pi system which allowed control of the variable diffuser and thermocouple rake through the Universal G-Code Sender program. The diffuser position was set by commands to the X position while the radial and circumferential positions of the thermocouples rake were controlled using the Y and Z positions, respectively. The bottom right housed the control module, which controlled the fuel mass flow rate through the Brooks mass flow controller using Channel 2. This fuel flow rate was input as SLPM in increments of 0.2.

Startup procedures involved turning on the two Zimmerman LPG electric heaters in the fuel farm to warm up for approximately 30 minutes to assure the liquid propane

fully vaporized. The COAL Lab compressor and air dryer were then turned on to fill the air supply tank. Once filled, the 7.92 cm, 3.81 cm, and auxiliary air line manual valves inside the COAL Lab were opened to allow the air flow rate to be controlled through LabView and the 8-Channel MKS. The propane and ethylene tanks were then opened and directed into the COAL Lab for control through the 8-Channel MKS, Brooks, or Alicat mass flow controllers.

The air flow for the 7.92 cm line was usually set to 10%, or 0.060 kg/s and the fuel flow through the Brooks mass flow controller was set to 24.4 SLPM as a start up condition. A flow of 25.0 SLPM and 3.5 SLPM of air and ethylene, respectively, though the 8-Channel MKS was initiated and the igniter sparked through LabView. Once the combustor was lit, the igniter spark was turned off and the flow through the 8-Channel MKS stopped. At this point the UCC was allowed to warm up and then the air and fuel was adjusted to the desired values for the test condition. The variable diffuser was moved to its appropriate position for the desired airflow split between the core and cavity by obtaining the desired pressure differential calculated before testing using the process outlined in Section 3.2.

The rig was then allowed to reach a steady state condition before data was recorded. If the thermocouple rake was not being used, data was recorded for 20 to 30 seconds, resulting in 200 to 300 cavity temperature points for each test condition. If the thermocouple rake was being used, data was recorded for 2 minutes to allow the rake to full traverse the exit plane, resulting in 1800 cavity temperature points, and 20 exit temperature points for each thermocouple position.

3.4 Repeatability

While the mass flow controllers were calibrated within 1%, fluctuations in the controller during testing occurred. The fluctuations in the 7.62 cm and 3.81 cm air

inlet lines while set to 0.052 kg/s and 0.004 kg/s can be seen in Figures 30 and 31, respectively. These measurements were taken during testing at a data rate of 1 Hz while the test condition was held for 98 seconds. The fluctuations for the 7.62 cm line were caused by compressor constantly filling up the air tank and the mass flow controllers trying to maintain the mass flow rate with the changing pressure. However even with these fluctuations, the average mass flow rate remained within 0.81% of the commanded value. The 3.81 cm line was ran at a low mass flow rate corresponding to 1.3% of the maximum flow rate through the line. At this flow rate, the controller began having trouble keeping the low flow rate and needed to constantly open and close maintain the commanded value. This resulted in a 8.57% variation in the resulting air mass flow rate over time.

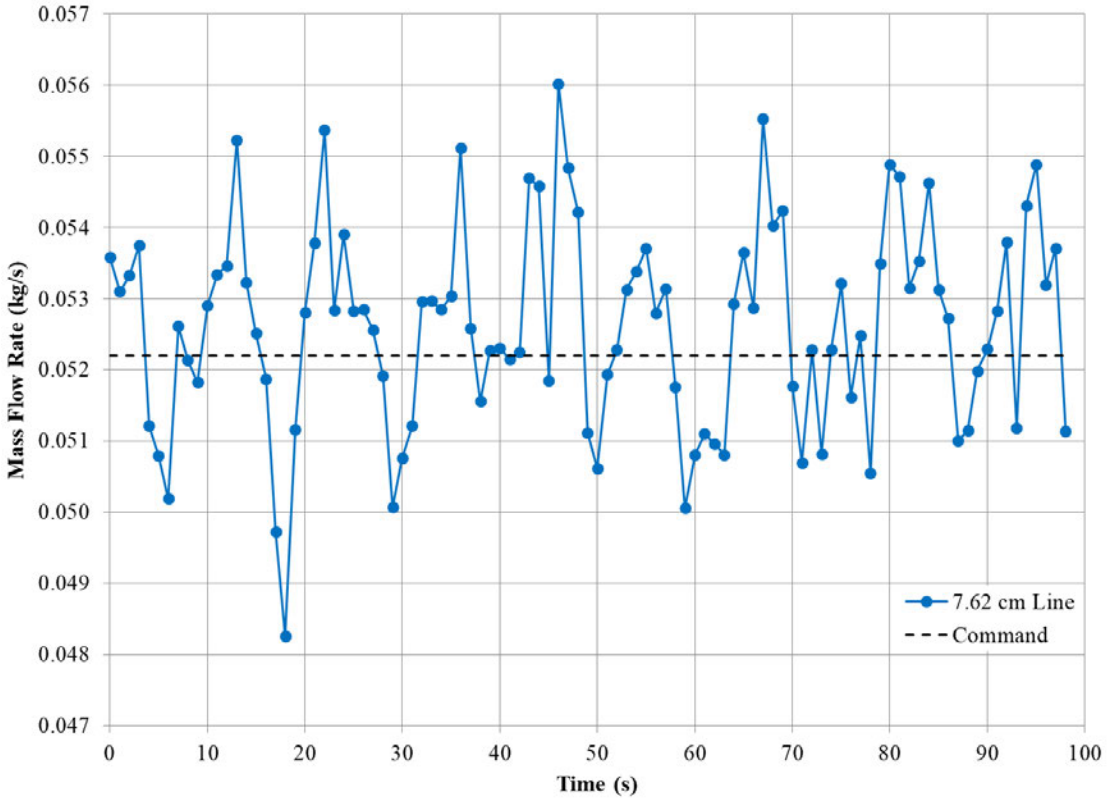

Figure 30. 7.62 cm Air Line Fluctuation

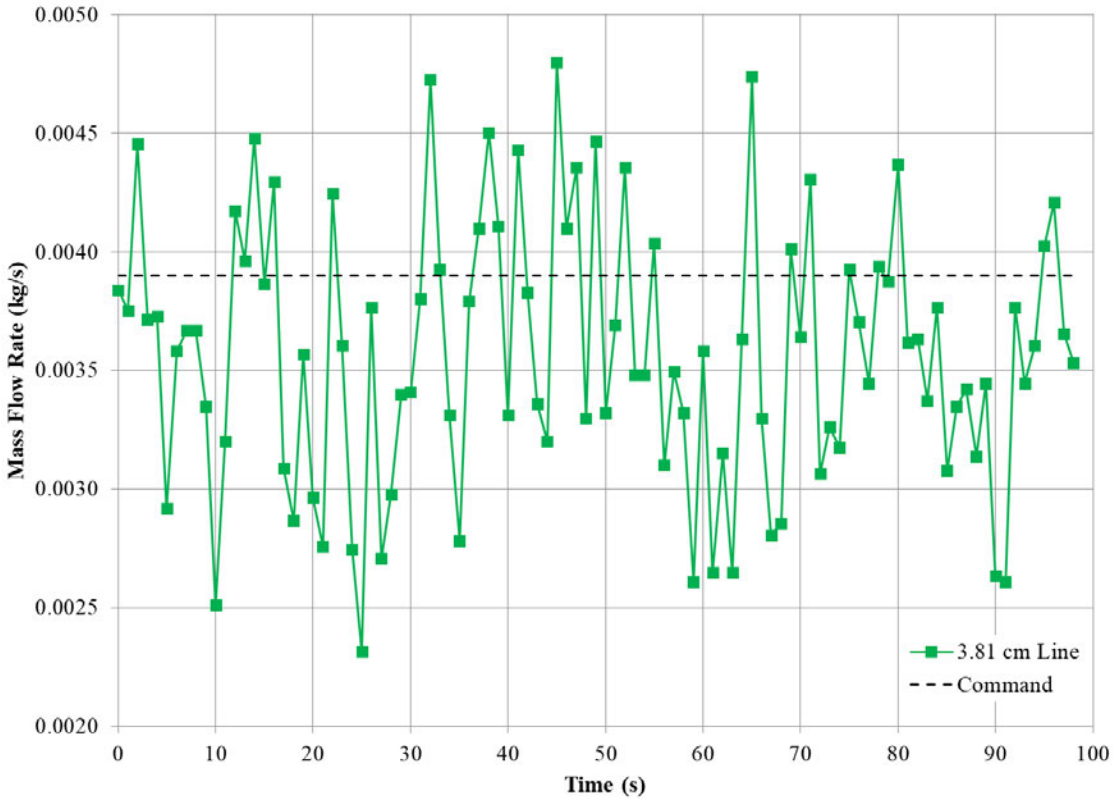

Figure 31. 3.81 cm Air Line Fluctuation

While the thermocouples were calibrated within 1%, the unsteady nature of the flow within the cavity can cause significant measurement fluctuations. To minimize the effects of the unsteadiness, the recorded data was time averaged, and in some instances spatially averaged. To quantify repeatability, the flow condition of 0.056 kg/s total air and 0.96 cavity equivalence ratio was ran six times on separate days and at different times during testing and the cavity temperatures recorded in Table 1. The $\frac{1}{4}$, $\frac{1}{2}$, and $\frac{3}{4}$ cavity temperature measurements had a 61 K, 62 K, and 64 K standard deviation, respectively, between the six cases. Spatially averaging these values produced the average cavity temperature which had a standard deviation of 31 K. These fluctuations were within reason when changes in inlet air temperature from day to day and mass flow rate were considered. The variation of average cavity

temperature, red, and the total air mass flow rate, purple, over a 40 second time period is shown in Figure 32. The fluctuations in total air mass flow rate corresponded inversely with the fluctuations in the average cavity temperature.

Table 1. Cavity Temperatures for Repeated Cases

Case	$\frac{1}{4}$ Cavity (K)	$\frac{1}{2}$ Cavity (K)	$\frac{3}{4}$ Cavity (K)	Average (K)
1	966	1109	664	913
2	883	1231	845	986
3	864	1182	691	912
4	819	1165	749	911
5	826	1276	775	959
6	797	1251	741	930
Deviation	61	62	64	31

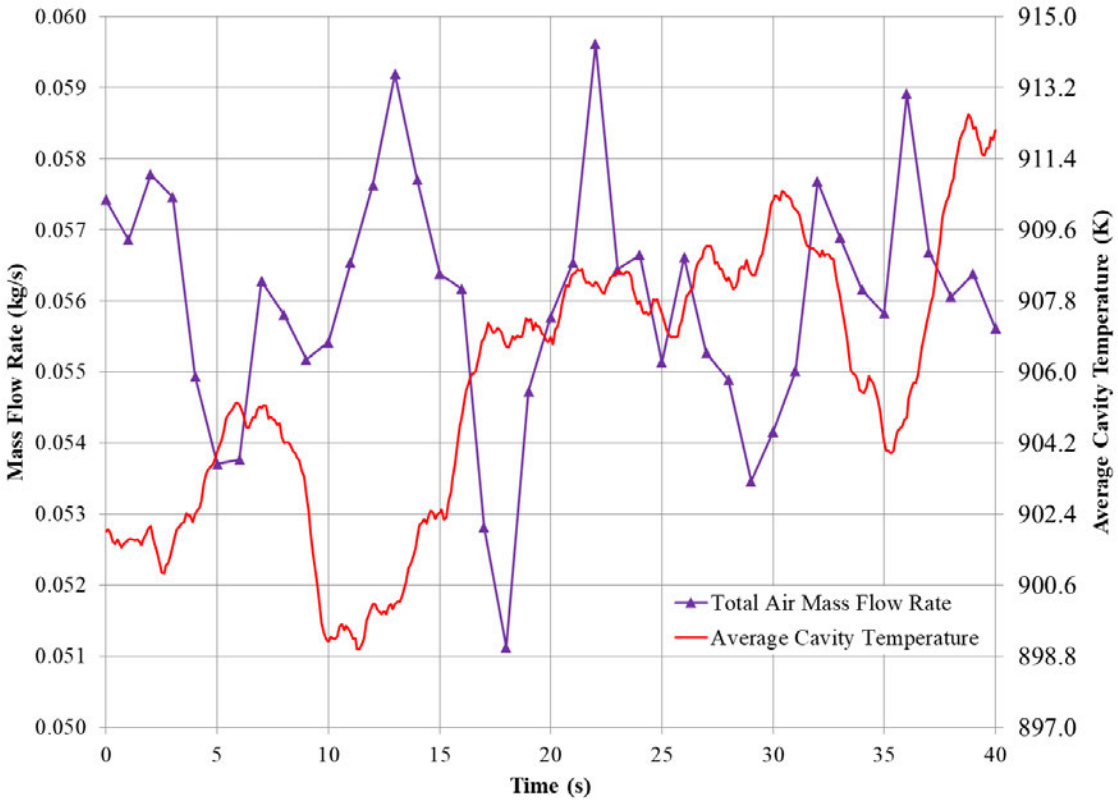

Figure 32. Total Air and Average Cavity Temperature Fluctuations

3.5 Baseline Results

Cottle's UCC design was tested at total air mass flow rates, $\dot{m}_{in}$, of 0.060, 0.090, 0.108, and 0.120 kg/s at cavity equivalence ratios, ϕ_{cav}, of 0.72 and 1.1 with an airflow split of 74% to the core and 26% to the CC. Tests were also conducted at a cavity equivalence ratio of 1.3 for a total mass flow rate of 0.108 kg/s. This equivalence ratio at other mass flow rates resulted in flameout. The test matrix is shown in Table 2 with the global equivalence ratio, ϕ_{Global}, core air mass flow rate, $\dot{m}_{core}$, cavity air mass flow rate, $\dot{m}_{cav}$, and fuel mass flow rate, $\dot{m}_f$, displayed.

Table 2. Baseline Test Cases

Case	ϕ_{Global}	ϕ_{Cav}	$\dot{m}_{in}$ (kg/s)	$\dot{m}_{core}$ (kg/s)	$\dot{m}_{cav}$ (kg/s)	$\dot{m}_f$ (kg/s)
1	0.19	0.72	0.060	0.044	0.016	0.0007
2	0.19	0.72	0.090	0.067	0.023	0.0011
3	0.19	0.72	0.108	0.080	0.028	0.0013
4	0.19	0.72	0.120	0.089	0.031	0.0014
5	0.29	1.10	0.060	0.044	0.016	0.0011
6	0.29	1.10	0.090	0.067	0.023	0.0016
7	0.29	1.10	0.108	0.080	0.028	0.0020
8	0.29	1.10	0.120	0.089	0.031	0.0022
9	0.34	1.30	0.108	0.080	0.028	0.0023

Case 3 was considered the cruise condition of the UCC and was evaluated computationally using FLUENT release16.2 with a Pointwise version 17.3 release 5 preprocessor. Heat transfer was modeled between the fluid and solid volumes by turning on the coupled fluid-solid energy equation. The flow within the CC and HGV passages were known to be turbulent and thus a a $k-\omega$ Shear Stress Transport (SST) model with viscous heating was used. This turbulence model was selected due to its performance in heat transfer problems and wall bounded flows [30]. The grid independence study for this geometry was conducted in a concurrent effort by Bohan et al. [31] at these same conditions, and confirmed that the unstructured grid used for evaluation

was well defined with a majority of the boundary layer resulting in a y^+ value of one or better.

Combustion was modeled using a Partially Premixed Model using the Flamelet Generated Manifold (FGM) with non-adiabatic, diffusion flamelets. The FGM model accurately models flame quenching due to wall contact or dilution air. To model combustion accurately the Gas Research Institute (GRI) 3.0 chemical equilibrium reaction mechanisms with a finite rate reaction progress variable were used. These mechanisms were used by FLUENT to generate mixture fractions of the combustion products at different flame temperatures, which was used to develop a probability distribution function (PDF) to define the species within the fluid volume of the computational model.

The computational results of Case 3 are shown in Figure 33. By averaging the tangential velocity along a constant radius iso-surface of 7.44 cm, corresponding to the radius of the middle of the quartz window, the average tangential velocity in the middle of the cavity axially was reported by Bohan et al. [32] to be 19.4 m/s for this case. Equation 23 was then used to calculate the centrifugal loading where r is the radius of interest, V_{tan} is the tangential velocity, and g is the gravitational acceleration. Using the radius of the middle of the quartz window, the centrifugal loading was calculated to be 516 g's. As discussed in Section 2.2.1, this centrifugal loading was on the low edge of the increased flame propagation range. To fully achieve the benefits of high-g combustion, increasing the tangential velocity and thus the centrifugal loading was imperative.

$$F_c = \frac{V_{tan}^2}{gr} \tag{23}$$

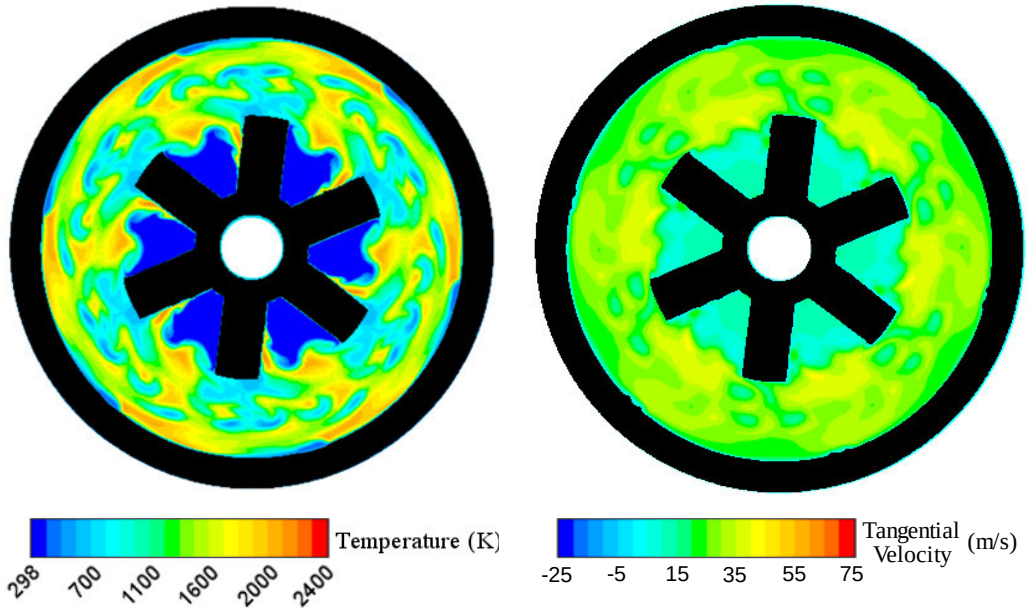

(a) Temperature (b) Tangential Velocity

Figure 33. Baseline $\frac{1}{2}$ Cavity CFD Generated Contours

The cavity temperature measurements for all cases can be seen in Table 3. For all cases except Case 9, the peak temperature was found at the $\frac{1}{2}$ cavity axial location with the highest variation being Case 3 with an increase of 196 K from the $\frac{1}{4}$ to $\frac{1}{2}$ cavity. Focusing on the effects of equivalence ratio, Figure 34 compares the experimental average cavity temperatures. The temperature for the 0.72 cavity equivalence ratio cases, blue, can be seen to increase to a peak temperature of 1346 K at a total air mass flow rate of 0.108 kg/s. After this point, the temperature began to drop slight. The cases at a 1.1 cavity equivalence ratio, red, are seen to have the peak temperature of 1285 K at the lowest flow rate, 0.060 kg/s. From this point, the average cavity temperature quickly dropped off to 1021 K at a 0.120 kg/s total air mass flow rate.

The trends seen in Figure 34 were most likely related to the fuel build up displayed in Figure 23 as the increased fuel flow rate allowed a thicker layer of fuel to build up along the outer diameter. The other aspect was the increased air flow through the front plate which moved the primary combustion region toward the rear of the cavity

Table 3. Baseline Cavity Temperatures

Case	$\frac{1}{4}$ Cavity (K)	$\frac{1}{2}$ Cavity (K)	$\frac{3}{4}$ Cavity (K)	Average (K)
1	1287	1353	1182	1274
2	1261	1406	1327	1331
3	1229	1425	1384	1346
4	1238	1413	1379	1343
5	1280	1358	1218	1285
6	1184	1337	1238	1253
7	1110	1232	1163	1168
8	939	1079	1047	1022
9	679	836	854	790

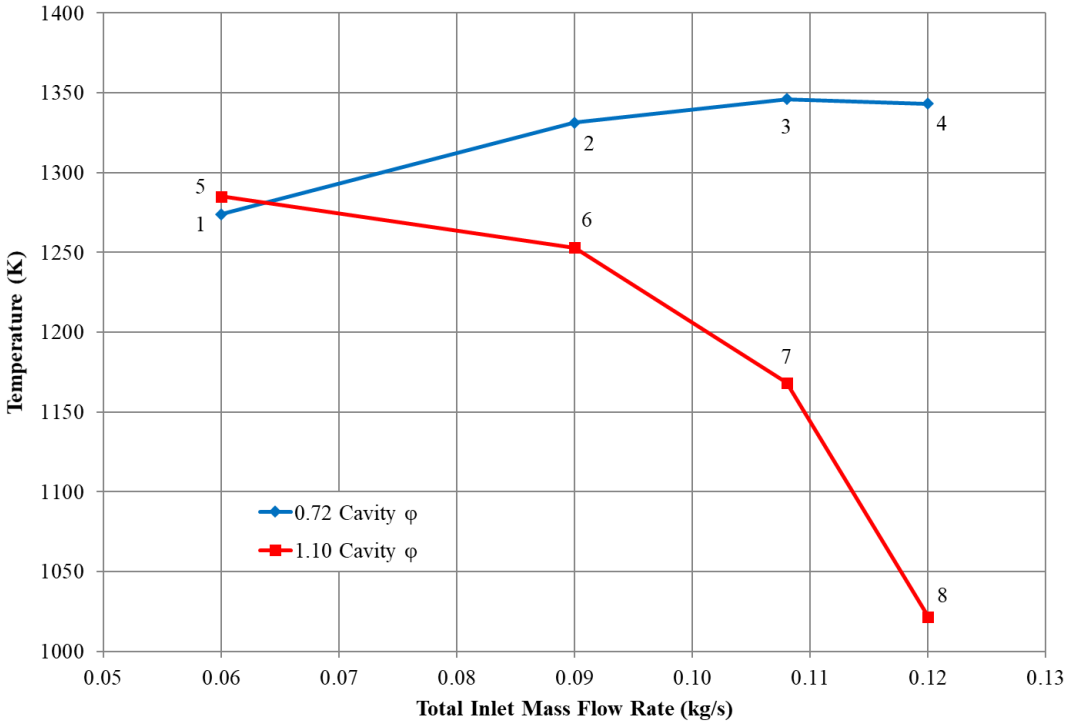

Figure 34. Baseline Average Cavity Temperature vs. Total Air Mass Flow

and eventually into the vane passage. This was confirmed by reviewing Table 3 where the $\frac{3}{4}$ cavity temperature increased from Case 5 to 6, and then decreased from Case 6 to 7 and to its minimum at Case 8.

The exit temperatures of the baseline cases were evaluated using the thermocouples rake and post-processed using MATLAB. The maximum exit temperature, T_{max}, average exit temperature, T_{avg}, and pattern factor for each case is shown in Table 4. For the 0.72 cavity equivalence ratio cases the average exit temperature varied very little, where the largest difference was 23 K between Cases 1 and 2. This trend was not present in the 1.1 cavity equivalence ratio cases. For these cases, both the maximum and average exit temperatures decreased from 1035 K to 932 K and 745 K to 658 K with increasing total air mass flow rate, respectively. The desirable range for a pattern factor was reported by Mattingly et al. [33] to be between 0.25 and 0.43. All the pattern factors calculated from the baseline cases are above this, with a range between 0.65 and 0.86, and need to be reduced before the UCC can be incorporated into a gas turbine engine.

Table 4. Baseline Exit Properties

Case	T_{max} (K)	T_{avg} (K)	Pattern Factor
1	822	613	0.67
2	911	636	0.82
3	894	631	0.79
4	892	618	0.86
5	1035	745	0.65
6	1076	731	0.80
7	949	663	0.79
8	932	658	0.76
9	792	598	0.64

Contour maps of the exit temperature for all nine experimental cases can be found in Figure 35. The exit temperature profiles showed a temperature gradient where low temperatures existed radially inward along the vane hub and higher temperatures existed radially outward along the vane tip. This indicates that the combustion products are not radially penetrating deep into the core flow. As discussed in Section 3.2, the existence of this temperature gradient is non-ideal as there would be an

increased heat load on the tip of a turbine blade, which could melt or deform the blade resulting in striking the engine casing or catastrophic failure of the turbine. At a cavity equivalence ratio of 0.72, or a global equivalence ratio of 0.19, the exit profiles exhibited the same characteristic where there was a thick low temperature region of 300 K to 600 K extending radially up to 50% of the contour, as shown in Figures 35 (a), (b), (c), and (d). This layer was thinned in Cases 5 and 6 where the low temperature region only extended radially up to 25% of the contour, however these contours displayed a high temperature pocket around 1000 K 75% radially and between -20° and 0° circumferentially, as shown in Figures 35 (e) and (f). Increasing the total air mass flow rate to 0.108 kg/s or 0.120 kg/s resulted in the Case 7 and 8 contours, shown in Figures 35 (g) and (h), respectively. These contours showed the hot spot found in Cases 5 and 6 was dramatically reduced to be a small region below 950 K. These profiles also showed an increased thickness of the low temperature region to about 40% of the contours radial height. At the highest equivalence ratio of 0.34 globally and 1.3 in the cavity, Case 9, the exit temperature drastically dropped off to temperatures below the lowest equivalence ratio cases, as shown in Figure 35 (i). The low temperature region extended to about 60% radially between -30° and 10° circumferentially and almost the full radial height between 10° and 30° circumferentially.

The results of this chapter established a baseline of the UCC performance to be used as comparison points. From these results, the CC was redesigned, as discussed in Chapter IV. Using computational methods and the experimental capability of the AFIT COAL Lab, discussed in Sections 3.1 and 3.2, cavity velocities, cavity temperatures, and exit temperatures of the redesigned CC were evaluated and compared with the baseline results, establishing the effects of the new components.

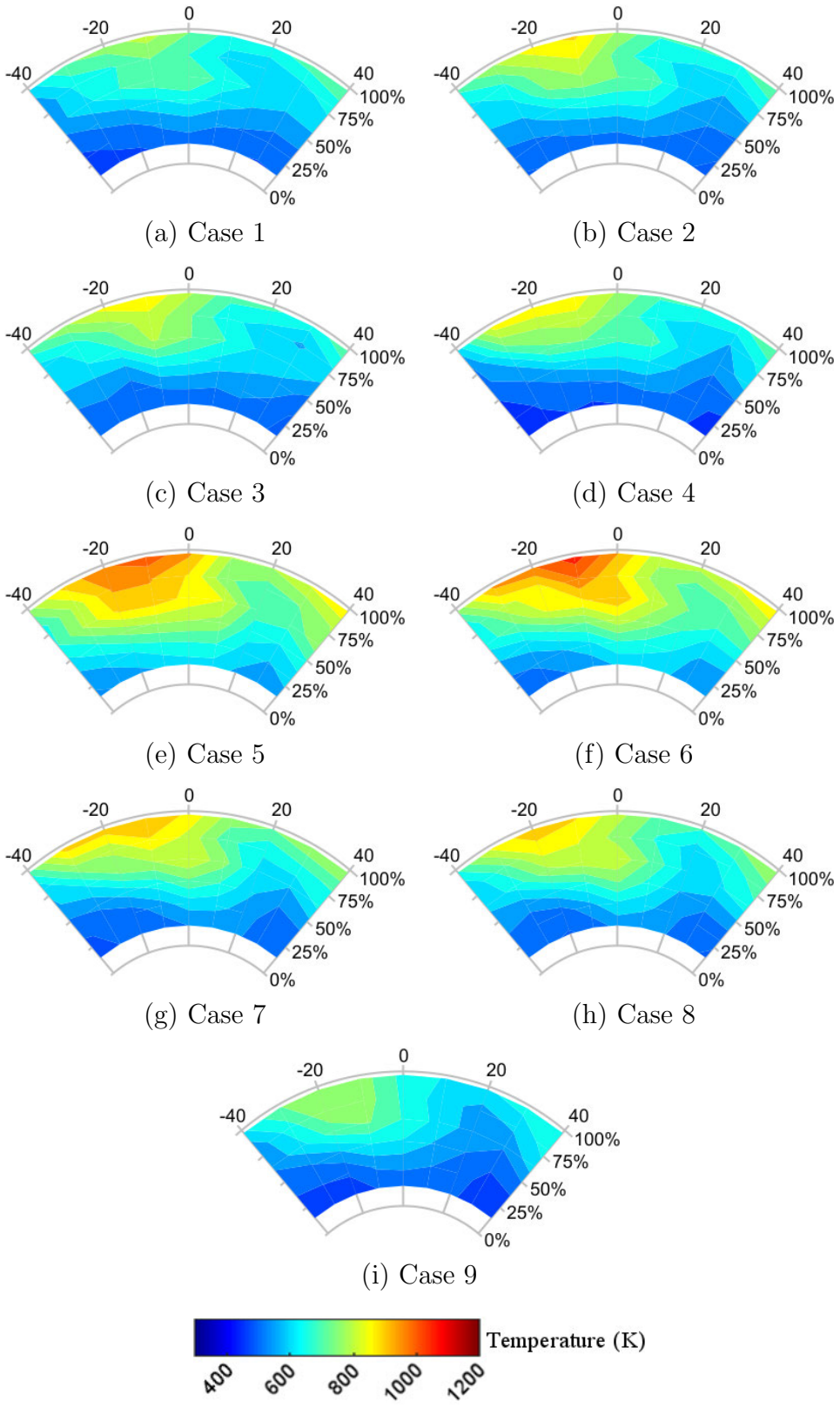

(a) Case 1 (b) Case 2

(c) Case 3 (d) Case 4

(e) Case 5 (f) Case 6

(g) Case 7 (h) Case 8

(i) Case 9

Figure 35. Baseline Experimental Exit Temperature Profiles

IV. Circumferential Cavity Redesign

Cottle's cavity design was successful in generating a centrifugal loading and burning within the CC. Unfortunately, the radial injection scheme did two things: first, the lack of air along the outer diameter resulted in a high local equivalence ratio, which was too high for combustion to occur. Second, the perpendicular injection slowed the bulk circumferential swirl within the cavity, reducing the centrifugal loading of the CC [9]. Therefore, changes in the UCC fuel and air injection into the CC were accomplished to allow control over the amount and location of air and fuel injection into the cavity and change the flow dynamics for better flame stabilization. With these changes, the local equivalence ratio along the outer diameter was decreased while the operating range and centrifugal loading was increased. The literature discussed in Chapter II was used to guide the design of this next iteration of improvements to the UCC. Changes were conducted by redesigning the outer ring and front air driver plate to incorporate improved control of the air introduction to the CC, discussed in Sections 4.1 and 4.2. The modification to the outer ring also enabled improved control of fuel introduction. This was further enhanced with the redesign of the back plate as discussed in Section 4.3.

4.1 6-Step Ring

A new outer ring injection scheme, referred to as the 6-Step Ring, aimed to increase the centrifugal loading in the cavity while improving air and fuel mixing by injecting the fuel and air tangentially to the bulk cavity flow out of six backward facing steps along the outer diameter of the CC, as shown in Figure 36 (a). The directionality of the injection served to increase tangential velocity and by bringing air into the outer portion, decrease the local equivalence ratio in the outer portion of the cavity.

Each of the six steps were 6.35 mm tall and equally spaced 60° around the outer ring. Each step contained five holes, as shown in Figure 36 (b); three 5 mm diameter ellipses, which were air inlets and two 2.5 mm diameter circular holes, which were fuel inlets. These holes were sized to introduce a nominal flow rate of $7.78{\cdot}10^{-4}$ kg/s of air, representing about half the total cavity air flow at a 74% to 26% core to cavity airflow split, at 34 m/s and $1.08{\cdot}10^{-4}$ kg/s of fuel at 11 m/s per hole. With the 6-Step Ring, air was also injected through the inner holes of Cottle's front plate while the other holes were taped over, as shown in Figure 36 (c). Reducing the front wall inlets was a result of redirecting half of the cavity air through the steps of the 6-Step Ring.

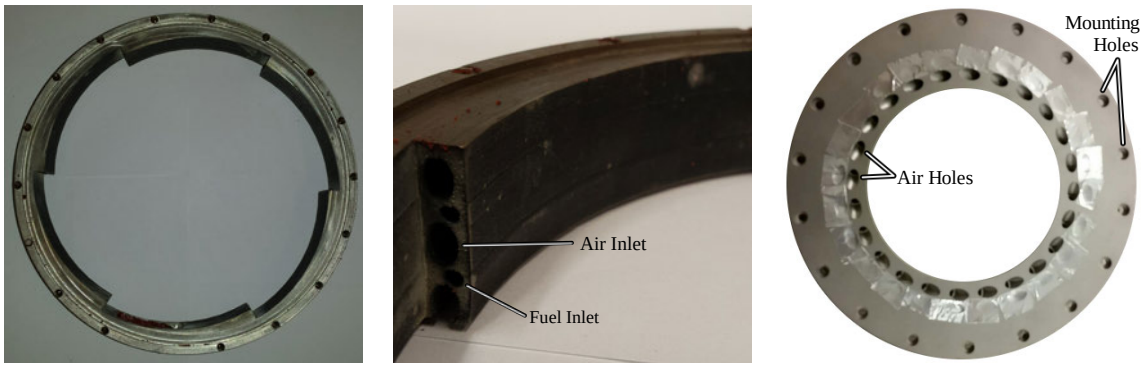

(a) 6-Step Ring (b) Step Face (c) Front Air Driver Plate

Figure 36. 6-Step UCC Cavity Outer Ring

The internal ducts of the 6-Step Ring, shown in Figure 37, meant the ring had to be additively manufactured. The 6-Step Ring was made out of Inconel on a Concept Laser M2 cusing 3D printer and was the first part printed by the AniMaL Lab at AFIT. The 6-Step Ring was printed on an aluminum build plate. However due to the build plate and the 6-Step Ring being a dissimilar metals, the part lifted off the build plate during printing which caused the ring to become warped and some air inlets to break through the sidewall, as shown in Figure 38. Although this was a print error, when installed in the UCC, the front and back plate contained the airflow, forcing

it out the designed path. The part was then brought to the AFIT Model Shop for post-processing which included drilling and taping the screw holes, beveling the fuel ports, and machining off excess material.

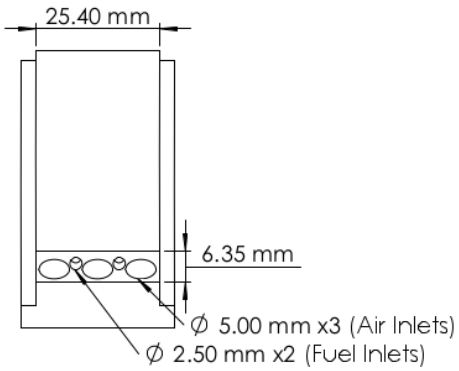

(a) Step Face

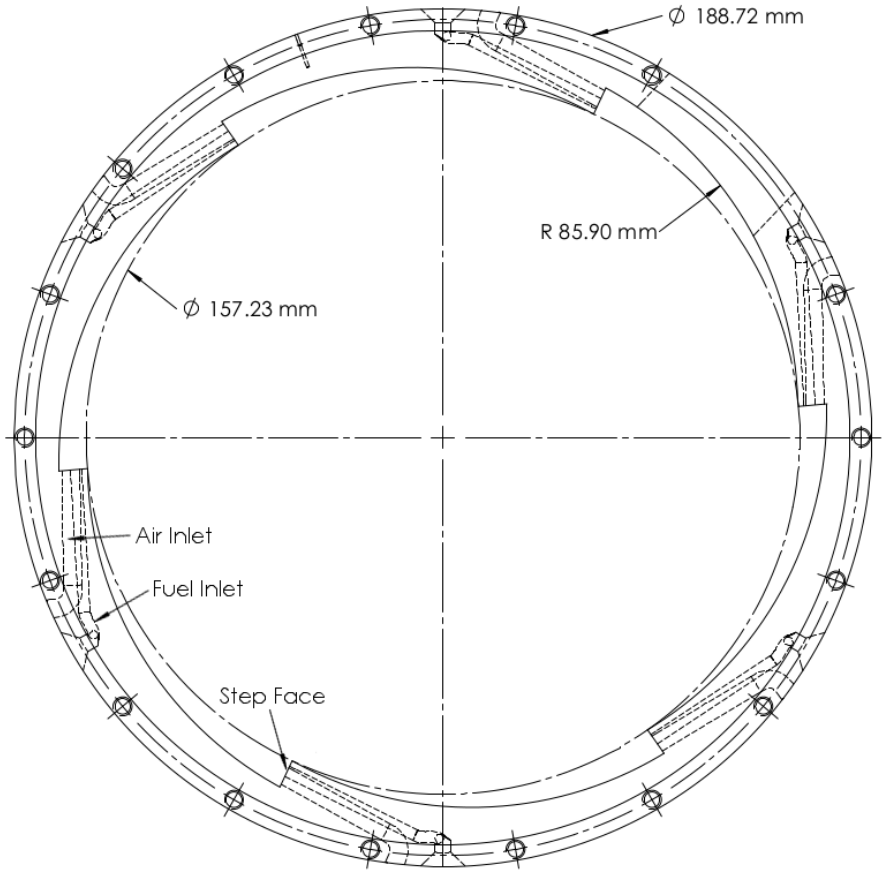

(b) Side View Showing Internal Ducts

Figure 37. 6-Step Ring Dimensions

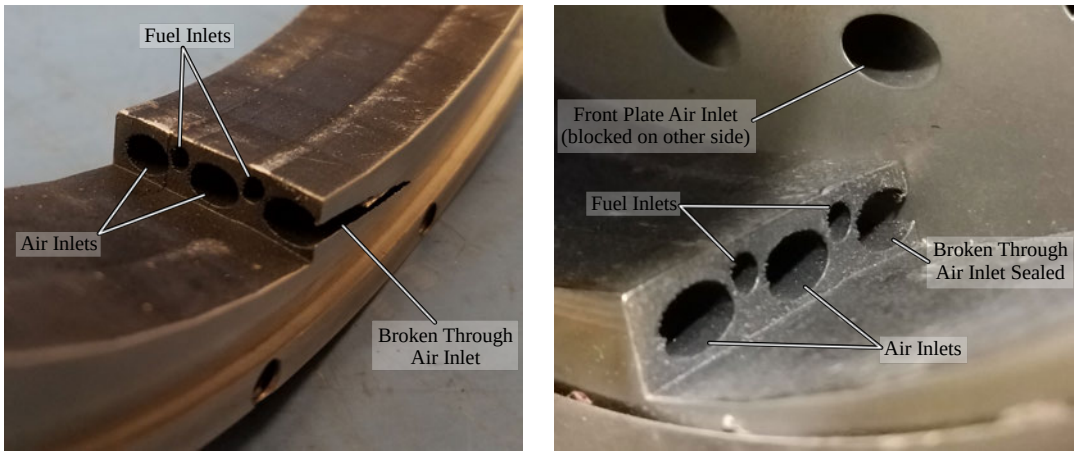

(a) Air Inlet Broken Through (b) Ring Installed

Figure 38. 6-Step Ring Print Error

4.1.1 CFD Evaluation.

The 6-Step design was computationally evaluated using FLUENT R16.2 with a Pointwise V17.3 R5 preprocessor and the settings outlined in Section 3.5. The flow condition was the same as that computationally tested on the baseline design, a 0.72 cavity equivalence ratio, 0.108 kg/s total inlet mass flow rate, and an air flow split of 74% to the core and 26% to the cavity. For the 6-Step design, 50% of the cavity air was directed through the outer ring, while the remaining 50% was directed through the front plate. This equated to an air mass flow rate of 0.014 kg/s through both the outer ring and front plate. The remaining 0.080 kg/s of air was directed through the core.

The resulting tangential velocity contours for the baseline and 6-Step Ring designs are shown in Figure 39 (a) and (b), respectively. An average tangential velocity for both designs was calculated by averaging the tangential velocity values along a constant radius iso-surface corresponding to the radius of the middle of the quartz window, which was 7.44 cm. While the average tangential velocity in the middle of the cavity axially was 19.4 m/s for the baseline configuration, for the same flow condition the average tangential velocity for the 6-Step Ring was predicted to be 28.5

m/s. Using Equation 23, the centrifugal loading along this radius was calculated for the baseline design to be 516 g's. The 6-Step design increased this loading to 1113 g's, equating to a 116% increase. This increase was the first objective of this research as it corresponds to an improvement in flame propagation benefits in a HGC [4]. From this analysis, the 6-Step design succeeded in improving the tangential velocity and centrifugal loading within the CC.

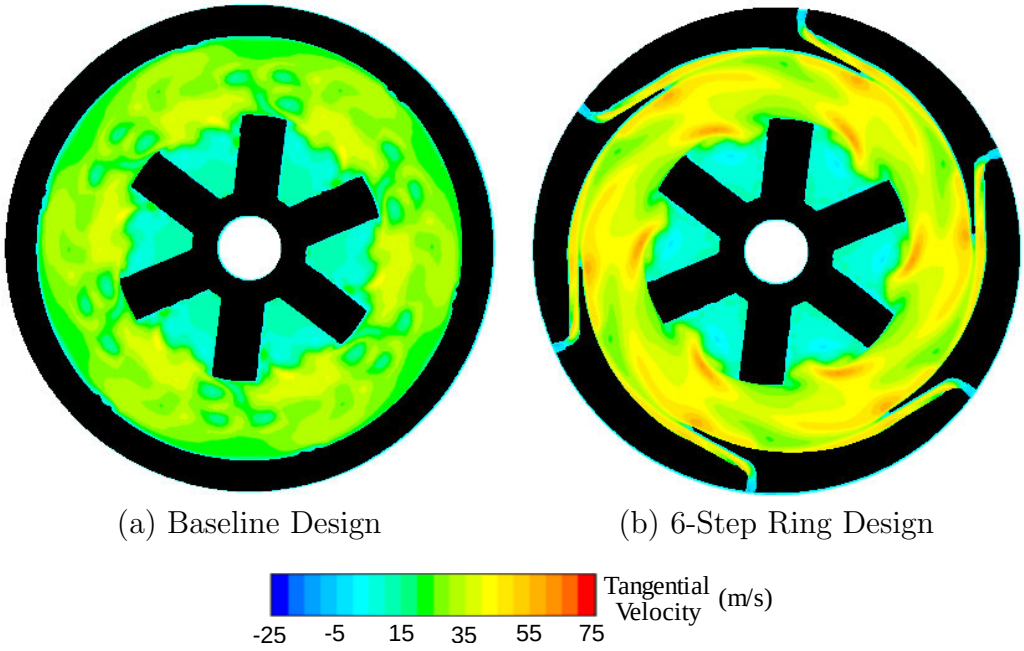

(a) Baseline Design (b) 6-Step Ring Design

Figure 39. 6-Step Ring $\frac{1}{2}$ Cavity Tangential Velocity Contours

4.1.2 Experimental Results.

When experimentally tested, the 6-Step Ring was unable to maintain continuous combustion at the designed cavity airflow split of 50% through the outer ring and 50% through the front plate. When the airflow rate through the outer ring was reduced to 1% of the total airflow into the cavity, sustained combustion was achieved. It was determined that either the flame was being extinguished due to exceeding the centrifugal blowout limits established by Zelina et al. [10], discussed in Section 2.2.1,

or due to a lack of recirculating regions, which are required to maintain combustion as discussed in Section 2.3.

In order to determine the centrifugal loading within the CC without combustion, PIV was used. PIV was conducted using a double-pulsed Nd:Yag laser, a monochrome PCO 1600 camera, a 55 mm f/11 lens, and a particle seeder system, as shown in Figures 40 and 41. The Nd:Yag laser, shown in Figure 41 (c), consisted of two 30 mJ 532 nm laser beams with a 20 μs offset between pulses. The PCO camera had a 33 ms exposure and was positioned 48.3 cm from a quartz window on the back plate of the CC which provided optical access. Silicon carbide particles were housed in a seeder system, shown in Figure 41 (d), which used a pneumatic motor to agitate the system. The vibrations loosened the seed particles which were picked up by a 35 psi air flow and carried out of the seeder. The seed particles were then introduced into the UCC diffuser upstream of the front air drive plate. The particles followed the flow into the CC and passed through a laser sheet at the axial middle of the cavity created by the Nd:Yag laser.

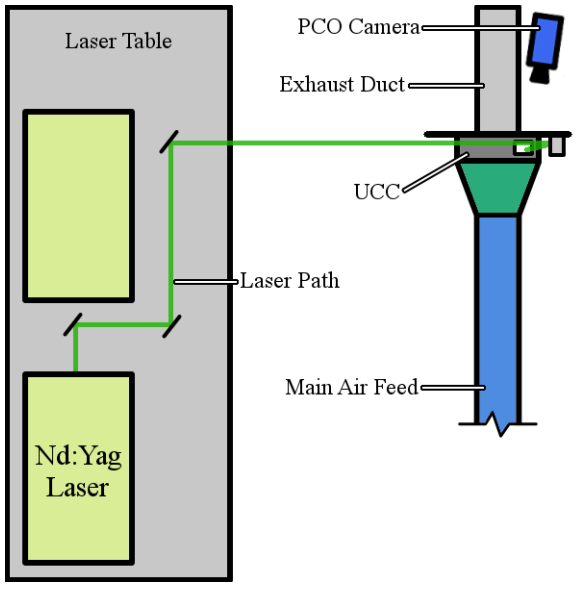

Figure 40. 6-Step PIV Schematic

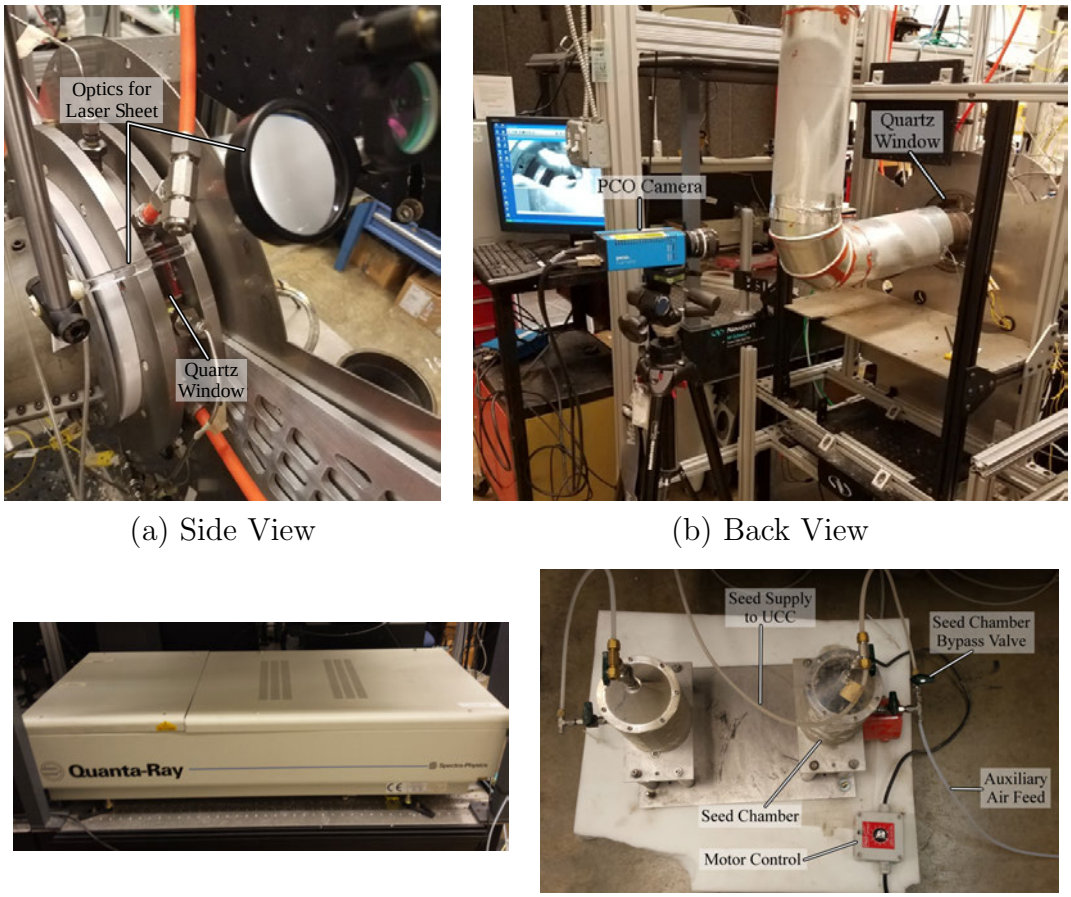

(a) Side View (b) Back View

(c) Nd:Yag Laser (d) Seeder System

Figure 41. 6-Step PIV Setup and Equipment

Standard PIV imaging techniques described in Section 2.7 enabled calculation of the flow velocities. Averaging the values along the middle of the window for the case with a 0.108 kg/s inlet mass flow rate and a 74% core and 26% cavity flow split resulted in a tangential velocity of 28.5 $\pm$ 0.7 m/s which corresponds to the predicted CFD values and a centrifugal loading of 1113 g's. This centrifugal loading is well below the established blowout limits, thus it was determined that there must have been insufficient recirculating regions within the cavity for flame stabilization. Therefore, the CFD was reevaluated to determine if recirculation regions were present. Figure 42 supported this conclusion as the flames within the CC were shown to be floating, and no strong recirculating regions were present.

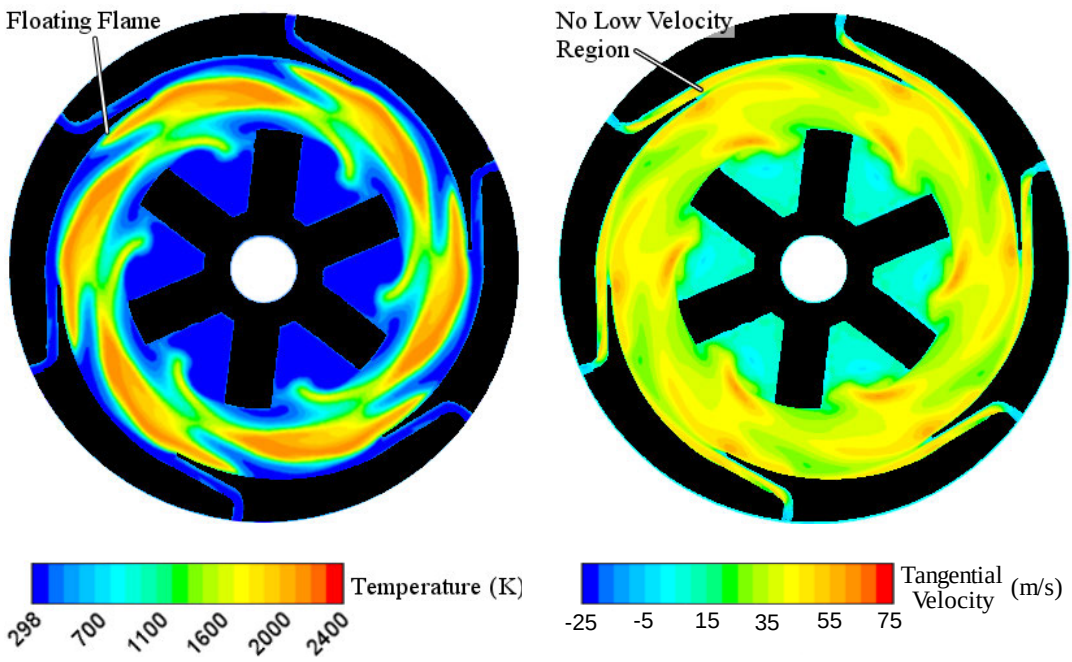

(a) Temperature (b) Tangential Velocity

Figure 42. 6-Step $\frac{1}{2}$ Cavity CFD Contours

4.2 12-Step Ring

The lack of flameholders in the 6-Step Ring was addressed by designing a new outer ring. This new ring, referred to as the 12-Step Ring and shown in Figure 43, incorporated a second set of backward facing steps into the design. The steps were spaced 30° around the outer ring with alternating injection schemes out of the step face, as shown in Figure 43 (b). Six steps remained as designed for the 6-Step Ring where the step face contained both air and fuel inlets. However, every other step only contained two circular fuel inlets at 2.5 mm in diameter, offset such that one fuel inlet was 3.1 mm while the other was 12.7 mm from the front wall of the CC. This offset was incorporated to introduce fuel closer to the front of the cavity with the expectation that the air from the front plate would push it toward the rear of the cavity. The height of each step was consistent with the 6-Step Ring at 6.35 mm.

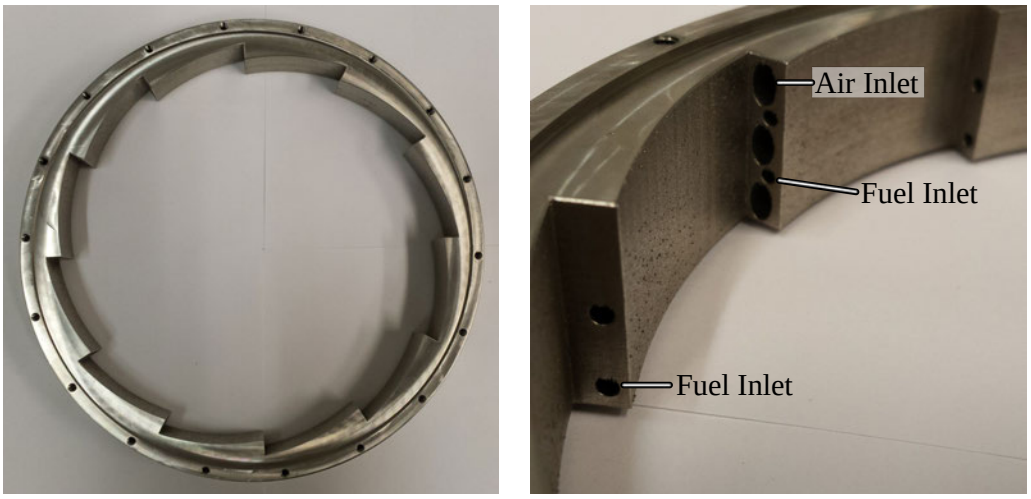

(a) 12-Step Ring (b) Step Face

Figure 43. 12-Step UCC Cavity Outer Ring

Similar to the 6-Step Ring, the internal ducts of the 12-Step Ring, shown in Figure 44, required an additive manufacturing technique. To prevent the 12-Step Ring from lifting off the build plate like the 6-Step Ring, a new build plate was machined out of Inconel by the AFIT Model Shop. The 12-Step Ring was printed by the AniMaL Lab at AFIT on a Concept Laser M2 cusing 3D printer out of Inconel. The new build plate prevented the part from lifting during the printing process and prevented issues with the air inlets breaking through the sides of the ring. The resulting part was brought to the AFIT Model Shop where it was cut off the build plate and post-processed in the same manner as the 6-Step Ring.

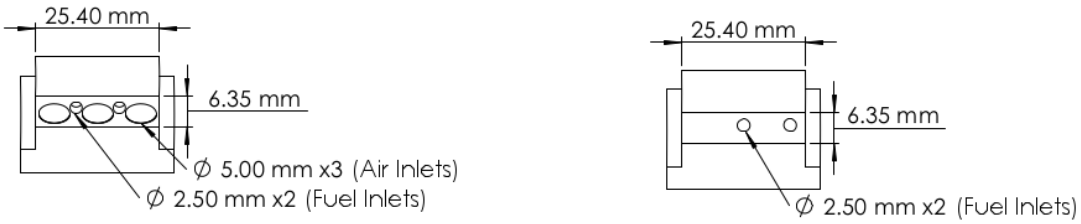

(a) Air and Fuel Step Face (b) Fuel Only Step Face

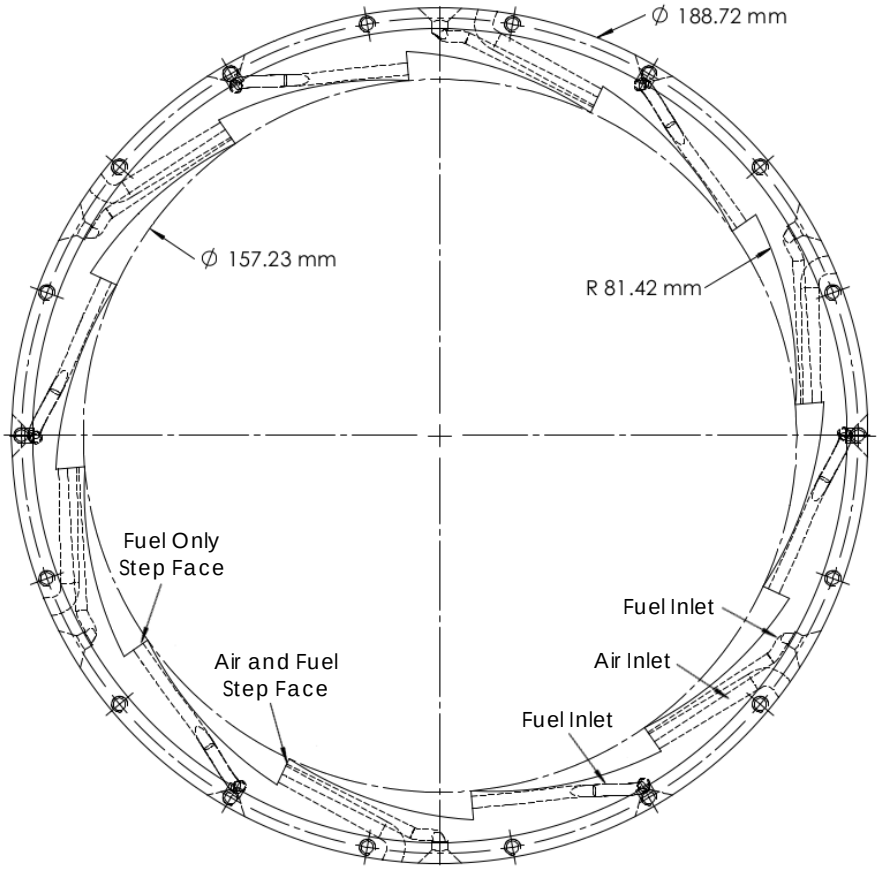

(c) Side View Showing Internal Ducts

Figure 44. 12-Step Ring Dimensions

4.2.1 CFD Evaluation.

The 12-Step design was analyzed computationally using the same settings as the baseline and 6-Step designs outlined in Section 3.5, with tangential velocity contours shown in Figure 45. The average 12-Step tangential velocity was calculated to be 36.9 m/s at a 0.72 cavity equivalence ratio, 0.108 kg/s inlet mass flow rate, a 74% to the core and 26% to the cavity flow split, and 50% of the cavity air through the front plate and outer ring, correlating to a centrifugal loading of 1867 g's. This is a 262% increase in loading over Cottle's design, and a 68% increase from the 6-Step design.

The increased circumferential loading between the 12-Step and 6-Step designs was due to the additional steps of the 12-Step Ring reducing the volume of the cavity. Although the volume was reduced, the same mass flow rate was entering the cavity, and thus the velocity increased to compensate.

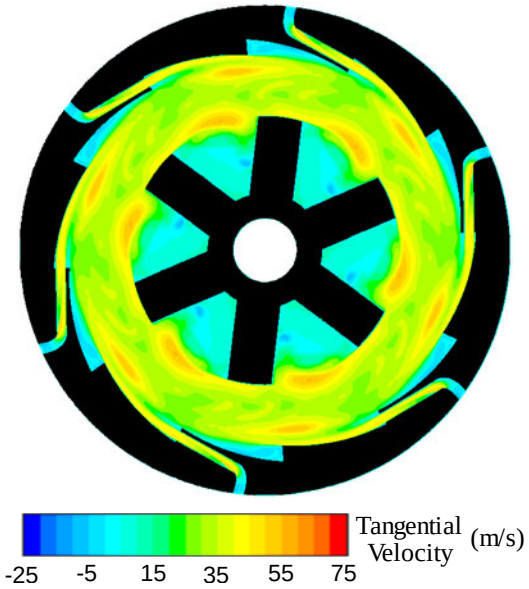

Figure 45. 12-Step Ring $\frac{1}{2}$ Cavity Tangential Velocity Contours

The CFD was then analyzed for low velocity recirculating regions, which were found to be present behind the steps with only fuel inlets, the light blue region on the outer diameter in Figure 45. Furthermore, CFD evaluation of the 12-Step design at a 0.108 kg/s mass flow rate and 0.72 cavity equivalence ratio showed large temperature gradients, as displayed in Figure 46 (a). The design showed hot temperatures along the outer and inner diameter with a cool zone in the middle. At the total airflow split of 74% to the core and 26% to the cavity and the cavity airflow split of 50% through the front plate and 50% through the outer ring, the combustion zones did not fully utilize the volume of the CC, which is undesirable.

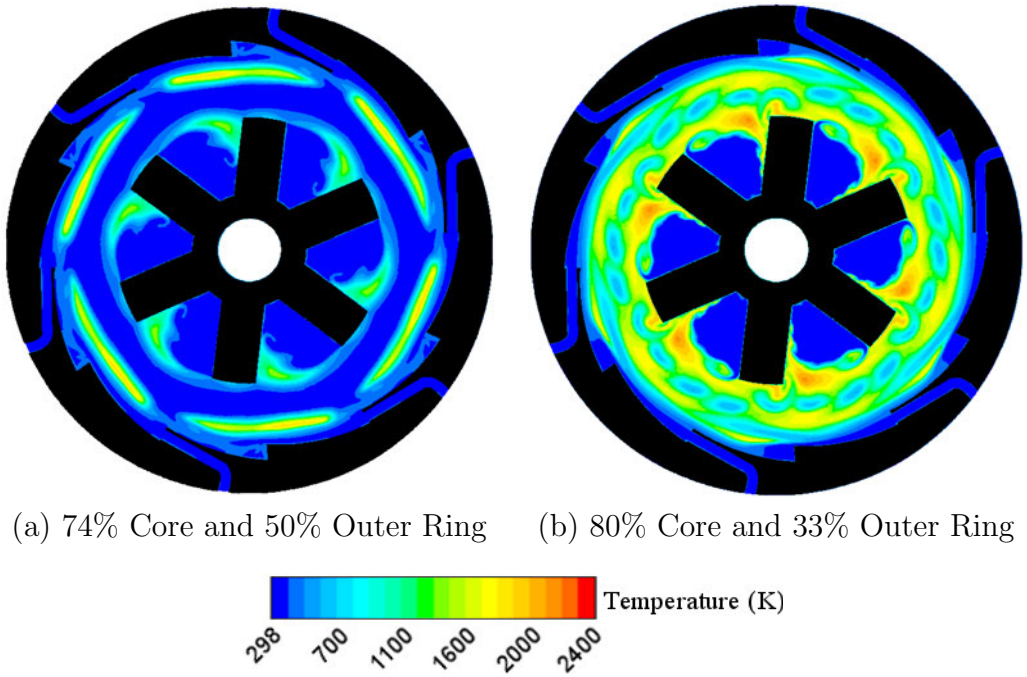

(a) 74% Core and 50% Outer Ring (b) 80% Core and 33% Outer Ring

Figure 46. 12-Step Ring $\frac{1}{2}$ Cavity Temperature Contours

4.2.2 Comparison to Baseline Design.

The flow conditions experimentally tested on Cottle's design in Section 3.5 were subsequently tested with the 12-Step design, however this resulted in either unstable combustion or low CC temperatures at the 74% core flow and 50% outer ring airflow splits, as shown in Figure 46 (a). Due to the control over the UCC, the airflow splits were varied to improve the cavity combustion dynamics. Stable combustion was achieved at a total airflow split of 80% to the core and 20% to the cavity and a cavity airflow split of 66% through the front plate and 33% through the outer ring. This condition was subsequently evaluated using CFD produced the temperature contour shown in Figure 46 (b). These new airflow splits improved both combustion stability and performance of the 12-Step design as the combustion was shown to utilize a large percent of the CC volume. These airflow splits were then experimentally tested to parameterize the 12-Step Ring at cavity equivalence ratios, ϕ_{Cav}, of 0.96, 1.47, and

1.73, and total air mass flow rates, $\dot{m}_{in}$, of 0.056, 0.084, 0.101 and 0.112 kg/s, as shown in Table 5. These flow conditions resulted in global equivalence ratios, ϕ_{Global}, ranging from 0.20 to 0.36.

Table 5. 12-Step Ring Test Cases

Case	ϕ_{Global}	ϕ_{Cav}	$\dot{m}_{in}$ (kg/s)	$\dot{m}_{core}$ (kg/s)	$\dot{m}_{cav}$ (kg/s)	$\dot{m}_f$ (kg/s)
1	0.20	0.96	0.056	0.045	0.011	0.0007
2	0.20	0.96	0.084	0.067	0.017	0.0010
3	0.20	0.96	0.101	0.081	0.020	0.0012
4	0.20	0.96	0.112	0.090	0.022	0.0014
5	0.31	1.47	0.056	0.045	0.011	0.0010
6	0.31	1.47	0.084	0.067	0.017	0.0016
7	0.31	1.47	0.101	0.081	0.020	0.0019
8	0.31	1.47	0.112	0.090	0.022	0.0021
9	0.36	1.73	0.056	0.045	0.011	0.0012
10	0.36	1.73	0.084	0.067	0.017	0.0019
11	0.36	1.73	0.101	0.081	0.020	0.0022
12	0.36	1.73	0.112	0.090	0.022	0.0024

Performance of the 12-Step Ring was quantified through evaluation of the average temperatures within the CC along with the exit temperature profile of the UCC. These values were then compared to the results in Section 3.5. The average of the temperatures at the $\frac{1}{4}$, $\frac{1}{2}$, and $\frac{3}{4}$ axial cavity locations for each flow rate and equivalence ratio are found in Figure 47 while the $\frac{1}{2}$ cavity temperatures compared to the total mass flow rate are found in Figure 48. For the 12-Step Ring at a set airflow rate the average cavity temperature decreased with increasing cavity equivalence ratio. With the rich equivalence ratios in the cavity, temperature decreased as the equivalence ratio increased beyond the stoichiometric conditions. The cavity temperatures of the 12-Step design were lower than those of the baseline design. Although there was more unburned fuel, the combusting regions in the baseline cavity design were closer to stoichiometric. The 12-Step design successfully improved the air and fuel mixing causing the majority of the cavity to combust at higher equivalence ratios.

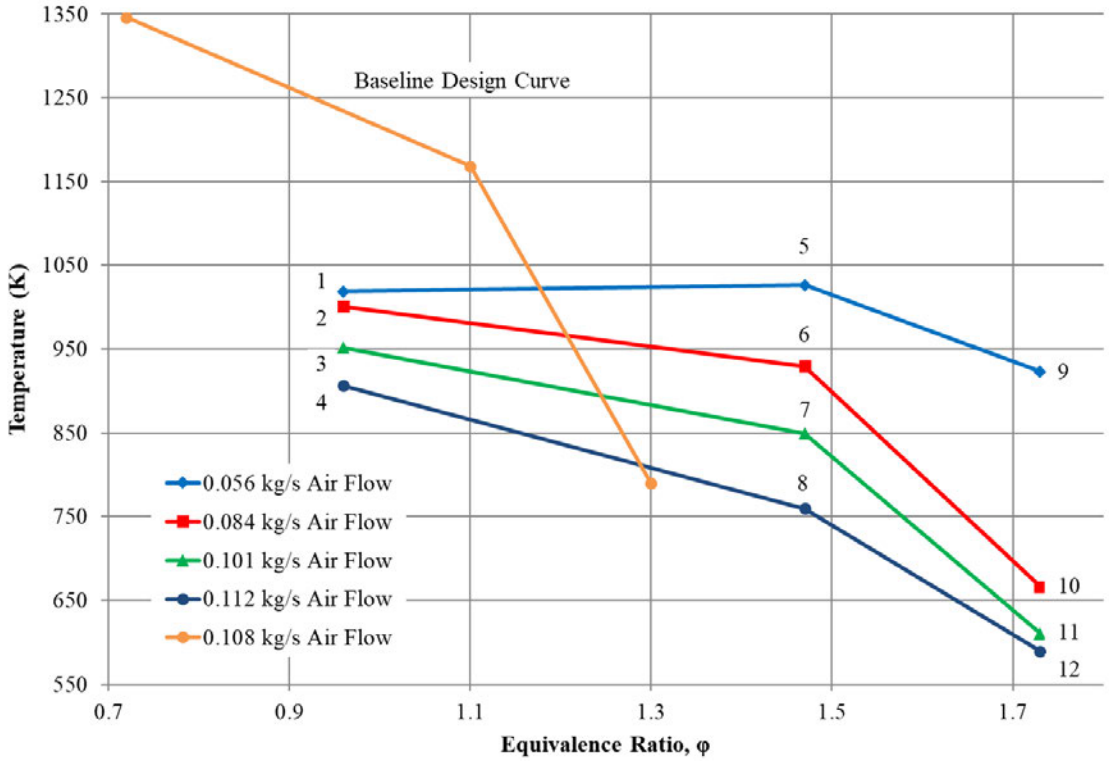

Figure 47. Average Cavity Temperature vs. Cavity Equivalence Ratio

Within the cavity the highest temperatures were at the $\frac{1}{2}$ cavity position, with a peak temperature of 1216 K occurring in Case 1. For all cavity equivalence ratios, the $\frac{1}{2}$ cavity temperature was then seen to decrease with an increasing total airflow. From Case 1 to Case 4, the $\frac{1}{2}$ cavity temperature decreased by 16%. At a 1.47 cavity equivalence ratio, the change from increasing the total air mass flow rate from 0.056 kg/s, Case 5, to 0.112 kg/s, Case 8, resulted in a 24% decrease in $\frac{1}{2}$ cavity temperature. From Case 9 to Case 12, a cavity equivalence ratio of 1.73, the $\frac{1}{2}$ cavity temperature experienced the greatest decrease of 34%. The temperature decrease was caused by the increased mass flow rate shifting combusting regions from $\frac{1}{2}$ cavity axial downstream to $\frac{3}{4}$ cavity, and eventually into the HGV.

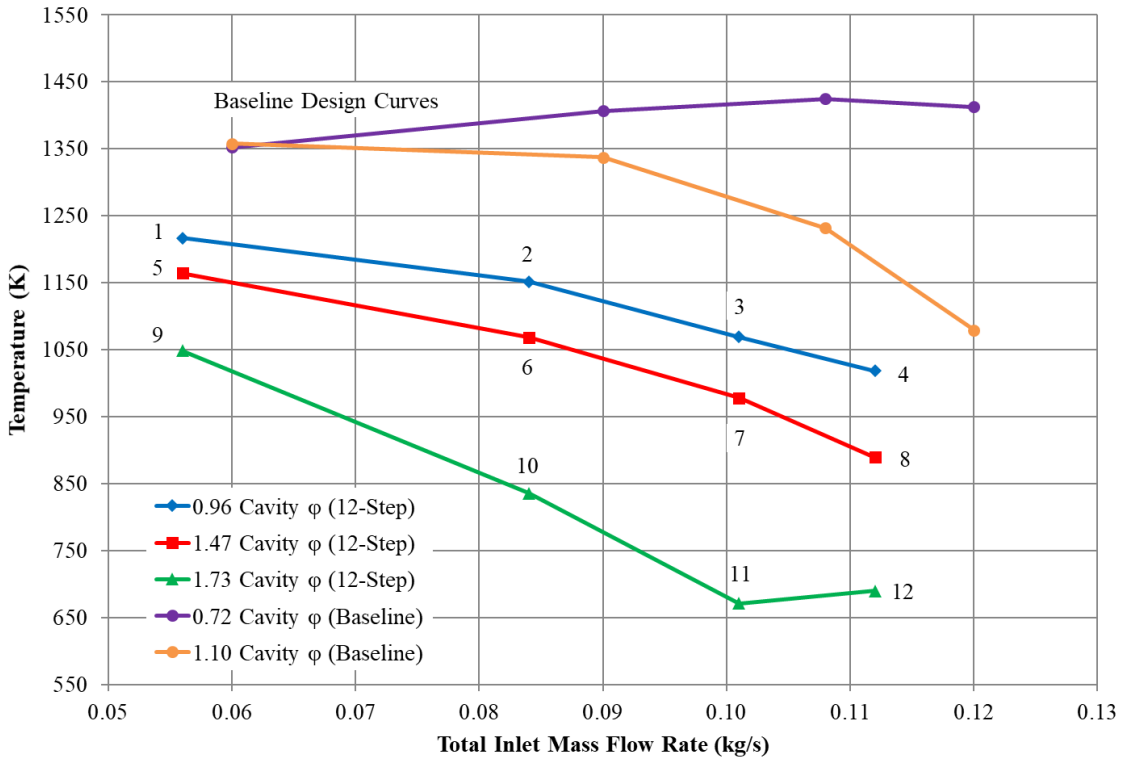

Figure 48. $\frac{1}{2}$ Cavity Temperature vs. Total Air Mass Flow

The exit temperature profile of the UCC was also evaluated and compared between the 12-Step design and Cottle's design. The maximum temperature, T_{max}, average temperature, T_{avg}, and pattern factor for each case are shown in Table 6. Despite the cavity flow differences, the 12-Step Ring and the Stock design are compared between similar global equivalence ratios and total mass flow rates as these values are within 6% and 7%, respectively. The average exit plane temperature of the 12-Step Ring was higher than that of the stock design for all cases with the greatest increase being from 598 K to 839 K, corresponding to a 40% increase, for Case 11. This case was at the highest equivalence ratio, where the baseline design had trouble maintaining combustion. The ability of the 12-Step design to operate at a global equivalence ratio of 0.36 at all the tested total air mass flow rates proved it extended the operating range of the UCC. The lowest increase in average exit temperature was from 631 K to 677 K, corresponding to a 7% increase, for Case 3.

Table 6. Exit Temperature Profile Characteristics

Case	ϕ_{Global}	12-Step Ring				Baseline Design			
		$\dot{m}_{in}$ (kg/s)	T_{max} (K)	T_{avg} (K)	Pattern Factor	$\dot{m}_{in}$ (kg/s)	T_{max} (K)	T_{avg} (K)	Pattern Factor
1	0.20	0.056	769	667	0.27	0.060	822	613	0.67
2	0.20	0.084	810	692	0.30	0.090	911	636	0.82
3	0.20	0.101	799	677	0.32	0.108	894	631	0.79
4	0.20	0.112	792	664	0.34	0.120	892	618	0.86
5	0.31	0.056	1015	800	0.42	0.060	1035	745	0.65
6	0.31	0.084	1036	826	0.40	0.090	1076	731	0.80
7	0.31	0.101	1083	822	0.49	0.101	949	663	0.79
8	0.31	0.112	1032	790	0.48	0.120	931	658	0.76
9	0.36	0.056	1119	866	0.44	0.060	—	—	—
10	0.36	0.084	1134	888	0.41	0.090	—	—	—
11	0.36	0.101	1073	839	0.42	0.108	792	598	0.64
12	0.36	0.112	996	770	0.47	0.120	—	—	—

The 12-Step design also experienced reductions in the pattern factor of up to a 63%, approaching the desirable range of 0.25 to 0.43 [7]. The best pattern factors were obtained at the global equivalence ratio of 0.20. For these cases, the reactions were well within the CC. As the equivalence ratio increased, more unburned fuel made it into the secondary reaction zone within the HGV which caused an increase in exit temperatures. At the highest total air mass flow rates the pattern factors increased which was likely due to the increased core velocity preventing the products from fully mixing out within the HGV. The overall reduction in pattern factors compared to the baseline design indicates a significant improvement of the exhaust gas uniformity across the span.

The exit temperature contour maps for global equivalence ratios of 0.20, 0.31, and 0.36 can be found in Figure 49. The 12-Step Ring design produced a more uniform temperature profile at a global equivalence ratio of 0.20 when compared to the stock design, as shown in Figures 49 (a), (b), (c), and (d). The hot products found on the outer diameter of the passage in the stock design can be seen to have penetrated

radially inward in the 12-Step Ring design. This pattern is also found in the global equivalence ratio of 0.31 profiles shown in Figures 49 (e), (f), (g), and (h). More heat was transported to the inner diameter of the passage where the minimum temperature was raised from 550K to 700 K enabling more work extraction by the downstream rotor. The passage outer diameter of the 12-Step design was found to experience a higher peak temperature of 1083 K in the 0.101 kg/s total airflow case, a 14% increase from the 949 K peak experience in the stock design. The highest exit profile temperatures for the 12-Step Ring design were at a global equivalence ratio of 0.36, shown in Figures 49 (i) and (j). The profiles in Figures 49 (e), (g) and (i) displayed an increase in the temperature levels compared to those in Figures 49 (f), (h) and (j), respectively. By comparing the average exit temperatures with the adiabatic flame temperature of propane, the amount of fuel burn for both cases can be compared. For a 0.36 global equivalence ratio, the average exit temperature for the 12-Step design was 69% while the baseline design was 49% the adiabatic flame temperature. This indicates the 12-Step design had a more complete burn of the reactants.

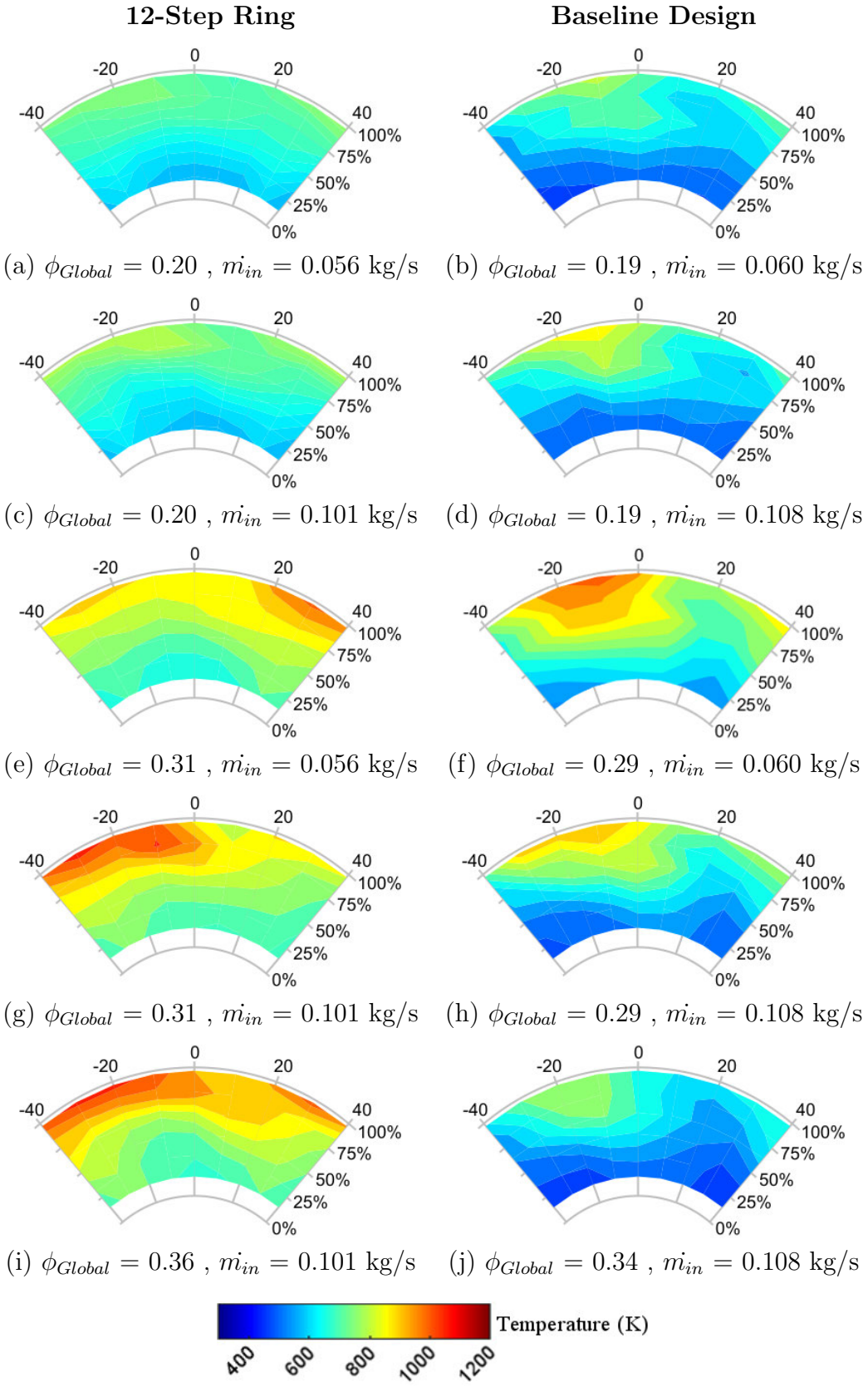

(a) $\phi_{Global} = 0.20$, $\dot{m}_{in} = 0.056$ kg/s (b) $\phi_{Global} = 0.19$, $\dot{m}_{in} = 0.060$ kg/s

(c) $\phi_{Global} = 0.20$, $\dot{m}_{in} = 0.101$ kg/s (d) $\phi_{Global} = 0.19$, $\dot{m}_{in} = 0.108$ kg/s

(e) $\phi_{Global} = 0.31$, $\dot{m}_{in} = 0.056$ kg/s (f) $\phi_{Global} = 0.29$, $\dot{m}_{in} = 0.060$ kg/s

(g) $\phi_{Global} = 0.31$, $\dot{m}_{in} = 0.101$ kg/s (h) $\phi_{Global} = 0.29$, $\dot{m}_{in} = 0.108$ kg/s

(i) $\phi_{Global} = 0.36$, $\dot{m}_{in} = 0.101$ kg/s (j) $\phi_{Global} = 0.34$, $\dot{m}_{in} = 0.108$ kg/s

Figure 49. 12-Step Design Exit Temperature Profiles Compared to Baseline

4.2.3 Fuel and Airflow Split Study.

Tests with the 12-Step Ring revealed that the combustion performance of the UCC was dependent on the percent of the total air injected into the CC and the amount of cavity air injected through the front plate compared to the amount through the outer ring. The CFD temperature contours at the axial middle of the cavity that were shown in Figure 46 revealed that at a cavity airflow split of 50% combustion did not fill the cavity and a large cool region existed at half the cavity height. However, changing the airflow split of 20% of the total air into the cavity with 66% of that through the front plate resulted in combustion filling the cavity and the only cool areas existed at the exits of the inlets from the front plate and step faces, as seen in Figure 46 (b). These drastically different contours illustrated the importance of the airflow splits on combustion within the cavity which was important to understand, thus an operating map of its effect was created.

The total air mass flow rate, $\dot{m}_{in}$, and global equivalence ratio, ϕ_{Global}, was set for each test while the percentage of the total air introduced into the cavity, percentage of cavity air through the front plate, and the percentage of fuel introduced through the fuel only steps were varied. The total air mass flow rate was manipulated using mass flow controllers and tests were performed at 0.060, 0.108, and 0.120 kg/s. The global equivalence ratio was held constant at 0.36 by maintaining the total fuel flow at each total air mass flow rate. The percent of the total air introduced into the cavity and the percent of the cavity air introduced through the front plate was controlled in combination of adjusting the variable diffuser, discussed in Section 3.2, and the air supply for the outer ring, controlled by the 3.81 cm airline LabView setting discussed in Section 3.3. With this control, the UCC was evaluated from 10% to 50% of the total air introduced to the cavity over a range of 10% to 90% of the cavity air introduced through the front plate. Finally, the independent fuel control between the

step types using the Alicat and Brooks mass flow controllers allowed the ideal split of fuel between the fuel only step, controlled by the Alicat, and the fuel and air step, controlled by the Brooks, to be found. This created a three-dimensional performance map for each total air mass flow rate and global equivalence ratio.

First, the effect of the fuel split was evaluated at a total air mass flow rate of 0.108 kg/s. The total fuel mass flow rate was held constant at 0.0025 kg/s, resulting in a 0.36 global equivalence ratio, while the fuel mass flow through the Alicat and Brooks flow controllers were manipulated, as shown in Table 7. The UCC performance was evaluated using the cavity thermocouples and the thermocouple rake. For this test, the thermocouple rake was held stationary at -20° circumferentially and 9.65 mm radially, which positioned the thermocouples in the region where peak exit temperatures were observed. The temperature measurements in the cavity, at the $\frac{1}{4}$, $\frac{1}{2}$, and $\frac{3}{4}$ axial locations, and at the exit were separately averaged to give an average cavity and average exit temperature for each case.

Table 7. 12-Step Fuel Split Evaluation Cases

Case	Fuel Only Step (Alicat)	Air & Fuel Step (Brooks)
1	50%	50%
2	60%	40%
3	70%	30%
4	80%	20%
5	90%	10%
6	100%	0%
7	50%	50%
8	40%	60%
9	30%	70%
10	20%	80%
11	10%	90%
12	0%	100%

The resulting average exit and cavity temperatures are shown in Figure 50, where the blue line was the average cavity temperature and the red line was the average exit temperature. The average cavity temperature was seen to increase by 101 K with an increase of fuel to the fuel only step, however this was most likely due to the position of the cavity thermocouples and the shifting of the combusting regions within the cavity off of the thermocouple point measurement. The exit temperature showed very little change with fuel split where the average of all cases was 760 K, represented by the black dashed line in Figure 50, with a standard deviation of 11 K. The combustor exit temperature represents a preferred performance parameter than the cavity temperature because the temperature rise over the combustor within an engine drives the available power. Furthermore, in the UCC the cavity thermocouples do not fully represent the characteristics of the flow within the cavity, and the high temperature gradients shown in the CFD models, such as those found in Figure 46,

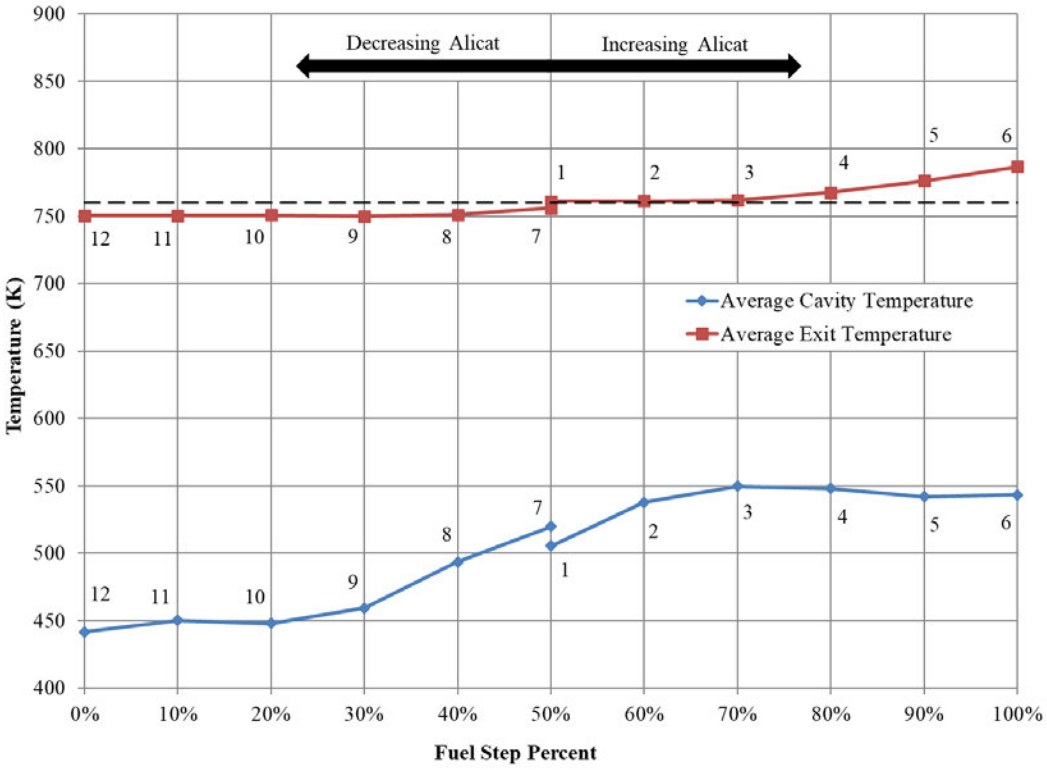

Figure 50. 12-Step Fuel Split Evaluation Plot

mean the location of the thermocouples greatly changes the measured cavity temperatures. As there was little change in the exit temperature, UCC performance was deemed independent of the fuel split. For all further tests both step types were controlled solely by the Brooks mass flow controller resulting in a fuel split of 50% between both step types.

Next the effect of the airflow split was evaluated by holding the total air mass flow rate of 0.108 kg/s. The total fuel mass flow rate was held constant at 0.0025 kg/s, resulting in a 0.36 global equivalence ratio, with a 50% split between the fuel only step and the fuel and air step. Both the core to cavity and the front plate to outer ring airflow splits were varied. The core to cavity split determined the percent of total air sent into the CC. For example, an 80% core to cavity split resulted in 0.022 kg/s of air entering the cavity out of the total 0.108 kg/s, while the remaining 0.086 kg/s bypassed the cavity and flowed through the core. The front plate to outer ring split determined where the cavity airflow entered from. For example, with an 80% core to cavity split and a 60% front plate to outer ring split, 0.009 kg/s of the 0.022 kg/s cavity airflow entered through the outer ring, while the remaining 0.013 kg/s entered through the front plate.

To populate an operating map over the range of airflow splits, the 24 test points in Table 8 were evaluated. While the global equivalence ratio was held constant, the cavity equivalence ratio varied with the core to cavity split from 0.72 to 3.60. Similar to evaluation of the fuel split, the UCC performance was evaluated using the average exit temperature recorded by the thermocouple rake, with the rake held stationary at -20° circumferentially and 9.65 mm radially. The variable diffuser controlled the core to cavity split but to determine the necessary position, the pressure differential, ΔP, between static and total pressure of the core flow within the diffuser was used, as discussed in Section 3.2. The required pressure differential values for the test

points can be found in Figure 51. With the diffuser splitting the flow using a pressure balance, there were certain pressure differentials which could not be obtained due to back pressure on the front plate or the limits of motion for the variable diffuser. This pressure differential limit has been found to be dependent on the total airflow, outer ring airflow, and combustion stability.

Table 8. 12-Step Airflow Split Test Points

Test Point	Core to Cavity Split	Front Plate to Outer Ring Split	ϕ_{Cav}
1	50%	10%	0.72
2	50%	70%	0.72
3	50%	90%	0.72
4	55%	80%	0.80
5	60%	70%	0.90
6	60%	80%	0.90
7	65%	90%	1.03
8	70%	50%	1.20
9	70%	70%	1.20
10	70%	80%	1.20
11	75%	60%	1.44
12	75%	70%	1.44
13	75%	80%	1.44
14	80%	40%	1.80
15	80%	60%	1.80
16	80%	90%	1.80
17	85%	50%	2.40
18	85%	80%	2.40
19	90%	10%	3.60
20	90%	20%	3.60
21	90%	30%	3.60
22	90%	40%	3.60
23	90%	70%	3.60
24	90%	90%	3.60

The 24 test points are shown in Figure 52 with the boxed numbers next to the points being the average exit temperature of each point. The test points were also labeled as either “Combusting”, where continuous combustion occurred, “Diffuser

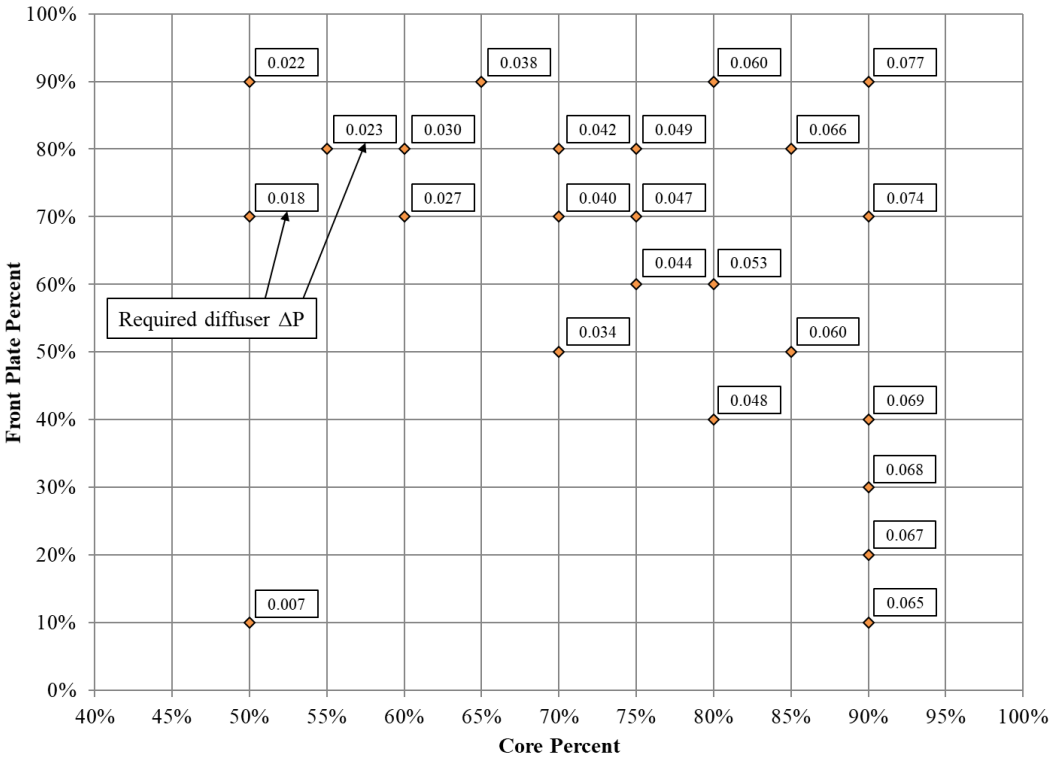

Figure 51. Required Pressure Differential Map, $\dot{m}_{in} = 0.108kg/s$

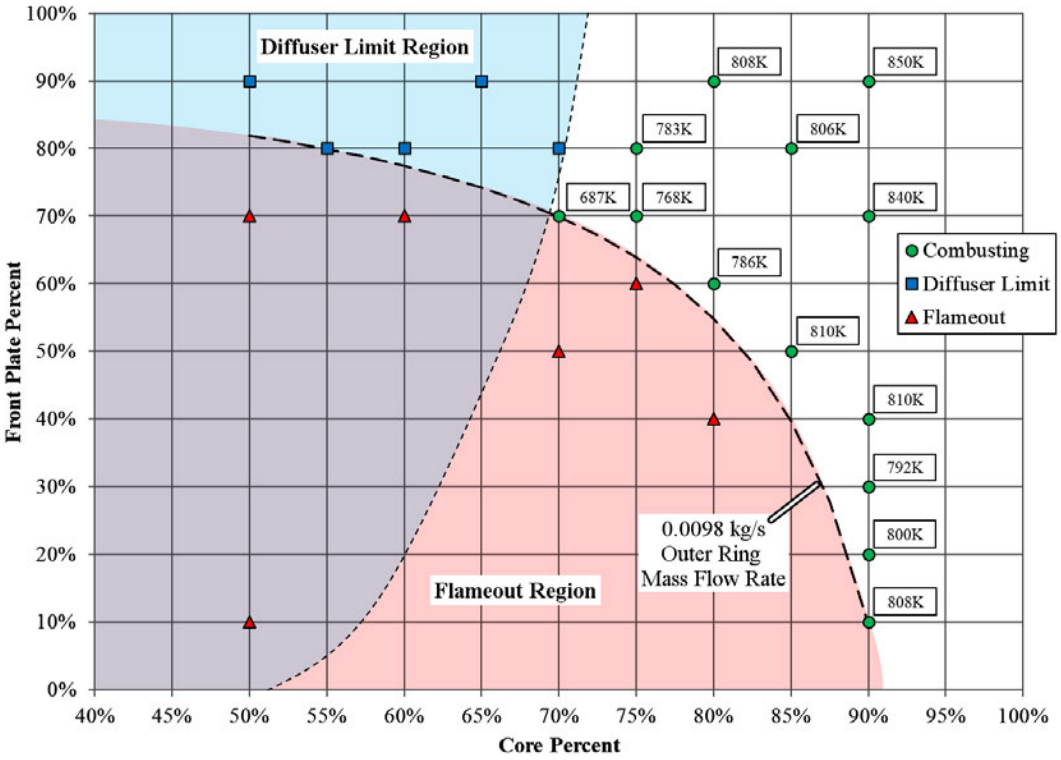

Figure 52. Average Exit Temperature Operating Map, $\dot{m}_{in} = 0.108kg/s$

Limit", where the diffuser could not reach the required pressure differential for that point, or "Flameout", where combustion could not occur. Using this a flameout region and diffuser limit region were estimated, shown as red and blue, respectively. It was noticed that flameout occurred when the setpoint on the 3.81 cm line was 3.25%, which equates to an air mass flow rate of 0.0098 kg/s through the outer ring, or about 9% of the total air mass flow rate.

The same test was conducted two more times with the total air mass flow rate held constant at 0.060 kg/s and then at 0.120 kg/s. The total fuel mass flow rate was held constant at 0.0014 kg/s and 0.0028 kg/s, respectively, resulting in a 0.36 global equivalence ratio. With the different total air mass flow rates, new pressure differentials were calculated and are displayed in Figures 53 and 54 for total air mass flow rates of 0.060 kg/s and 0.120 kg/s, respectively.

The average exit temperature for each point are shown in Figures 55 and 56 for a total air mass flow rate of 0.060 kg/s and 0.120 kg/s, respectively. Consistent with the 0.108 kg/s case, the operating region is located in the top right region of the plot. Reviewing the flameout points for the 0.120 kg/s case, the setpoint on the 3.81 cm line was about 3.60%, which equates to an air mass flow rate of 0.0108 kg/s through the outer ring, or about 9% of the total air mass flow rate which is consistent with the 0.108 kg/s case. For the 0.60 kg/s case, the points were first tested without combustion to determine the diffuser limit and reduce the dataset. This resulted in no flameout points tested, however using the trend from the other two cases where flameout occurred with a greater than 9% of the total air mass flow rate through the outer ring, a flameout region was approximated as greater than 9% of the total air mass flow rate being injected through the outer ring, which equated to a setpoint on the 3.81 cm air line of 1.80%, or 0.0054 kg/s, and is shown in Figure 55.

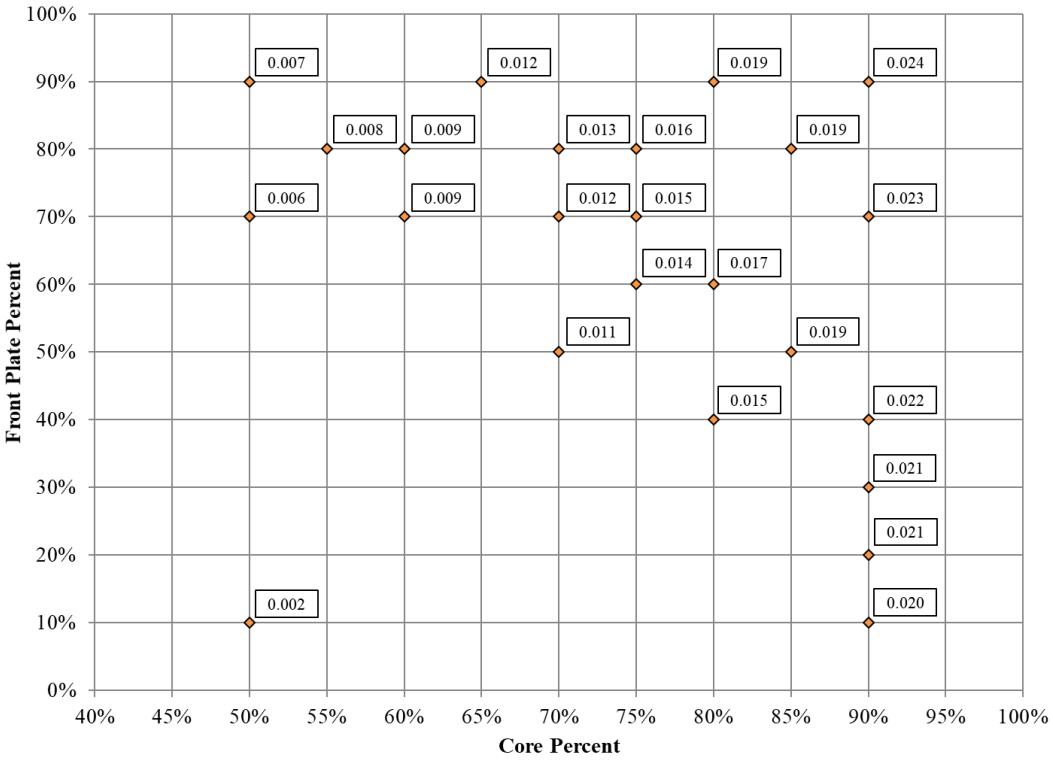

Figure 53. Required Pressure Differential Map, $\dot{m}_{in} = 0.060 kg/s$

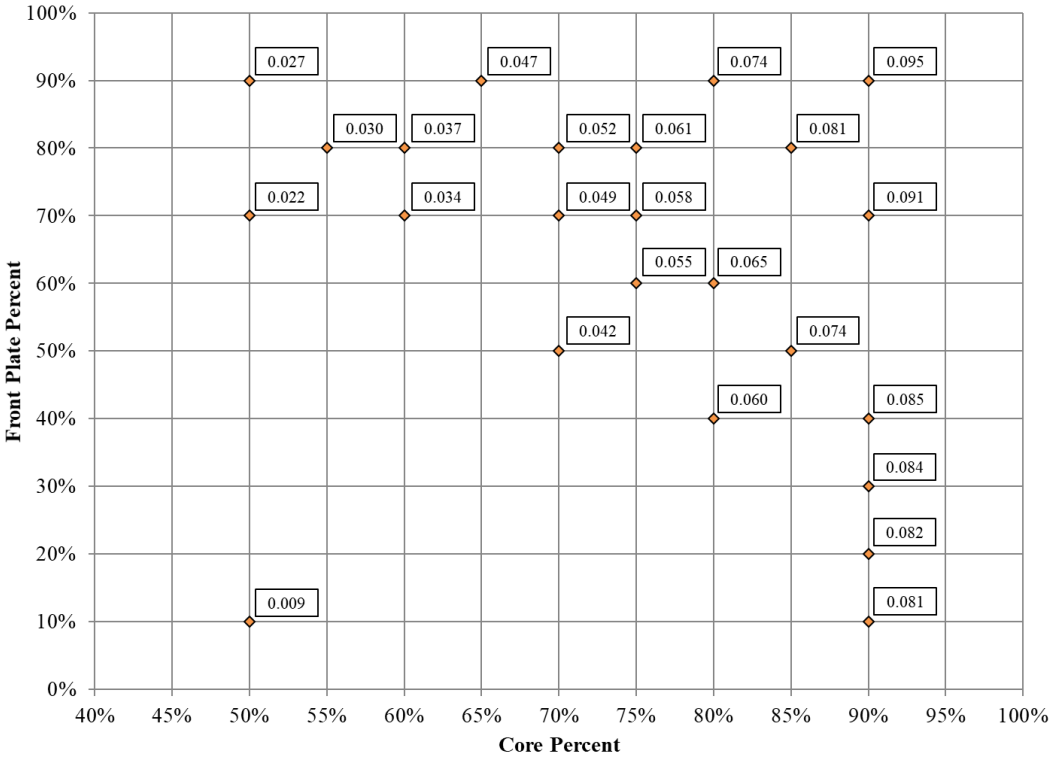

Figure 54. Required Pressure Differential Map, $\dot{m}_{in} = 0.120 kg/s$

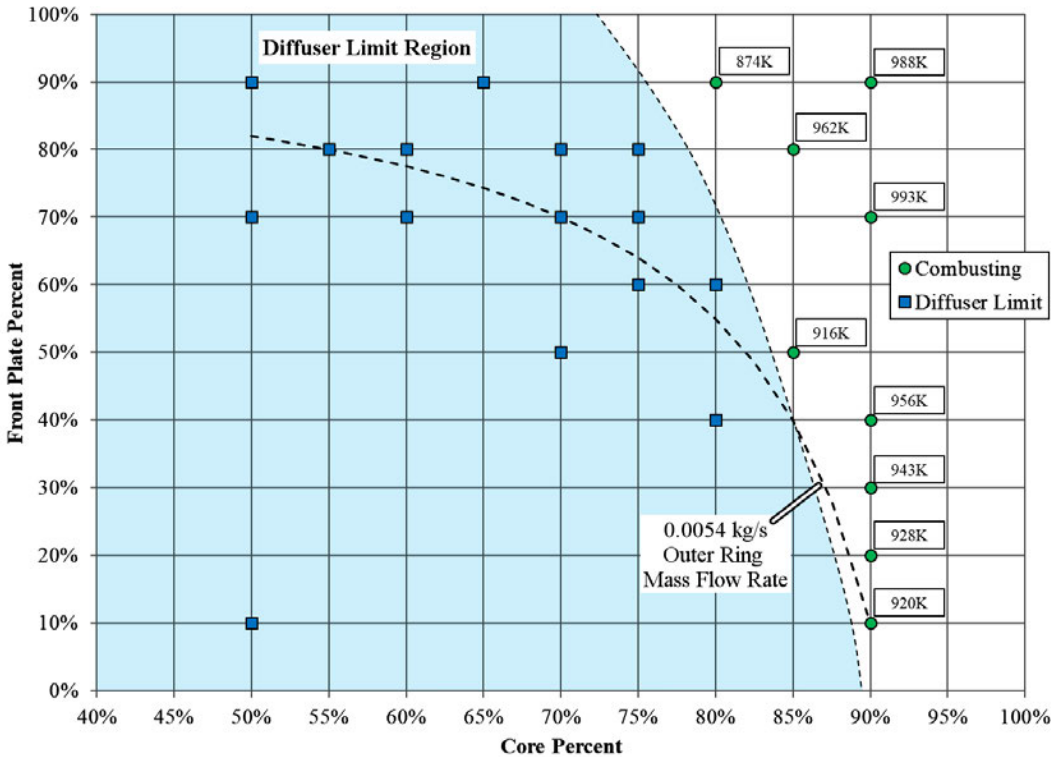

Figure 55. Average Exit Temperature Operating Map, $\dot{m}_{in} = 0.060kg/s$

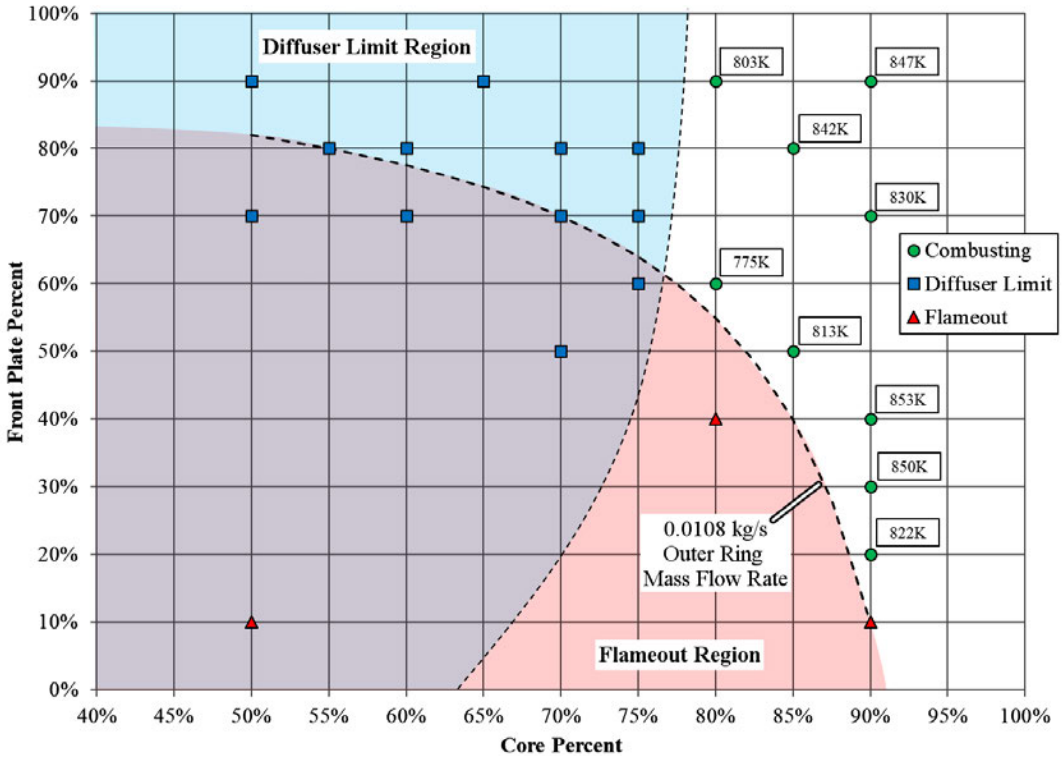

Figure 56. Average Exit Temperature Operating Map, $\dot{m}_{in} = 0.120kg/s$

Reviewing all three cases, it is shown that the peak temperature rise across the combustor was at the top right portion of the plot with a high airflow percent through the core and front plate. The highest exit temperature was 988 K with a total air mass flow rate of 0.060 kg/s at 90% through the core and 90% through the front plate. However at this mass flow rate, the operating region was greatly reduced due to the diffuser limit, and the accoustic level of the UCC was around 91 dB. The best operating range was at a total air mass flow rate of 0.108 kg/s where the exit temperatures were high and the accoustic level was around 88 dB.

4.3 Back Plate Injection

A different approach to solve the fuel build up on the outer diameter of the CC was to inject fuel in a different location. The back plate was redesigned to allow fuel to be injected into the CC from the rear versus the outer diameter. The new design, shown in Figures 57 (a) and (b), contained twelve 6.15 mm diameter fuel injection holes angled 45° off normal into the direction of the cavity swirl. The twelve injectors existed as two sets of six equally spaced around the ring with one set 7.73 cm radially outward and the other six 6.72 cm radially outward from the center of the back plate. Six of the fuel inlets were connected to an Alicat MCR-250SLPM-D-40X55 mass flow controller, while the other six were capped off or filled with a thermocouple, as shown in Figure 57 (c). The Alicat allowed the fuel flow through the back plate to be controlled independently from the fuel flow through the outer ring. Metal tubing was used as fuel lines which were connected to a 90° Swagelok elbow, to prevent interference of the fuel fitting with the collar, which screwed directly into the back plate.

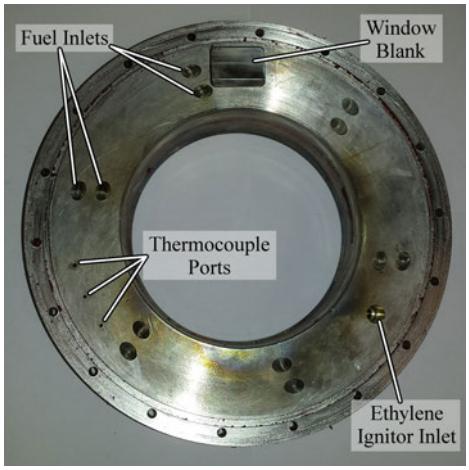

(a) Cavity Side

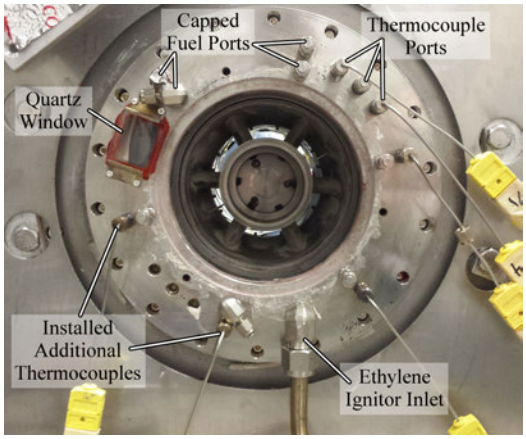

(b) Exterior Side

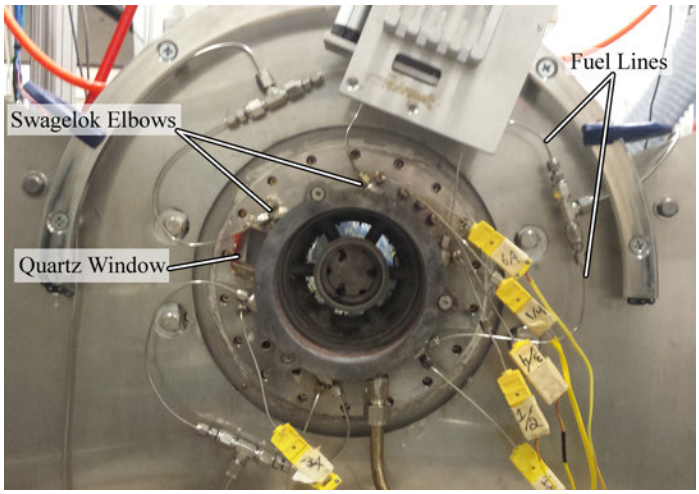

(c) Fuel Lines Installed

Figure 57. Redesigned UCC Back Plate With Fuel Injectors

The new back plate was also designed to resist warping. The original back plate was 1.27 cm thick and the thermal loads caused the plate to need to be machined regularly due to warping. The new back plate was built to be 2.41 cm thick, greatly increasing the thermal mass and reducing warping. Similar to t back plate, the new back plate had three thermocouple ports for measurement of combustion temperatures at the $\frac{1}{4}$, $\frac{1}{2}$, and $\frac{3}{4}$ cavity axial locations, however unused fuel ports were able to house additional thermocouples. The new back plate also contained a cutout for a

rectangular quartz window 1.91 cm by 2.54 cm, which was a significant reduction in area from Cottle's back plate, however a larger window would interfere with the fuel inlets on the back plate. The new design was machined by the AFIT Model Shop out of Hastelloy, and the quartz window was purchased from Quality Quartz Engineering.

4.3.1 Experimental Results.

The effects of injecting fuel through the back plate was studied at total air mass flow rates, $\dot{m}_{in}$, of 0.060, 0.108, and 0.120 kg/s and a constant global equivalence ratio, ϕ_{Global}, of 0.36. The percent of fuel entering the cavity through the back plate was varied between 0% and 30%, as shown in Table 9. Each case contained the 24 test points outlined in Table 8, and the results of Cases 1, 5, and 9 were discussed in Section 4.2.3. The fuel was introduced through the six fuel inlets at 6.72 cm radially.

Table 9. Back Plate Fuel Injection Cases

Case	Total Air Flow Rate (kg/s)	Back Plate Percent	Back Plate Fuel Flow (kg/s)	Outer Ring Fuel Flow (kg/s)
1	0.108	0%	0	0.00249
2	0.108	10%	0.00025	0.00224
3	0.108	20%	0.00050	0.00199
4	0.108	30%	0.00075	0.00174
5	0.060	0%	0	0.00138
6	0.060	10%	0.00014	0.00124
7	0.060	20%	0.00028	0.00110
8	0.060	30%	0.00041	0.00097
9	0.120	0%	0	0.00276
10	0.120	10%	0.00028	0.00248
11	0.120	20%	0.00055	0.00221
12	0.120	30%	0.00083	0.00193

The operating maps for Cases 1, 2, 3, and 4 can be found in Figures 52, 58, 59, and 60, respectively. Comparing the plots between these four cases revealed that the operating region reduced with an increase in fuel flow through the back plate. Cases 2

and 3 saw an increase in the number of points where the diffuser could not obtain the proper pressure differential. Some test points were only achieved after fully opening the diffuser, which changed the acoustic mode of the UCC, and then closing it to the desired position. This possibly indicates there was an unstable region between the combusting and diffuser limit regions which depends heavily on the combustion dynamics. The addition of fuel through the back plate enabled continuous combustion at the 75% air through the core and 60% through the front plate test point whereas this test point resulted in a flameout when there was no fuel through the back plate. This suggests that injecting fuel through the back plate shifted the flameout region down and left. However, the operating region significantly decreased as a result of additional diffuser limit point which existed near the flameout region. Reviewing the average exit temperatures showed an increase in all points from Case 1 to 2 in the range of 65 K to 98 K. The temperature differences between Cases 2 and 3 and 4, were minor within 28 K.

Increasing the percentage of the fuel entering the CC through the back plate to 30%, shown in Figure 60, increased the operating region from that of Cases 2 and 3, making it comparable to the operating region of Case 1. The average exit temperatures for the test points were seen to increase between 58K and 118 K from the Case 1 values, however the temperature difference compared to Case 3 is not as great being between a decrease of 27 K and an increase of 23 K. While Case 4 indicates a performance increase from Case 1, the fuel injected through the back plate increased reactions within the vane passage which increased the acoustic levels and most likely the Rayleigh losses of the UCC. To verify this, future testing recording the acoustic characteristics and pressure across the UCC is necessary.

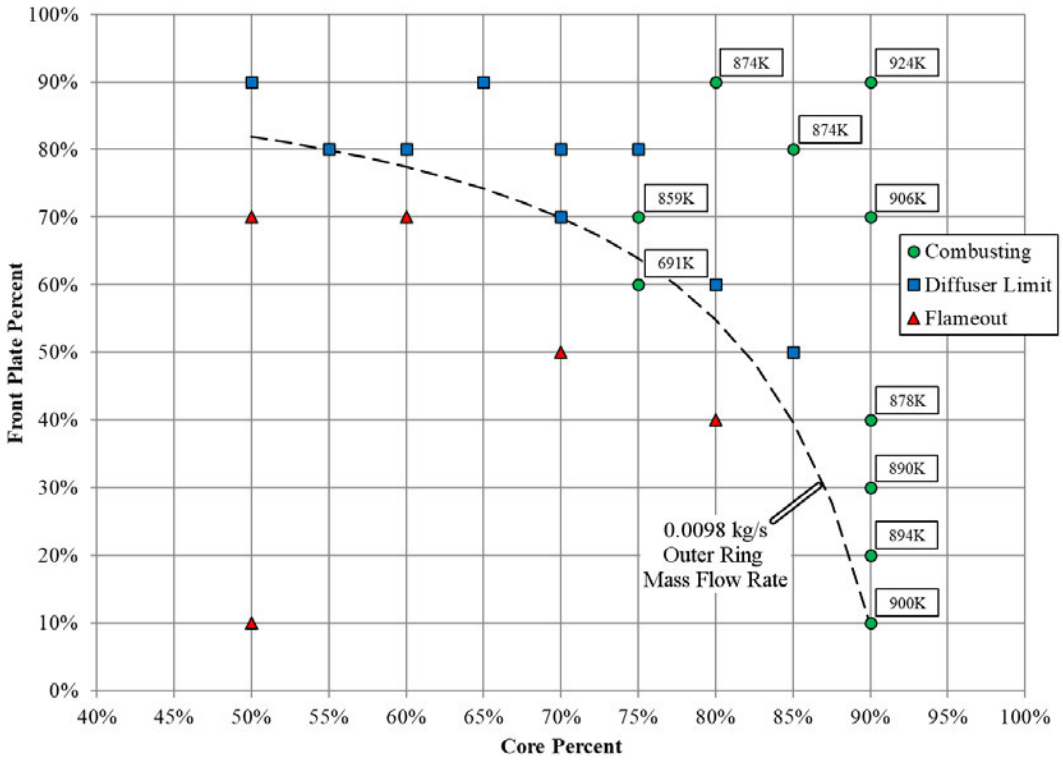

Figure 58. Case 2 Average Exit Temperatures 10% Back Plate Fuel, $\dot{m}_{in} = 0.108kg/s$

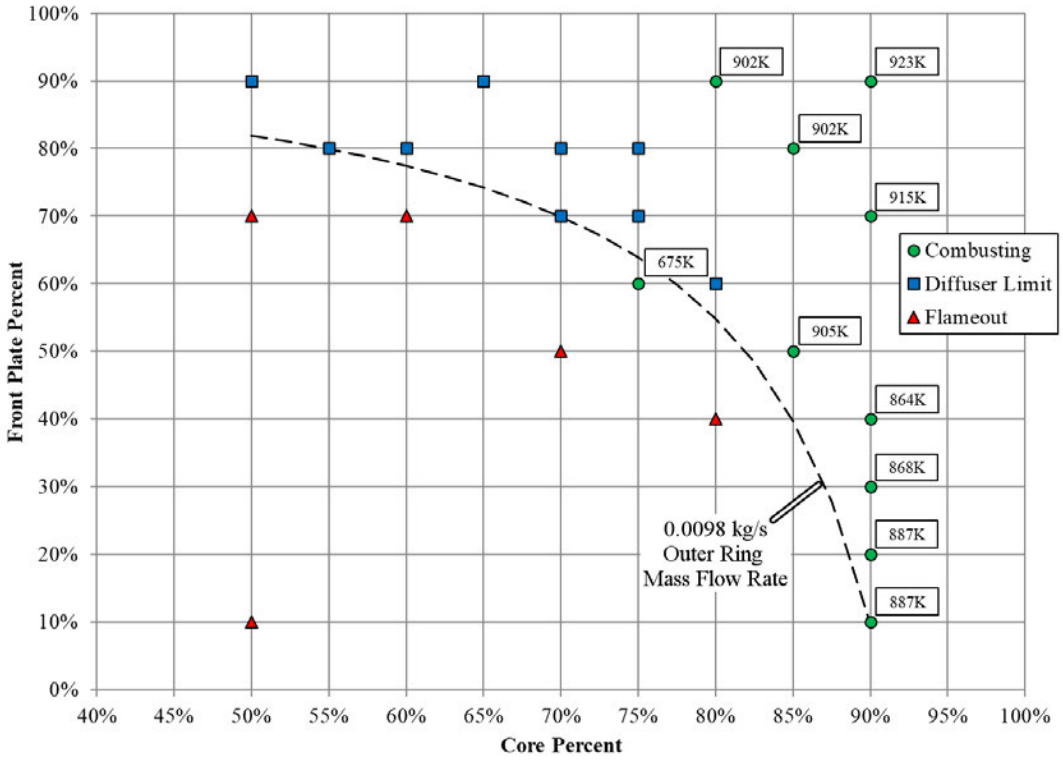

Figure 59. Case 3 Average Exit Temperatures 20% Back Plate Fuel, $\dot{m}_{in} = 0.108kg/s$

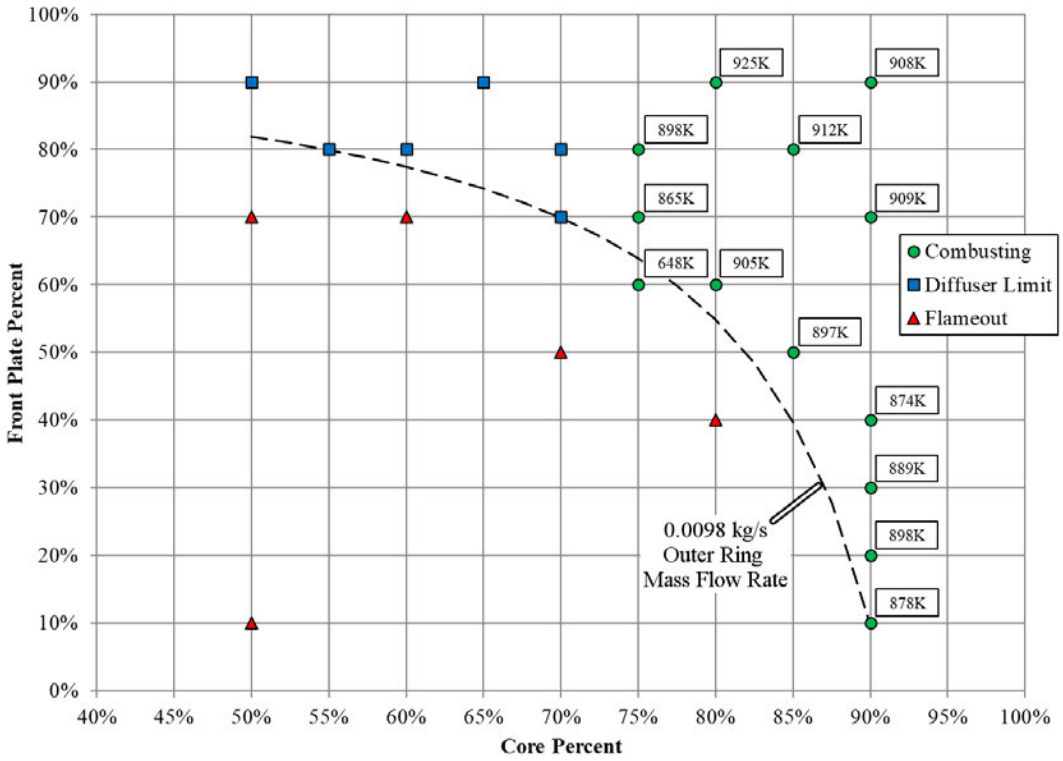

Figure 60. Case 4 Average Exit Temperatures 30% Back Plate Fuel, $\dot{m}_{in} = 0.108 kg/s$

The operating maps for Cases 5, 6, 7, and 8 can be found in Figures 55, 61, 62, and 63, respectively. Unlike the cases tested at a total air mass flow rate of 0.108 kg/s, the operating maps for the 0.060 kg/s cases did not show a reduction in operating range with a change in back plate fuel percent, but instead an increase. With the introduction of back plate fuel, four points which were unobtainable due to the limits of diffuser control became available, resulting in an increased operating region for the UCC. Besides the new availability of these four test points, the majority of exit temperatures between Cases 5 and 6 varied little, between a decrease of 8 K and an increase of 25 K. The 80% through the core and 90% through the front plate test point had a relatively large increase in temperature of 106 K. Increasing the back plate fuel to 20% resulted in an average increase in exit temperatures of 4 K. All the exit temperatures then decrease by up to 34 K

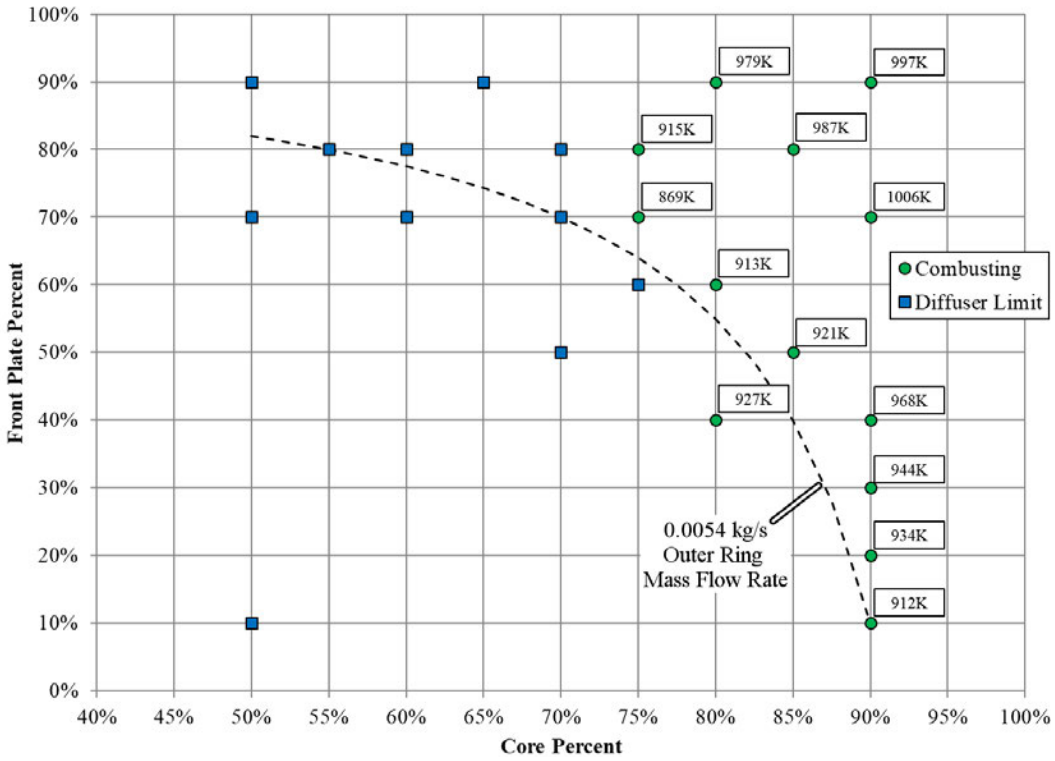

Figure 61. Case 6 Average Exit Temperatures 10% Back Plate Fuel, $\dot{m}_{in} = 0.060kg/s$

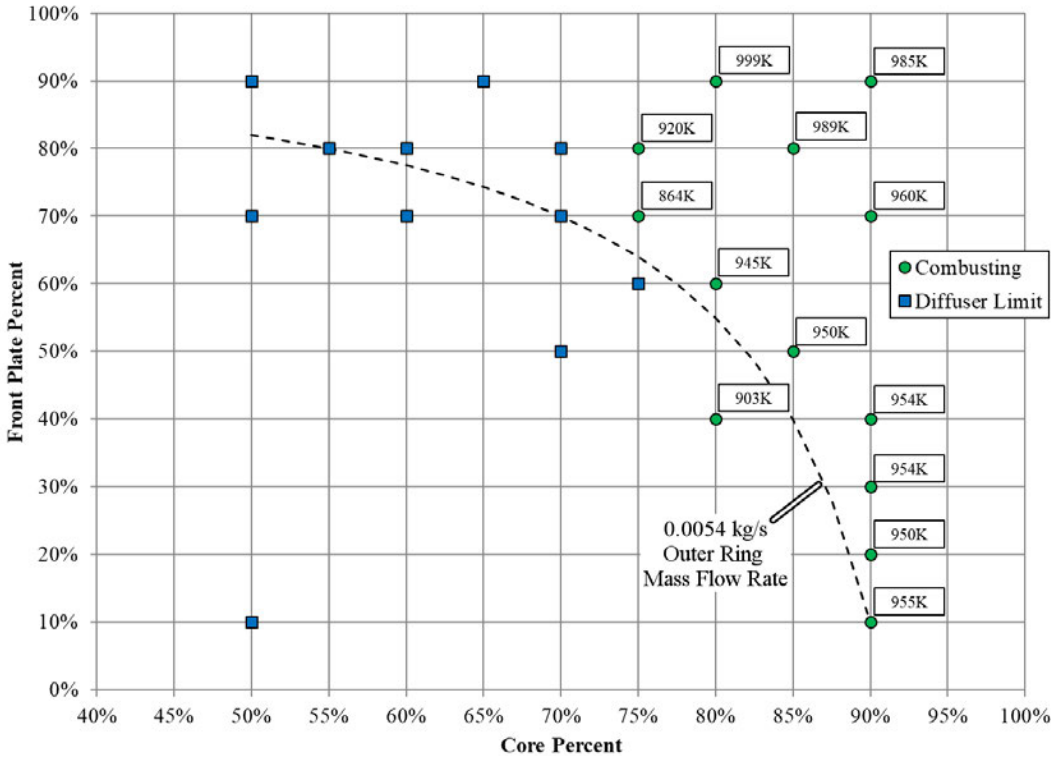

Figure 62. Case 7 Average Exit Temperatures 20% Back Plate Fuel, $\dot{m}_{in} = 0.060kg/s$

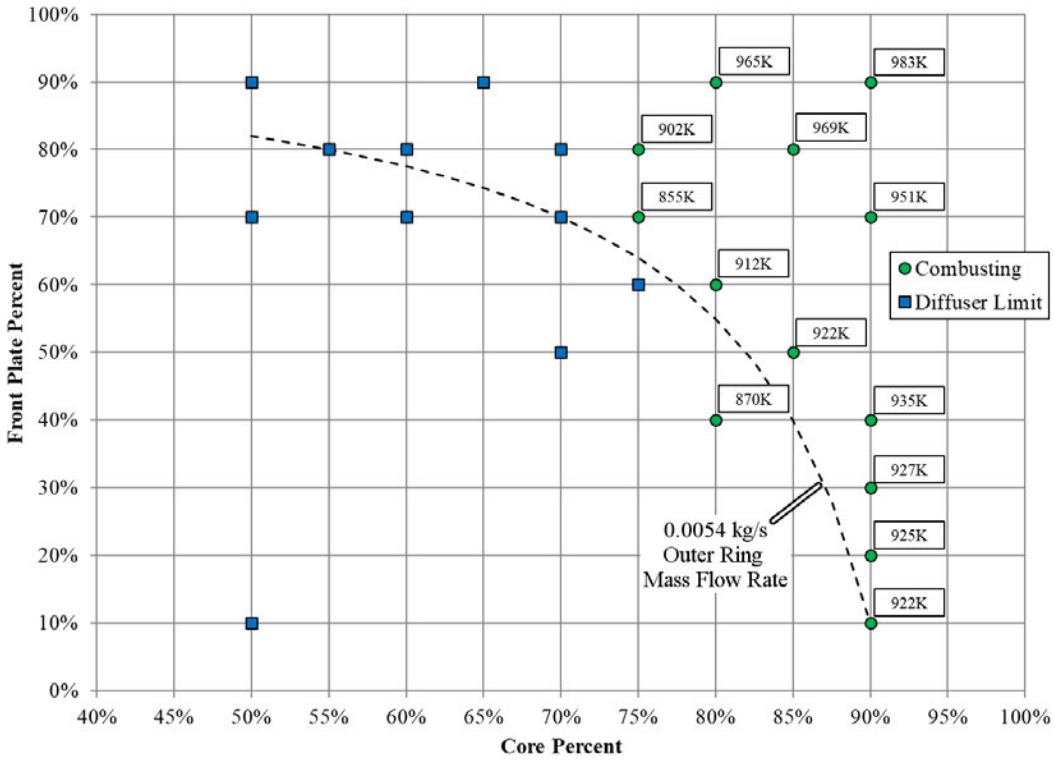

Figure 63. Case 8 Average Exit Temperatures 30% Back Plate Fuel, $\dot{m}_{in} = 0.060 kg/s$

from Case 7 to 8. Comparing Cases 5 and 8 show an average increase of 2 K in exit temperatures, with a peak increase of 91 K, however the operating range was increased by four test points. The increased operating range is beneficial as it allows the combustor to maintain combustion at additional engine flow conditions. Operating at 10% fuel through the back plate would minimize the increased reactions in the vane passages while obtaining the peak exit temperatures and increased operating range for a 0.60 kg/s total air mass flow rate.

The operating maps for Cases 9, 10, 11, and 12 can be found in Figures 56, 64, 65, and 66, respectively. At these higher mass flows, the introduction of 10% fuel through the back plate caused the 80% through the core and 60% through the front plate test point, which was possible to achieve in Case 9, unobtainable. Case 10 also had a large decrease in exit temperature of 277 K for the 90% through the core and 20%

through the front plate test point from Case 9. The other test points were between a 26 K decrease and 77 K increase. Increasing the fuel through the back plate to 20% opened the operating region back up to include the 80% through the core and 60% through the front plate test point while also allowing combustion at the 90% through the core and 10% through the front plate test point which was previously resulted in flameout. Case 11 also increased the exit temperature of the 90% through the core and 10% through the front plate test point by 287 K, close to the Case 9 value. All other test points were between an 80 K decrease and 48 K increase from Case 10. Increasing the fuel through the back plate to 30% had no change in the operating region, but a majority of the exit temperatures increased with an average increase of 31 K. Comparing Cases 9 and 12 show an addition of one operating point and an increase in exit temperatures up to 103 K. While the operating region remained relatively consistent across all cases, an acoustics shift in a similar manner as the 0.108 kg/s cases was observed.

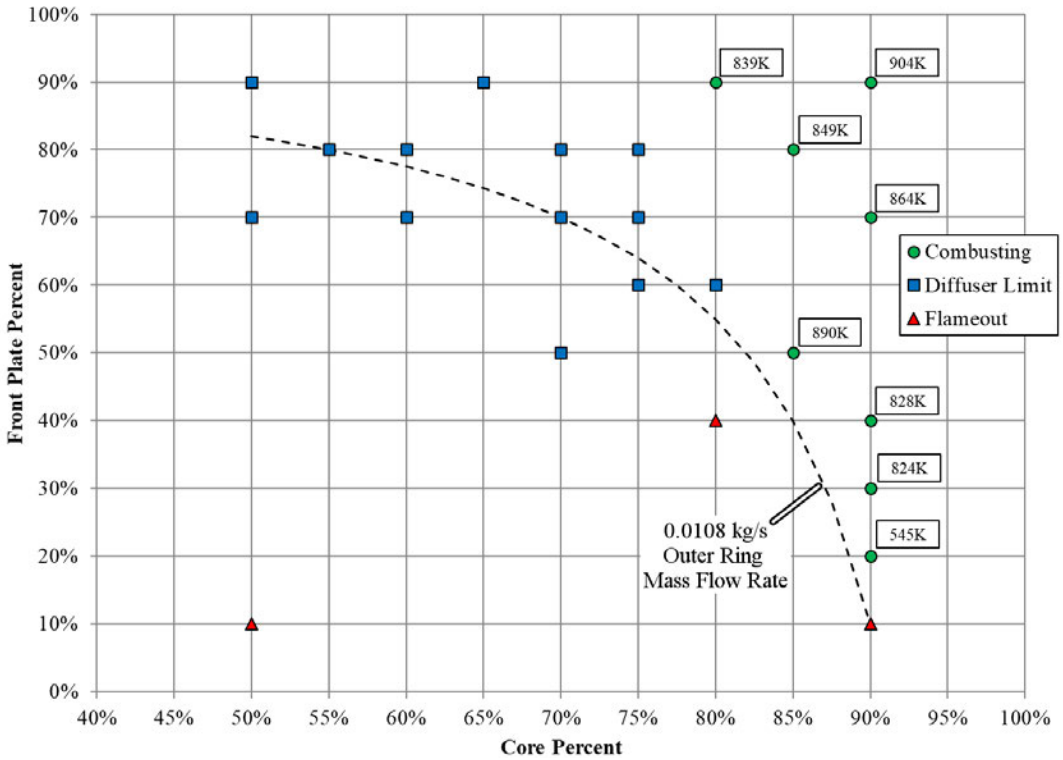

Figure 64. Case 10 Average Exit Temperatures 10% Back Plate Fuel, $\dot{m}_{in} = 0.120 kg/s$

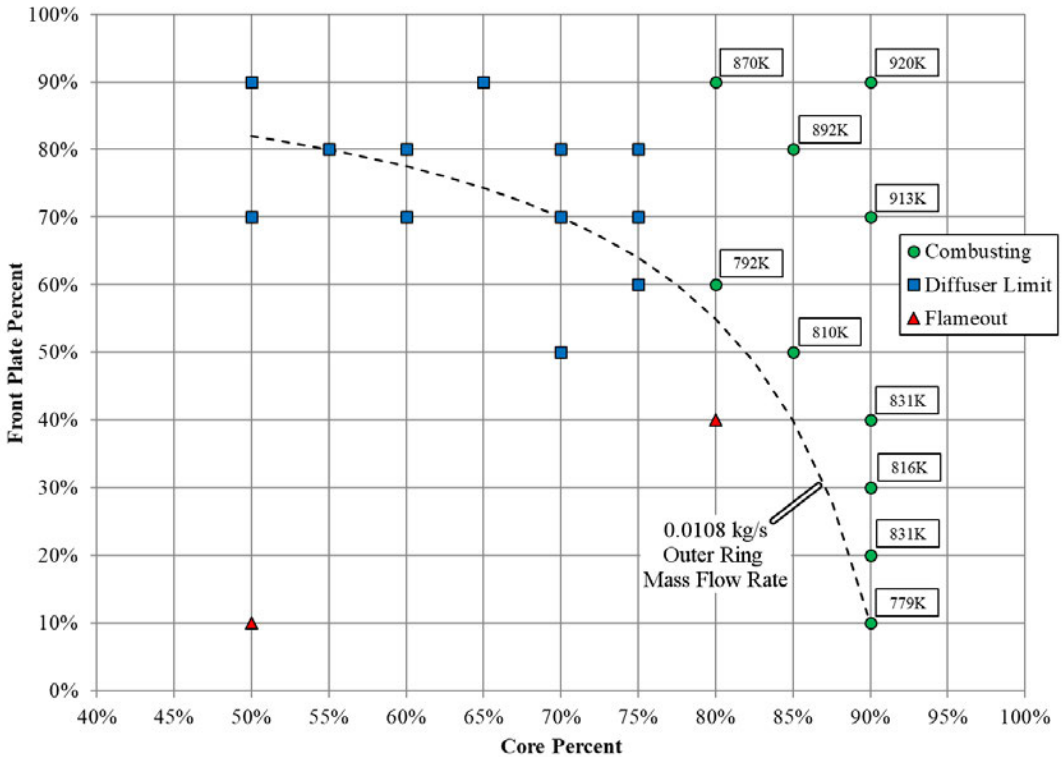

Figure 65. Case 11 Average Exit Temperatures 20% Back Plate Fuel, $\dot{m}_{in} = 0.120kg/s$

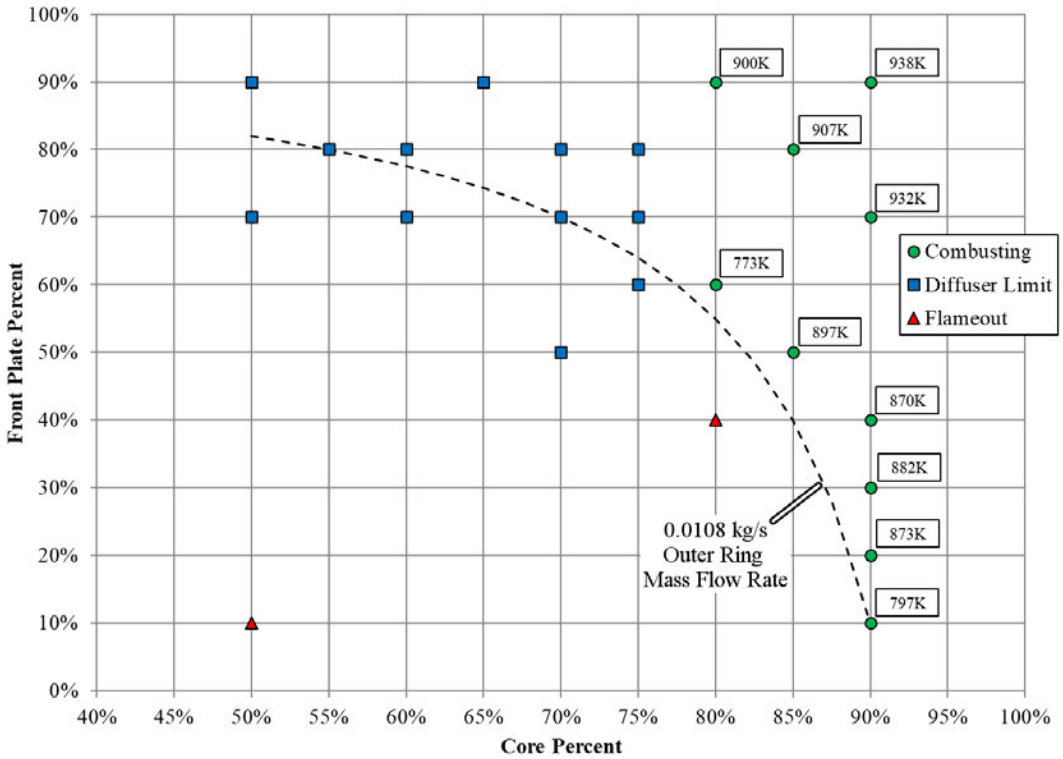

Figure 66. Case 12 Average Exit Temperatures 30% Back Plate Fuel, $\dot{m}_{in} = 0.120kg/s$

The operating maps for each total air mass flow rate was imported into MATLAB where intermediate points were interpolated and a 3-dimensional operating map was constructed, as shown in Figures 67, 68, and 69. The points which were labeled as flameout or diffuser limit regions were given a value of 0, while all other points were given their average exit temperature values. From this data a mesh grid was generated with 0.3% intervals in airflow and bounded between 50% and 90% for the percent through the core, 10% and 90% for the percent through the front plat. Planes were created for 0%, 10%, 20% and 30% total fuel through the back plate. These plots provide better visualization and qualitative comparison of the test matrix.

Figure 67 shows the vast decrease in operating range from 0% back plate fuel flow to 10% and 20% back plate fuel flow. However, the operating range opens back up with 30% of the fuel injected through the back plate at exit temperatures greater than with no fuel flow through the back plate. Figure 68 shows an operating range increase with back plate injection. The exit temperatures are seen to peak with 10% of the fuel injected through the back plate and then slowly decrease with increasing back plate fuel flow. Unlike the other cases, Figure 69 shows very little change in the operating range with back plate fuel injection, however this operating range is no larger and results in lower exit temperatures than the other cases. The exit temperatures are seen to increase with increasing back plate fuel flow, however this increase does not offset the drawback of the decreased operating range.

Overall, back plate injection was beneficial in increasing exit temperature, but its effects on operating range varied with total air mass flow rate. As the total air mass flow rate increased, the reduction in the operating range due to back plate injection also increased. Comparing the flow conditions, the best condition for UCC operation was at a total air mass flow rate of 0.060 kg/s with 10% of the fuel flow through the back plate. At this condition, the operating range is widest, at 13 points, and exit temperatures greatest, peaking at 1006 K, for a global equivalence ratio of 0.36.

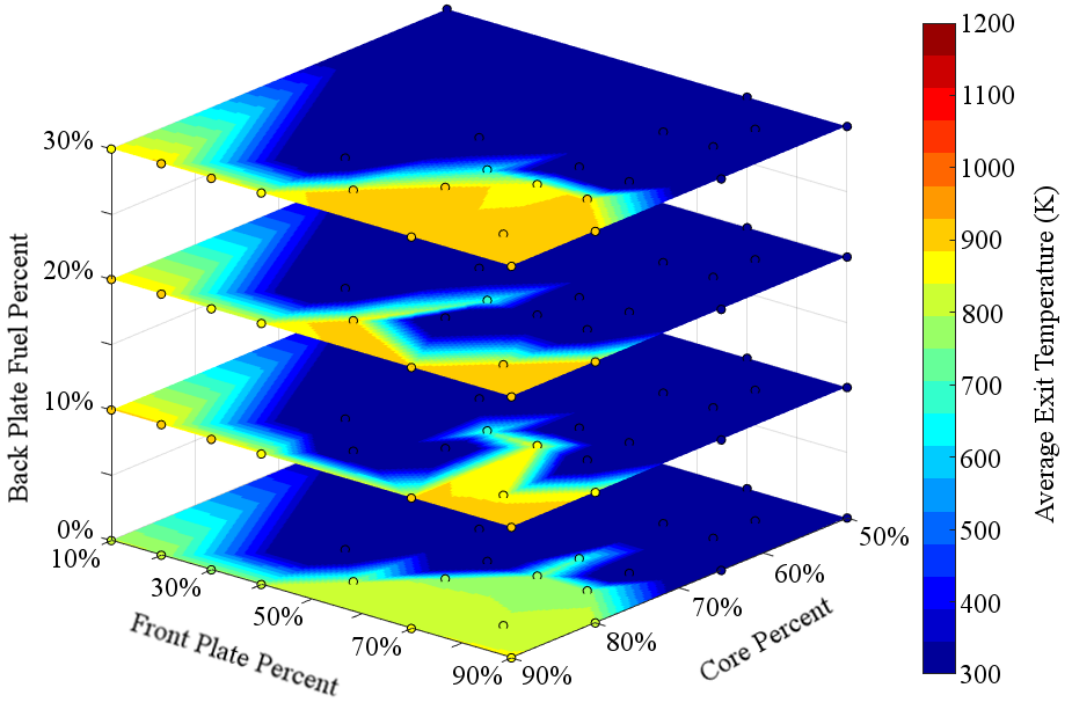

Figure 67. Average Exit Temperature Full Back Plate Operating Map, $\dot{m}_{in} = 0.108kg/s$

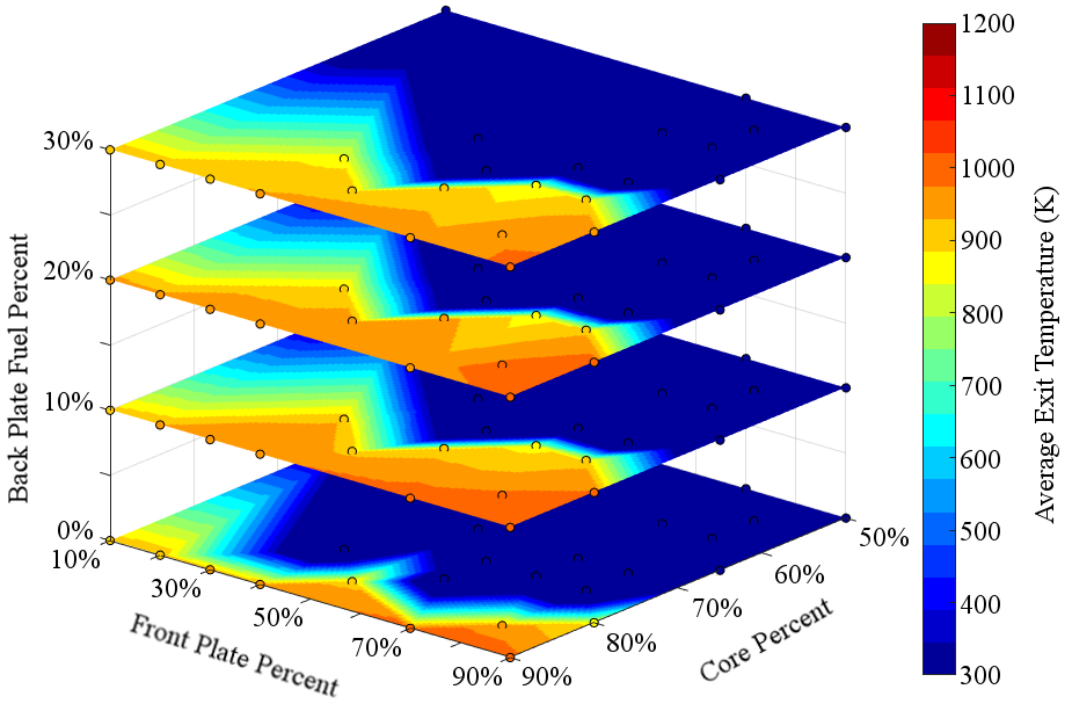

Figure 68. Average Exit Temperature Full Back Plate Operating Map, $\dot{m}_{in} = 0.060kg/s$

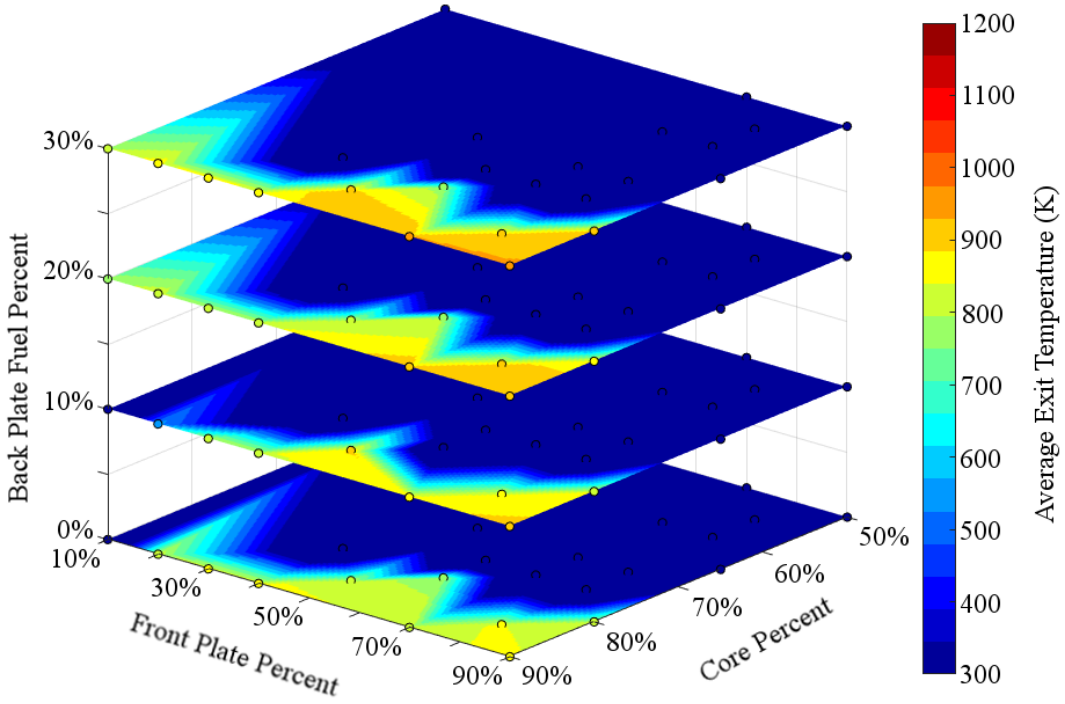

Figure 69. Average Exit Temperature Full Back Plate Operating Map, $\dot{m}_{in} = 0.120kg/s$

The results of this chapter completed the first two objectives of this research. First, the computational analysis of the 12-Step Ring showed that the centrifugal loading in the CC was increased by 262%. Then experimental testing of the design showed increased flame stability and a wider range of operational cavity equivalence ratios, completing the first objective of this research. Furthermore, the new control over the UCC air and fuel flow brought be the redesigned components was characterized to develop operating maps of the combustor which established operating points producing peak exit temperatures. These maps showed control over the UCC performance was possible, completing the second objective of this research.

V. UCC Film Cooling

The UCC geometry not only offers potential size and combustion benefits, but it also allows the development of a unique cooling scheme. The location of the HGV with respect to the CC keeps the leading edge of the vanes ahead of the combustion products, as shown in Figure 70. The HGV sits radially inward of the CC and extends both upstream and downstream which results in the HGV experiencing a wide temperature range as the leading edge is only exposed to incoming compressor exit core flow while the hot combustion products enter midway down the vane, impinging on the suction surfaces of the vanes. Bohan et al. [31] theorized a design which utilized the upstream positioning of the HGV leading edge. Instead of air being bled from the compressor and ducted around the combustor like in traditional engines, this cooling scheme intakes core air through the stagnation region at the leading edge of the HGV. The coolant air was then ducted internally around a plug to build up pressure and then exited throughfilm cooling holes or a trailing edge slot.

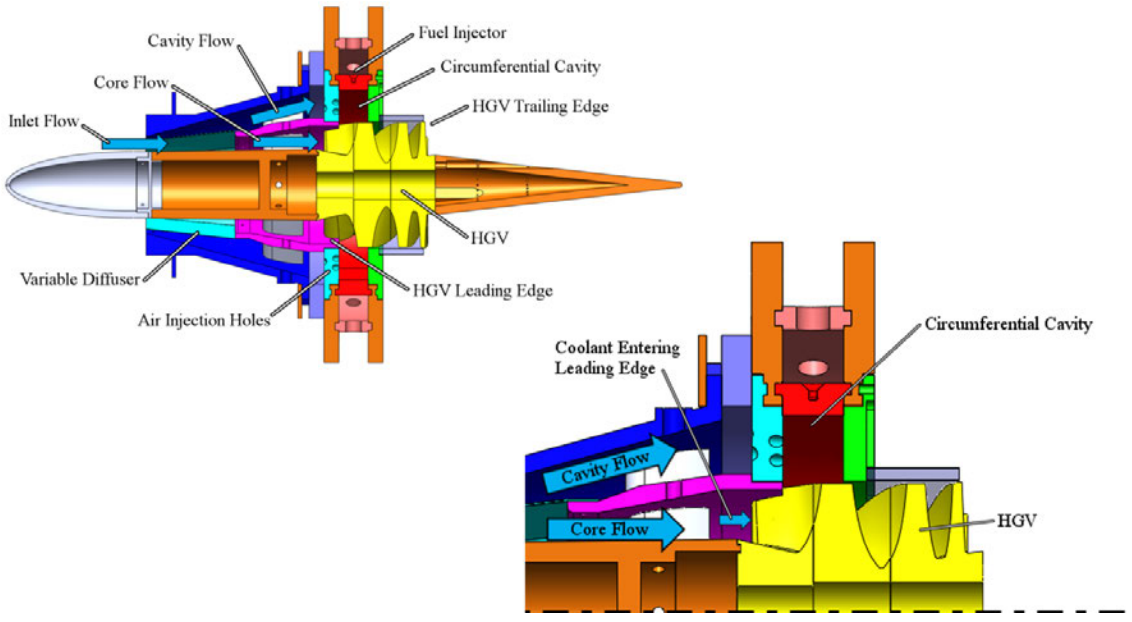

Figure 70. Cross-Section of UCC Showing HGV Location

Bohan et al. [31] conducted a CFD analysis of various cooling schemes using this setup. Within the study, the plug distance and exit size were varied to determine which configuration resulted in the greatest pressure differential between the inner and outer surfaces of the vanes at the earliest axial chord location. The results showed that the highest internal pressure was established using a 5.84 mm plug distance and a 0.477 cm^2 exit area. The pressures on the internal and external surfaces varied with axial chord, and this distribution is shown in Figure 71. In order for the internal flow to exit, the holes must be located in a region where the internal pressure is greater than the external pressure. Bohan et al. [13] determined that this region existed past 50% axial chord.

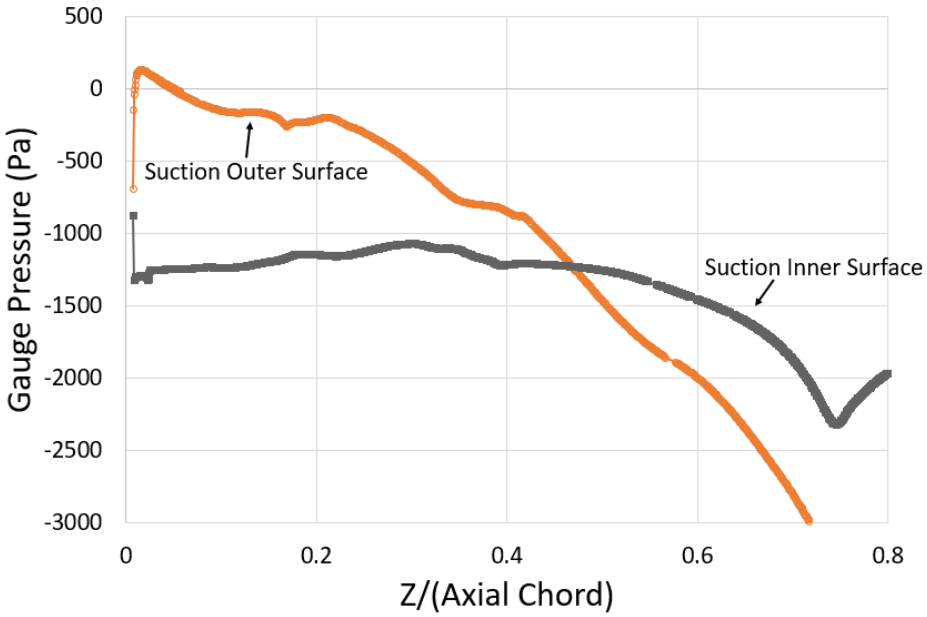

Figure 71. Vane Surface Pressure Distributions [31]

5.1 Design and Manufacturing

Based on the results reported by Bohan et al. [31], five different cooling schemes were designed and incorporated into five of the six HGV vanes. The cooling schemes were based off the basic structure displayed in Figure 72. The leading edge of each

vane had a 2.06 cm span, a 2.54 cm axial chord length, and contained a rectangular inlet with a 0.839 cm^2 area, and the vane surface thickness was held constant at 1.27 cm. For each vane, the plug distance, film cooling holes incorporation, and exit size were varied as listed in Table 10, with the sixth vane being a solid, uncooled vane.

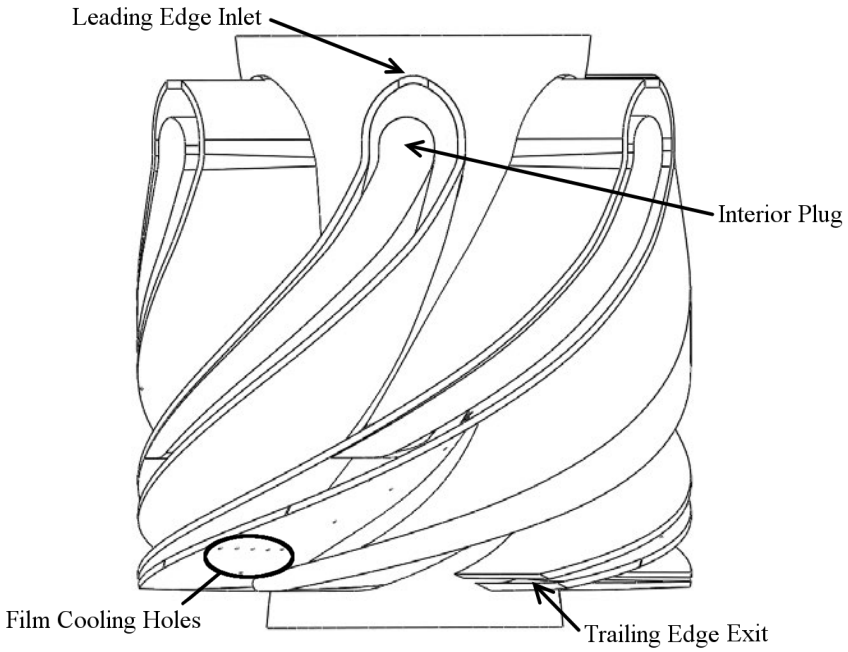

Figure 72. Internal Vane Structure

Table 10. HGV Cooling Schemes by Vane

Vane	Plug Distance (mm)	Cooling Holes	Exit Area (cm^2)
A	5.84	Yes	0.477
B	2.29	No	0.587
C	5.84	Yes	None
D	5.84	No	0.587
E	5.84	Yes	0.587

The cooling holes incorporated in the three vanes were non-shaped circular holes 0.508 mm in diameter and at a 30° angle from surface normal. The holes were incorporated in six different axial locations past the 50% axial chord distance established

by Bohan et al. [31] as shown in Figure 73. The first location only had one hole located 87% radial span. The second, third, fourth, and sixth locations had two holes located at 87% and 60% radial span. The fifth hole location had six holes located at 87%, 82%, 76%, 70%, 64%, and 60% radial span. This scheme allowed evaluation over a wide variety of axial and spanwise locations to see the effects on coolant distribution.

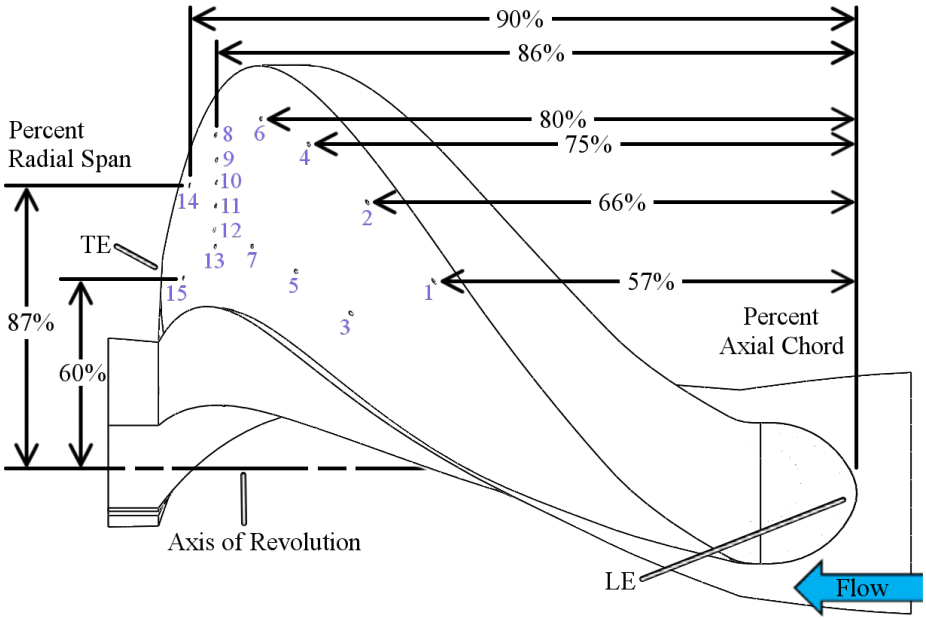

Figure 73. Cooling Hole Locations

These cooling designs were intended to be additively manufactured into the HGV. To accomplish this, an internal support structure was required to avoid part deformation due to large unsupported overhangs. The design goal of the internal supports was to support the vane surfaces during printing while minimizing the internal blockage. The first design implemented a 1 mm thick lattice structure shown in Figure 74 (a). Printing errors occurred with the printer's recoater blade contacting the part's external support structure and the internal lattice structure, resulting in the part shown in Figure 74 (b). To aid in the integrity of the external support structure,

the part was reprinted with a 3.5 mm thick ring around the part. This solved the external support structure problem, however the internal structure was still damaged. To visualize the extent of the damage, a test print of the back half of a single vane was printed. The test print design and final product can be seen in Figures 74 (c) and 74 (d) respectively. The test print confirmed that the internal lattice structure had been broken away due to the recoater bladed and the resulting top vane surface had geometry deformations from the lack of support.

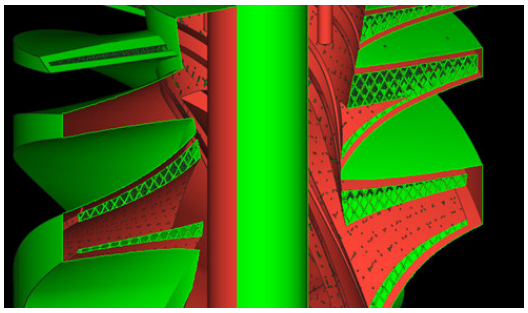

(a) Internal Lattice Structure

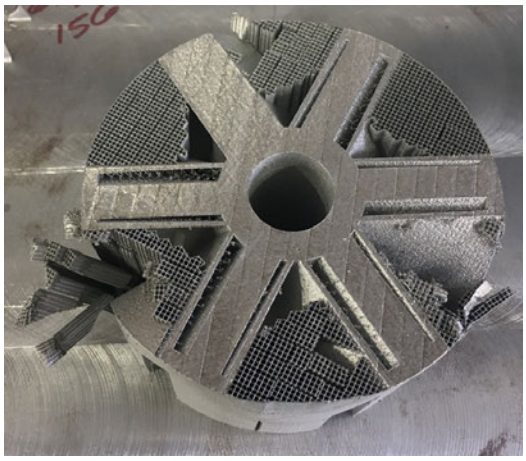

(b) First Print Result

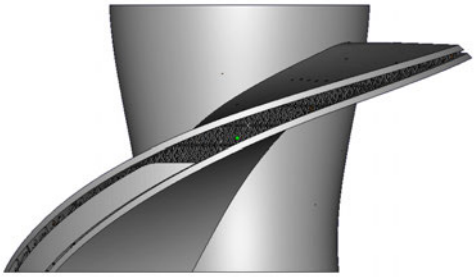

(c) Partial Test Print Design

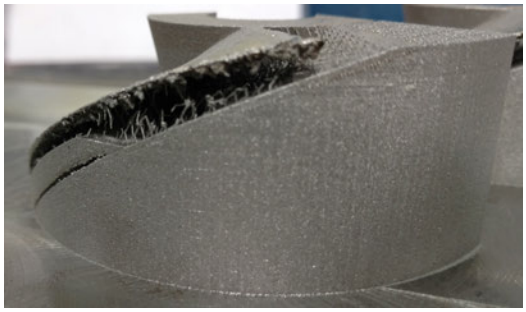

(d) Partial Test Print Result

Figure 74. First HGV Internal Support Design

Two alternative designs were engineered and suggested by Linear AMS. The first suggested design consisted of 2 mm thick rectangular supports spaced 3 mm radially apart, as shown in Figures 75 (a) and 75 (b). The back half of a single vane was

modeled using this internal structure, shown in Figure 75 (c), and a test print was conducted to determine the integrity of internal structure and the result is shown in Figure 75 (d). This internal design resulted in no broken support structures and a well supported top surface. However, the supports added a large volume into the internal surface resulting in a significant amount of flow blockage.

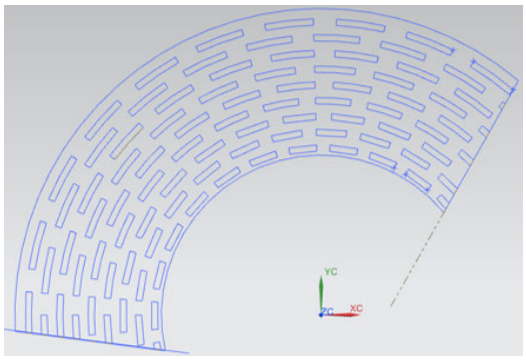

(a) Internal Structure Top View

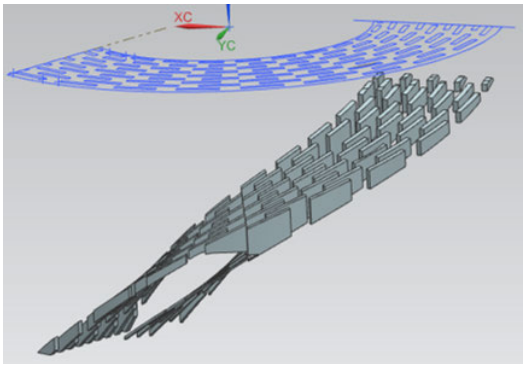

(b)Internal Structure

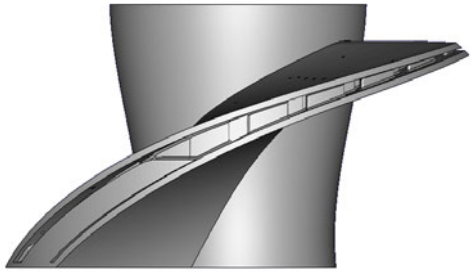

(c) Partial Test Print Design

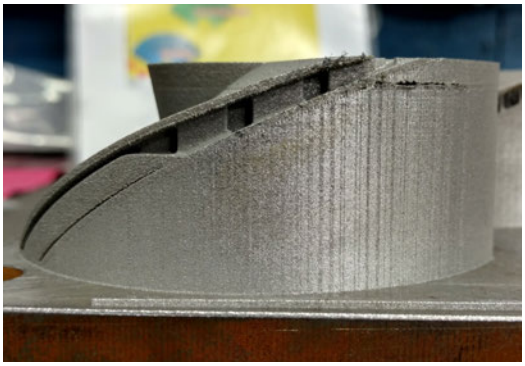

(d) Partial Test Print Result

Figure 75. Rectangular Internal Support Design

The second suggested design consisted of 2 mm diameter circular supports spaced 3 mm apart, as shown in Figures 76 (a) and 76 (b). The back half of a single vane was modeled using this internal structure, shown in Figure 76 (c), and a test print was conducted to determine the integrity of the internal structure, the result of which is shown in Figure 76 (d). Although this internal design resulted in two broken support pins, the top surface was well supported and there was no deformation. The use

of these circular supports greatly opened the interior of the vane compared to the rectangular supports, and thus this design was selected and implemented into the HGV design.

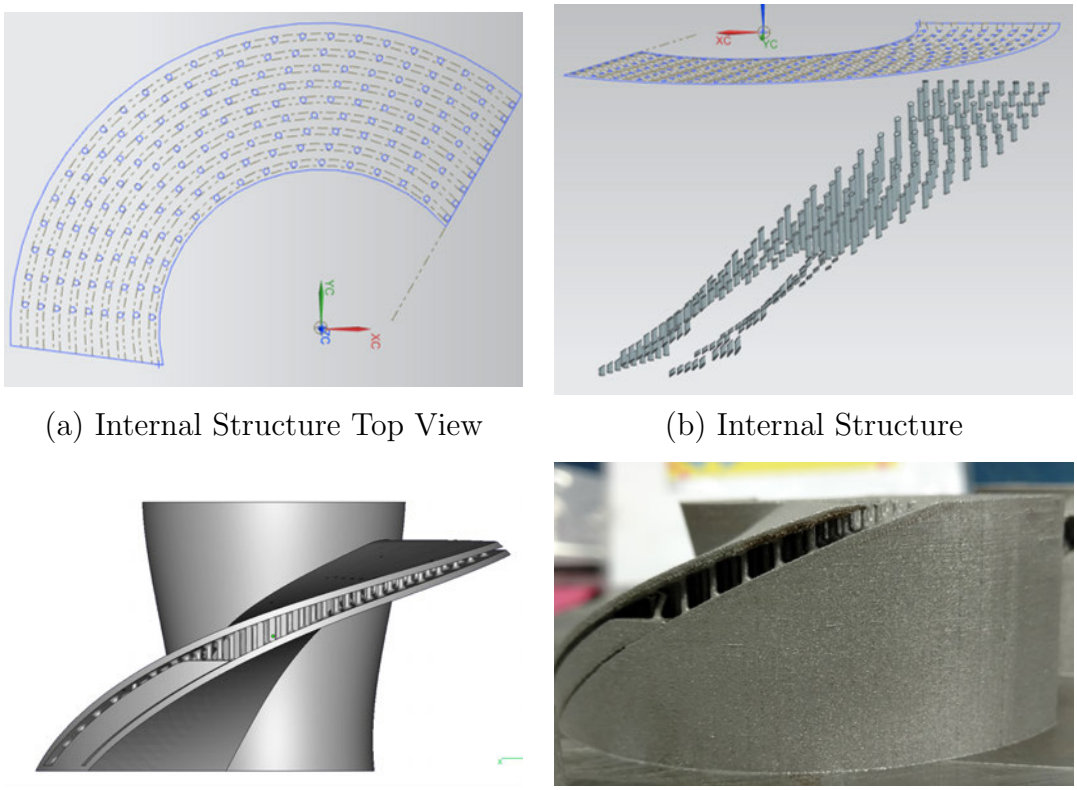

(a) Internal Structure Top View

(b) Internal Structure

(c) Partial Test Print Design

(d) Partial Test Print Result

Figure 76. Circular Internal Support Design

Even with the internal support structure printing the HGV was still difficult. Linear AMS attempted to print the HGV axially from the trailing edge to the leading edge. An anchor was printed onto the build plate to decrease the distance between the vane surface and a solid contact. Support material was built on top of the anchor connecting to the vane surface. However, the asymmetric design of the HGV caused the solid vane to lift off the support material and strike the recoater blade, as shown in Figure 77. Printing parameters needed to be evaluated in order to print the part as supports had to extend up to 22 mm without separating from surfaces. Linear AMS

conducted different tests to evaluate multiple printing parameters. First, the support parameters were evaluated by printing nine blocks across the build plate with various laser powers and speeds. The growth height and adhesion of each block was reviewed and an energy density was selected. Then, five prints of the front 3.81 cm of the vane, to include the vane under it, were printed using this energy density. Here, support separation and recoater blade impacts were reviewed to determine a support density. Finally, the full vane was attempted and completed.

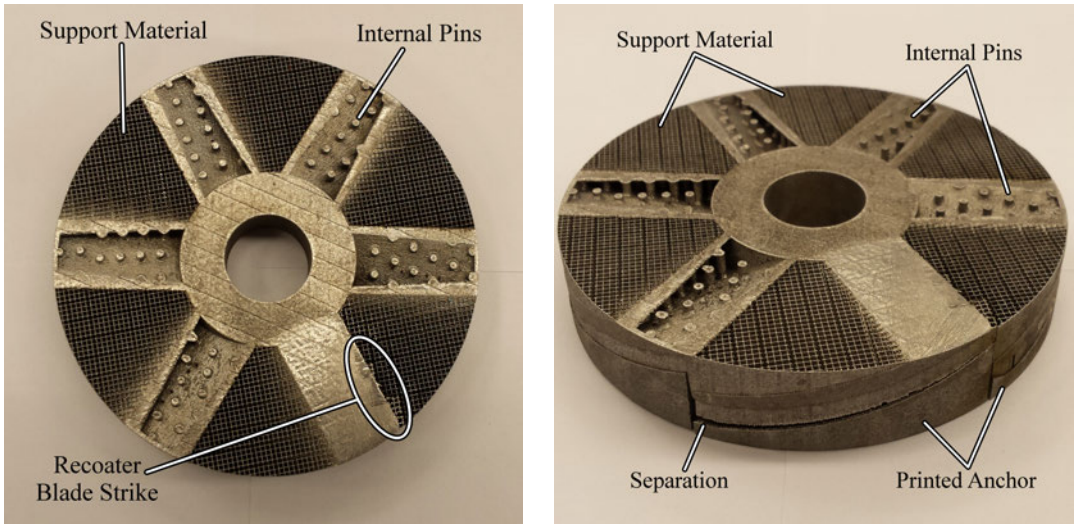

(a) Top View (b) Side View

Figure 77. HGV Printing Problem

In the final design, the supports, shown in Figure 78 (a), started 25.4 mm from the leading edge and extended to the trailing edge. The final vane design took 72 hours to be additively manufactured by Linear AMS in 17-4 stainless steel. There were three build stops during the build process and one recoater jam, which occurred 6.35 cm from the base of the vane, the peak height of the supports. The part was cut off the build plate and delivered to AFIT where it was brought to the AFIT Machine Shop for post-processing, resulting in the part shown in Figures 78 (b), (c), and (d).

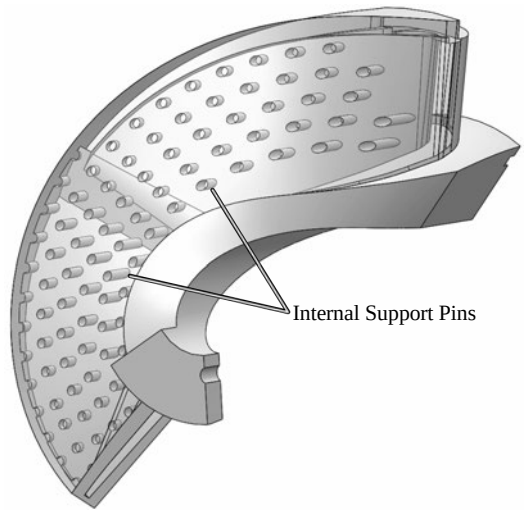

(a) Internal Structure

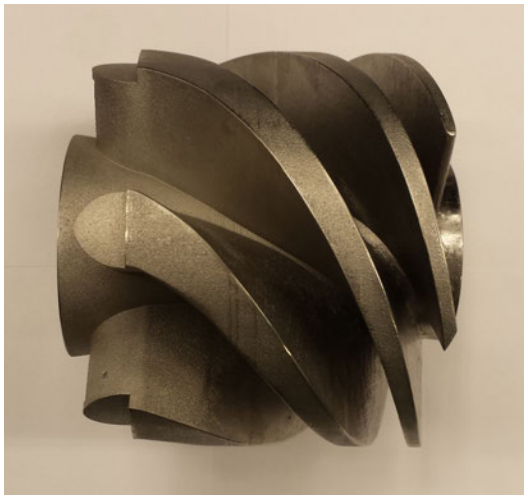

(b) Leading Edge

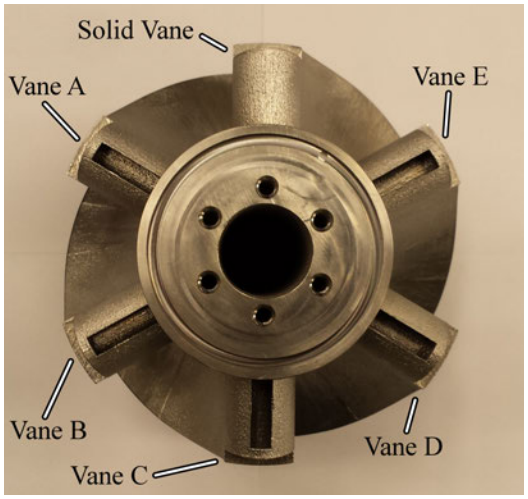

(c) Side

(d) Trailing Edge

Figure 78. Additively Manufactured HGV With Cooling Schemes

5.2 Film Cooling Design CFD Evaluation

Although the internal passage was kept as open as possible, it was expected that the addition of the pins to the design would result in a lower internal pressure distribution than calculated for the open internal passage shown in Figure 71. The pins were also expected to impact the effectiveness of the cooling scheme. To determine the effects of the pins, numerical analysis was conducted on a model of the Vane

A geometry in Table 10 to determine the effects of the support structure on the HGV. Four cases were conducted and are described in Table 11. Cases 1 and 2 were conducted by Bohan et al. [31], while Cases 3 and 4 are defined in this study.

Table 11. HGV CFD Cases

Case	Plug Distance (mm)	Cooling Holes	Exit Area (cm^2)	Internal Structure
1		Solid Vane		
2	5.84	No	0.477	No
3	5.84	Yes	0.477	No
4	5.84	Yes	0.477	Yes

5.2.1 CFD Setup and Settings.

The three dimensional domains, shown in Figure 79, consisted of a fluid volume, which included reacting chemistry, and a solid volume, allowing conjugate heat transfer. Heat transfer between the vane surface and the fluid was allowed and only considered at the interface between the vane surface and the fluid, all other walls were considered adiabatic. Within the fluid and solid volumes, away from the interfaces,

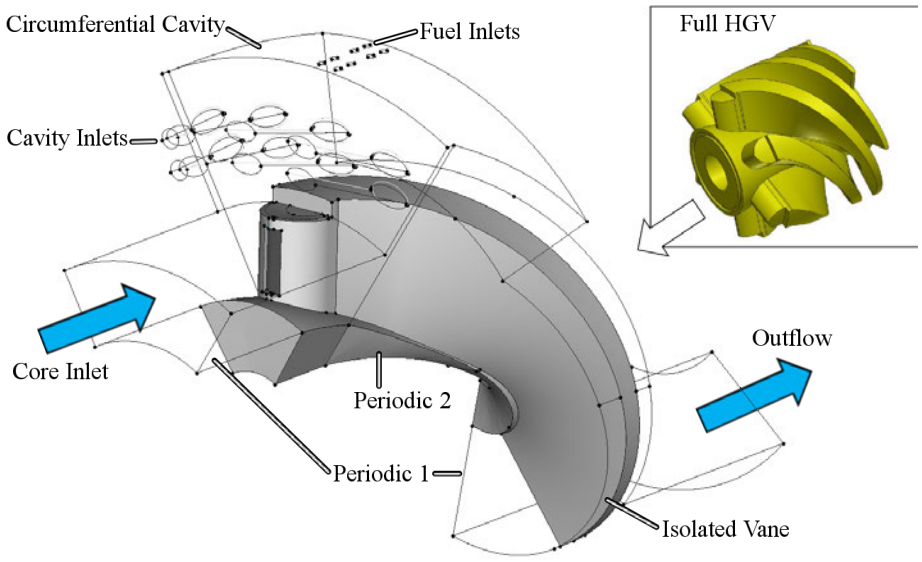

Figure 79. HGV CFD Test Domain

the advection and conduction respectively were calculated independently. Although the AFIT UCC was supplied from a common air source, as shown in Figure 19, the computational domain had independent inlets for the core and cavity flows for simplification and direct control over cavity airflow. The core inlet had an inner radius of 3.05 cm and a 1.98 cm channel height. The cavity inlets were circular with a 0.45 cm diameter and angled 55° relative to the engine centerline. The HGV was modeled to be rotationally periodic over 60°. This created a single vane wherein a slice of the circumferential cavity, an entrance passage, and an exit passage were modeled in order to establish an accurate flow field around the vane.

The cases were generated in Pointwise version 17.3, release 5, and the final grid is shown in Figure 80. The solid region was modeled by a fully unstructured mesh while a T-Rex hybrid mesh modeled the fluid volume. The T-Rex function builds three dimensional anisotropic tetrahedrals off selected surfaces which creates prisims within the boundary layer. This allows the boundary layer to be well defined and appropriately modeled. Once interference from the vane's geometry or adjacent cells prohibited the structured prisims from being generated, the remaining fluid volume

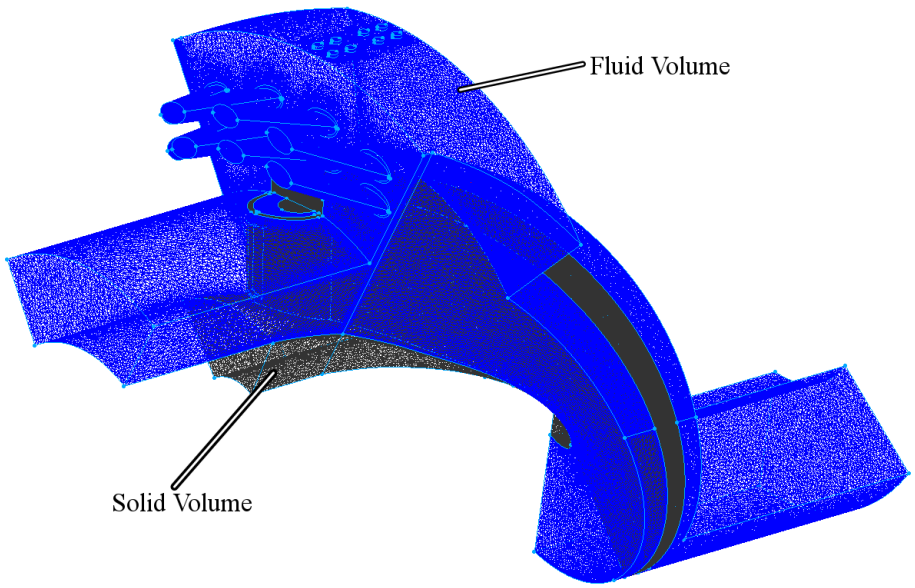

Figure 80. HGV CFD Grid

was filled with unstructured cells. The resulting grids had a resolution of 68 million cells for Case 3, without the internal support pins, and 80 million cells for Case 4, with the internal support pins. These grids were generated using the template established and tested for grid independence by Bohan et al. [31].

The cases were solved for a CFD solution using FLUENT release 16.2 with a pressure-based solver and an absolute velocity formulation. The following settings were selected for consistency with the work done by Bohan et al. [31], a review of the works of Briones et al. [34] and Cottle [5, 35] who both obtained solutions comparable to UCC experimental data, and a review of the FLUENT manual [36].

To model heat transfer between the fluid and solid, the coupled fluid-solid energy equation was turned on. The flow was expected to be turbulent thus a k-ω Shear Stress Transport (SST) model with viscous heating was selected. The k-ω SST model was chosen over other turbulence models because of its performance in wall bounded flows and heat transfer problems [30]. The grid was well defined within a majority of the boundary layer resulting in a y^+ value of one or better allowing accurate modeling of heat transfer and wall properties.

Gaseous propane and air were injected into the circumferential cavity through the fuel inlets and cavity inlets shown and labeled in Figure 79, respectively. The cavity modeled was the one designed by Cottle [5] and discussed in Section 3.2. To model combustion within the cavity and completing chemical reactions within the vane passages a Partially Premixed Model using the FGM with non-adiabatic, diffusion flamelets and GRI 3.0 chemical equilibrium reaction mechanism was used with the reaction progress variable set to finite rate. The FGM model parameterizes the combustion species and temperatures by a few variables such as mixture fraction, scalar dissipation, and reaction progress. The transport equations are then solved for these parameters in the 3D simulation. The FGM model thus allows the flame to be fully quenched from wall contact or dilution air. To model combustion accurately

the GRI 3.0 chemical equilibrium tables were imported into FLUENT. These tables were then used by FLUENT to create mixture fractions of products from combustion at different flame temperatures. From these products a mixture PDF was generated and this defined species within the fluid volume.

The inlets were set as mass flow inlets with values shown in Table 12 resulting in a cavity equivalence ratio of 0.72. The core and cavity inlets were set to flow air while the fuel inlets were set to flow propane. All gases were injected at 300 K with a 5% turbulence intensity and the set core inlet conditions corresponded to a Reynolds number of $5{\cdot}10^4$. As the HGV was made of 17-4 stainless steel, the solid components were modeled as stainless steel which was imported from the FLUENT material database.

Table 12. HGV CFD Inlet Boundary Conditions

Boundary	Mass Flow (kg/s)	Gauge Total Pressure (Pa)
Cavity Air Inlet	0.0054	4800
Core Inlet	0.0126	4800
Fuel Inlet	0.00025	5200

The coupled pressure-velocity scheme was used to solve pressure and velocity simultaneously for both cases. For Case 3, without internal pins, second order upwind was selected for all spatial discretization parameters. Solution stability was quickly achieved with combustion modeled. The pins in Case 4 made solution stabilization difficult with second order schemes, thus standard initialization was used along with first order schemes to achieve stability. Once stabilized, the fluid ignited and the solution converged with reactions occurring. The cases were both solved as steady-state with the pseudo transient option enabled to accelerate convergence. Solution convergence was then evaluated through equation residuals and an area weighted average of the exit plane surface temperature.

5.2.2 CFD Results.

The CFD evaluation aimed to cover three major goals with respect to controlling cooling for a UCC HGV. These include: results outlining where coolant can be ejected, the impact of different cooling schemes on the resulting surface temperature, and the effects from the required internal support pins. The initial theory laid out by Bohan et al. [31] was confirmed by evaluating the cooling hole mass flow rate at specific axial locations. The surface temperature effects were conducted by comparing the overall effectiveness profiles of a solid vane, a hollow vane without cooling holes, the hollow vane with cooling holes, and the vane with cooling holes and support structure referred to as Cases 1, 2, 3, and 4, respectively. Finally the effects stemming from the requirement to add an internal pin support structure for manufacturing were studied by comparing overall effectiveness, surface pressure distribution, and coolant mass flow between Cases 3 and 4.

The pressure distribution on the suction side of the vane both internally and externally established the driving force of coolant flow through the holes. The pressure distributions for Cases 2, 3, and 4 are shown in Figure 81. The Case 2 distribution was reported by Bohan et al. [31] and compared to Cases 3 and 4 which is shown in Figure 81. Even with the incorporation of cooling holes the pressure distributions between Cases 2 and 3 follow the same trend.

The incorporation of the pins in Case 4 resulted in a lower pressure drop near the inlet of the vane as shown in Figure 81. This caused the point at which the internal surface pressure surpasses the external surface pressure, the transition point, to be at 35% axial chord instead of at 50% or 45% as seen in Cases 2 and 3, respectively. After the transition point, the internal pressure remains above the external pressure, however this pressure differential is lower than that for Cases 2 and 3, resulting in a lower mass flow rate through the vane.

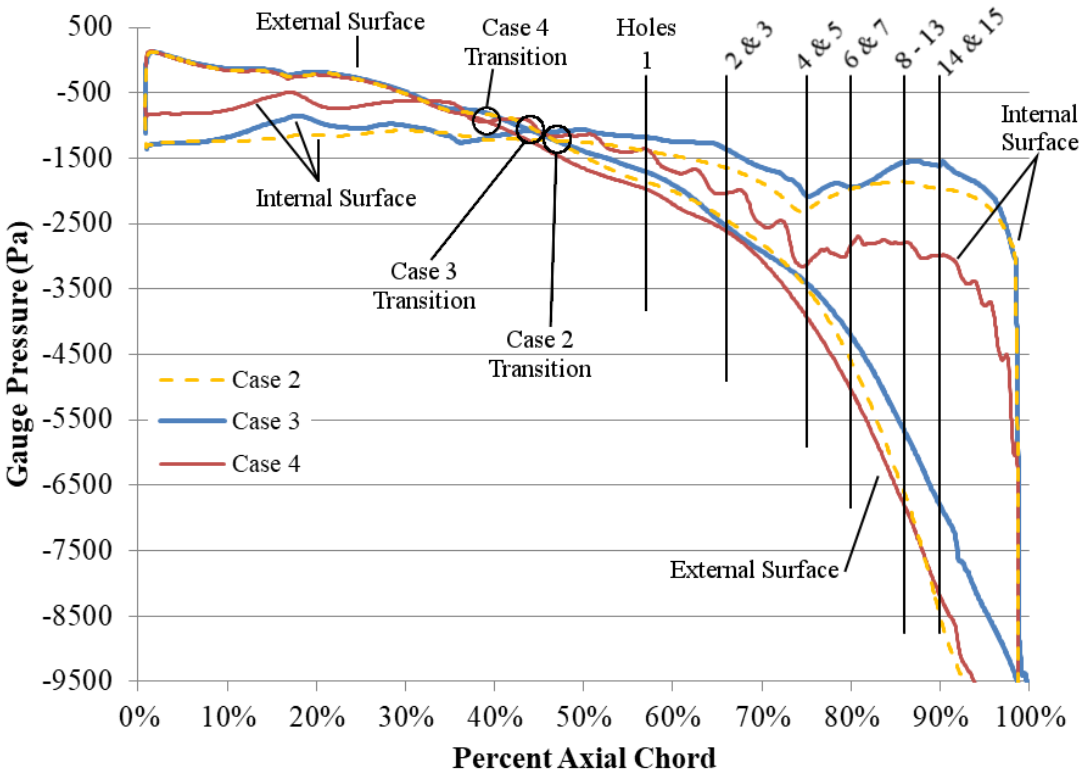

Figure 81. Surface Pressure Distributions

While the coolant holes were positioned in locations with a favorable pressure gradient, the coolant flow through each hole remains important to quantify for future cooling scheme development. Using FLUENT, a bounded plane was created for each cooling hole which intersected the hole walls and allowed the mass flow, velocity, and density of the fluid through the hole to be measured. For Case 3, the coolant mass flow rate increased with downstream distance from 0.0032 g/s at Hole 1 to 0.0157 g/s at Hole 15, consistent with the increase in pressure differential with axial distance. These flow rates were converted to a blowing ratio, M, using the velocity and density of the fluid exit the cooling holes, the freestream velocity and density, and Equation 24:

$$M = \frac{\rho_c V_c}{\rho_\infty V_\infty} \tag{24}$$

where ρ_c is the coolant density, V_c is the coolant velocity, ρ_∞ is the freestream density, and V_∞ is the freestream velocity. The blowing ratio for the holes in this scheme were between 0.64 and 1.1, as shown in Table 13. According to Bogard [17] the coolant for cylindrical holes is most effective at a blowing ratio of 0.6, and at 0.85 the effectiveness of the coolant drops off. The high values indicate the coolant jet needs to be slowed, which can be done by increasing hole diameter or shaping the hole [37].

Table 13. Coolant Hole Blowing Ratios

Hole	Percent Axial Chord	Percent Radial Span	Case 3 Blowing Ratio	Case 4 Blowing Ratio
1	57%	87%	0.66	0.62
2	66%	87%	0.64	0.44
3	66%	60%	0.85	0.68
4	75%	87%	0.65	0.45
5	75%	60%	0.75	0.54
6	80%	87%	0.69	0.67
7	80%	60%	0.80	0.94
8	86%	87%	0.74	0.60
9	86%	82%	0.96	0.73
10	86%	76%	1.03	0.80
11	86%	70%	1.07	0.86
12	86%	64%	0.93	0.97
13	86%	60%	1.10	0.84
14	90%	87%	0.81	0.73
15	90%	60%	0.85	0.89

The pins in Case 4 caused a 15% decrease in coolant mass flow entering the leading edge. This along with the decreased pressure differential resulted in a reduced mass flow and blowing ratio through the cooling holes. The minimum mass flow was 0.0017 g/s at Hole 2 while the maximum was 0.0138 g/s at Hole 15, a 55% and 12% reduction, respectively. The blowing ratios for Case 4 can also be found in Table 13 and ranged from 0.44 to 0.97. Of note was that no effort was made to advantageously position holes with respect to the pins. As a consequence, the holes at 87% radial span sat within the wake region of a pin. This explains the nominal 16% decrease in blowing

ratios out of holes at 87% radial span as opposed to the 10% decrease in blowing ratio out of holes at 66% radial span.

The overall effectiveness for each case was calculated using Equation 9 and are displayed in Figure 82. The surface temperatures, T_s, were coupled with a coolant temperature, T_{ci}, of 300 K and a freestream temperature, T_∞, of 2200 K taken from the peak temperature seen within the CC. The resulting contours from Case 3 and Case 4 were compared with the Case 1 and Case 2 results obtained by Bohan et al. [31]. Case 1 was evaluated to have a minimum overall effectiveness of 0.61 correlating to a peak surface temperature of 1035 K located below the CC. The incorporation of an internal passage, plug, and trailing edge slot for Case 2 resulted in the minimum overall effectiveness increasing to 0.64, which corresponds to a peak surface temperature of 990 K. While Case 2 has a lower peak temperature and an overall cooler surface, both Cases 1 and 2 have a hot streak which extends downstream starting at the CC. As the hot streak progresses it tapers toward the hub while approximately maintaining a 60% radial span.

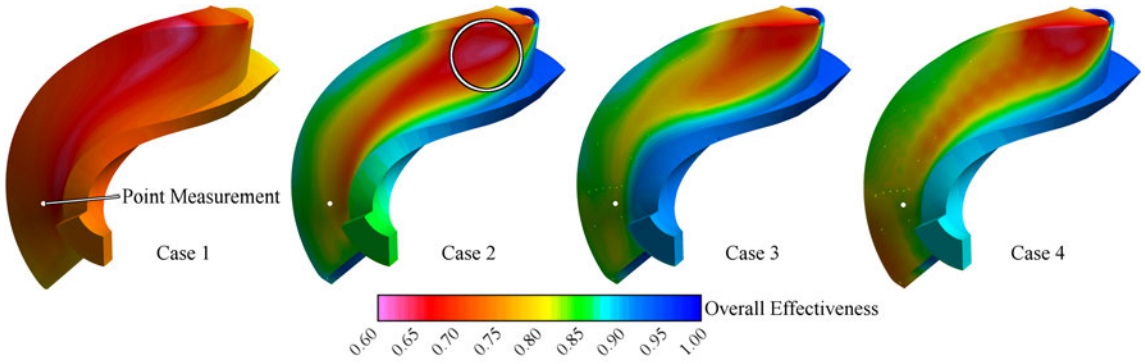

Figure 82. Vane Overall Effectiveness Contours For Each Case

Case 3 experienced a minimum overall effectiveness of 0.65, corresponding to a peak surface temperature of 956 K, which is a reduction from both Cases 1 and 2. When compared to Case 2 the vane surface axially under the CC, indicated by the

circle in Figure 82, looked almost identical, however the incorporation of cooling holes broke up the hot streak from the CC where it did not extend past 80% axial chord. After 86% axial chord the vane surface was close to a uniform temperature from the hub to the tip, which was different from Case 2 where the tip was cooler than the hub.

Case 4 displayed a minimum overall effectiveness of 0.63, corresponding to a maximum surface temperature of 1007 K, at the vane edge within the combustion cavity. This maximum surface temperature was a 3% decrease from Case 1, but a 5% increase from Case 3. These changes are insignificant and within a region where the pins do not connect to the surface. The impact of the internal structure was witnessed in the region of the hot streak. The hot streak present in Cases 2 and 3 can still be seen in Case 4, as shown in Figure 82. Although this streak extends further axially in Case 4 than Case 3, the temperature of the streak in Case 4 was reduced when compared to Case 2. The reduced temperatures was a result of the additional conduction paths introduced by the pins. This allowed the suction surface of the vane to transfer heat through the interior plug to the pressure side of the vane, increasing the surface temperature of the pressure side which also reduced the thermal stresses in the part.

The pins also acted as pin fins, transferring heat to the coolant internally, thus raising the average coolant temperature at the trailing edge slot. The coolant in all three cases entered the vane at 300 K. Cases 2 and 3 had an average coolant exit temperature of 412 K and 411 K, respectively. However, Case 4 had an average coolant exit temperature of 490 K, a 19% increase. This phenomenon was also noticeable in the overall effectiveness profile for Case 4, shown in Figure 83. The contours have a scalloped shape around the pins where the overall effectiveness at the location of the pin was greater than the surrounding area. The contour and the increased coolant exit temperature shows the pins are pulling heat away from the surface more effectively

and transferring this heat into the coolant. Overall, the temperature profile could be smoothed by relocating the cooling holes in between pins within the hot streak. This would increase the coolant released in that region and thus protect the surface from the hot combustion gases and reduce the heat transfer into the vane.

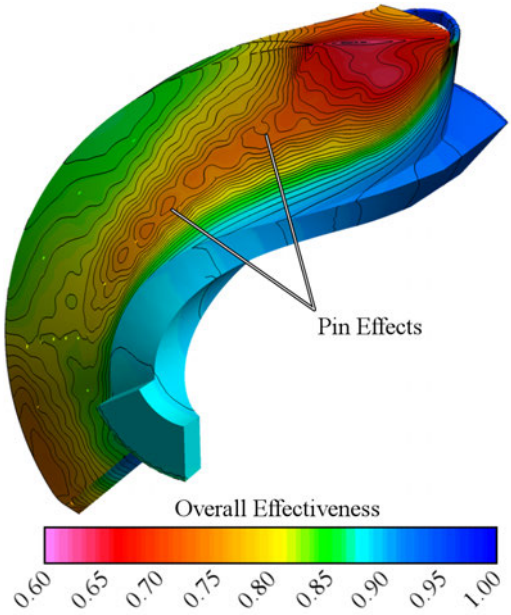

Figure 83. Vane Overall Effectiveness Contour For Case 4

The temperature and overall effectiveness for each case was measured at 88% axial chord and 64% radial span, indicated in Figure 82, as a point comparison of each case and is displayed in Table 14. This point is located near the vane trailing edge and 2% axial chord downstream of Hole 12. As expected Case 1 had the highest temperature at this point and lowest overall effectiveness of 878 K and 0.70, respectively. The internally cooled vane, Case 2, reduced this point's temperature by 21% to 697 K, or a 0.79 overall effectiveness. Incorporating the cooling holes in Case 3 further reduced the point's temperature to 631 K, a 28% reduction from Case 1. Case 4 had a surface temperature of 630 K, or 0.83 overall effectiveness, at the same point, which was comparable to the Case 3 value, but a 28% and 10% reduction compared to Cases 1

and 2, respectively. Clearly the presence of internal cooling had a more substantial impact than the coolant holes, while the incorporation of the internal pins had little to no impact on the overall effectiveness at this point location.

Table 14. Cooling Configuration Impact

88% Axial Chord and 64% Radial Span

Case	Overall Effectiveness	Temperature (K)
1	0.70	878
2	0.79	697
3	0.83	631
4	0.83	630

What the pins did was provide a more distributed heat load, as shown by the heat flux profile for Cases 3 and 4 in Figure 84. For interrogation purposes, the vane surface can be split into two regions, as indicated in the figure. Region 1 contained the outer holes and within this region both cases showed a similar heat flux of around $4{\cdot}10^4$ W/m^2. The difference between the two cases was experienced within Region 2. Here, Case 3 showed significant gradients while Case 4 shows these gradients have smooth by a factor of two. Within Region 2 high heat flux values were found in the region corresponding to the low overall effectiveness region shown in Figure 82. This is most likely a result of both the highly turbulent nature and the localized completion of reactions of the flow exiting the CC. Using the thermal conductivity of stainless steel as 16.3 W/m·K, the 1.27 cm surface thickness of the vane, and Equation 12 a Biot number range for the two cases were calculated. For both cases, the Biot number was between 0 and 0.10 aft of 50% axial chord.

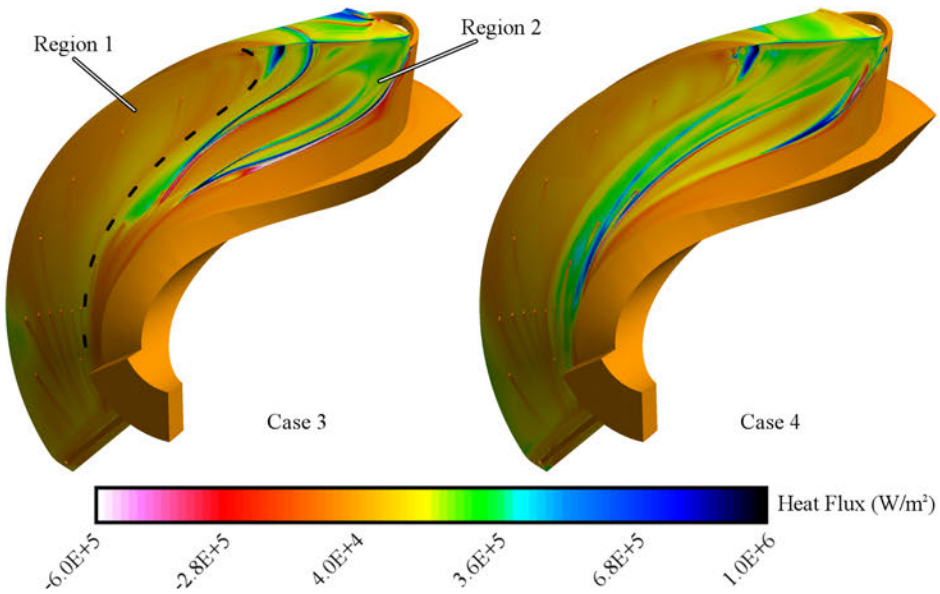

Figure 84. Vane Heat Flux Contours

On the vane surface downstream of the coolant holes a decrease in heat flux was revealed, as shown in Figure 85. The coolant exiting the holes reduced the heat transferred to the vane surface, however the holes were not shaped, and thus their effects were discreet. The incorporation of shaped holes would improve the coolant distribution and further reduce the heat transferred to the vane surface.

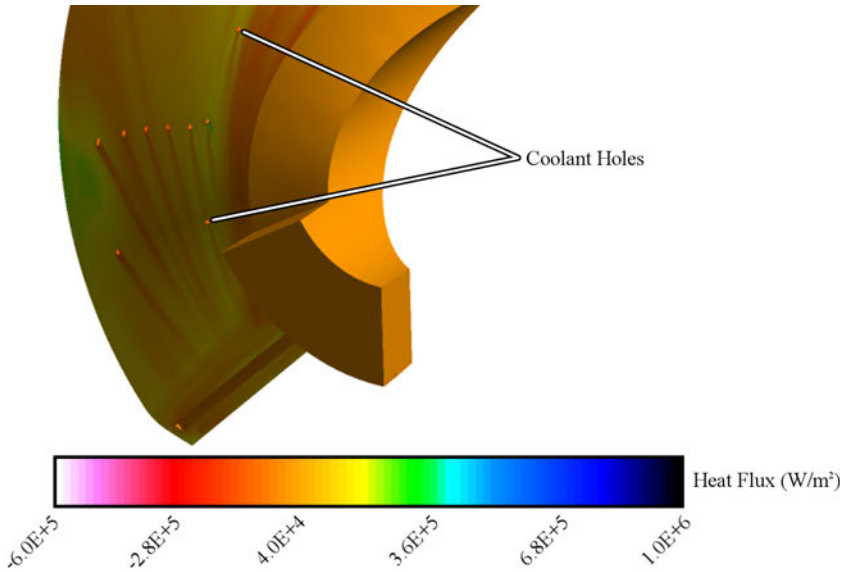

Figure 85. Coolant Hole Effects on Vane Heat Flux Contours

The results of this chapter completed the third, and final objective of this research. A cooled HGV which allows multiple cooling schemes to be evaluated was designed. For manufacturing, the design required an internal support structure to support the vane surface and prevent deformation. Multiple support designs were attempted and the part was successfully manufactured using an internal support structure which consisted of an array of 2 mm diameter pins spaced 3 mm apart. The part was then evaluated using CFD to determine the effects of the internal structure on the ability of the design to cool the vane surface. It was determined that while the pins decreased the coolant mass flow through the part by 15%, the pressure transition point shifted from 45% to 35% axial length and the heat loading on the vane surface was reduced.

5.3 Experimental Setup

The computational evaluation showed that the designed film cooled HGV accomplished its goal of reducing the surface temperature of the HGV. The next step to fully complete the goal of integrating a film cooled HGV into the UCC was to experimentally evaluate the manufactured part. The manufactured HGV discussed in Section 5.1 was prepared for experimental IR thermography evaluation by incorporating static pressure taps and thermocouple channels into each cooled vane, as shown in Figure 86. The pressure tap was 1.59 mm in diameter and included on each internally cooled vane to measure the internal pressure 15.88 mm axially from the trailing edge of the HGV. This axial position was selected to make sure the tap was not within the CC or covered by the back plate. The thermocouple channels were both 0.51 mm in diameter and created using electrical discharge machining at 11.90 mm and 4.19 mm axially from the trailing edge of the HGV. These positions were selected to guarantee their visibility to the IR camera. The channels were angled such that they broke through only a portion of the vane surface and ended abruptly at 90% and 60% span,

respectively. This put the thermocouple bead in contact with the surface where half was within the channel and half exposed to the flow.

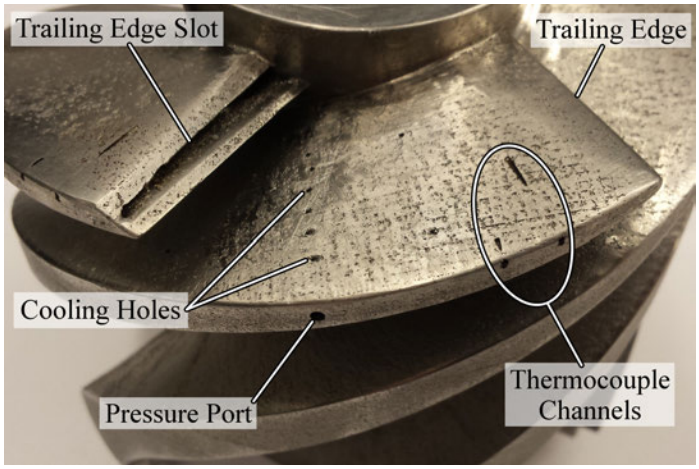

Figure 86. HGV Instrumentation Ports

The vane surface temperature profile was planned to be investigated with the IR thermography setup shown in Figure 87. To do this, the HGV was first painted with a high emissivity flat black paint, obtaining an emissivity close to unity. The vane was also instrumented with twelve K-type thermocouples, two embedded in the channels on each vane surface, were installed to correlate the IR image to a surface temperature. To capture the IR emission, a FLIR SC6700 IR camera was used with an internal bypass filter allowing emission within the 3774 nm to 4040 nm range. The filter allowed the camera to look through any flame that may be over the HGV surface. To protect the camera, the vane was viewed through a 63.5 mm diameter window. The window was 2 mm thick and made of uncoated sapphire due to its high transmissivity within the IR range. The recorded surface emission was then correlated with the twelve embedded thermocouples using the MATLAB code in Appendix A to produce surface temperature profiles which accounted for gas and window transmissivity. These components and this setup allow the film cooled HGV to be accurately evaluated using IR thermography in future studies.

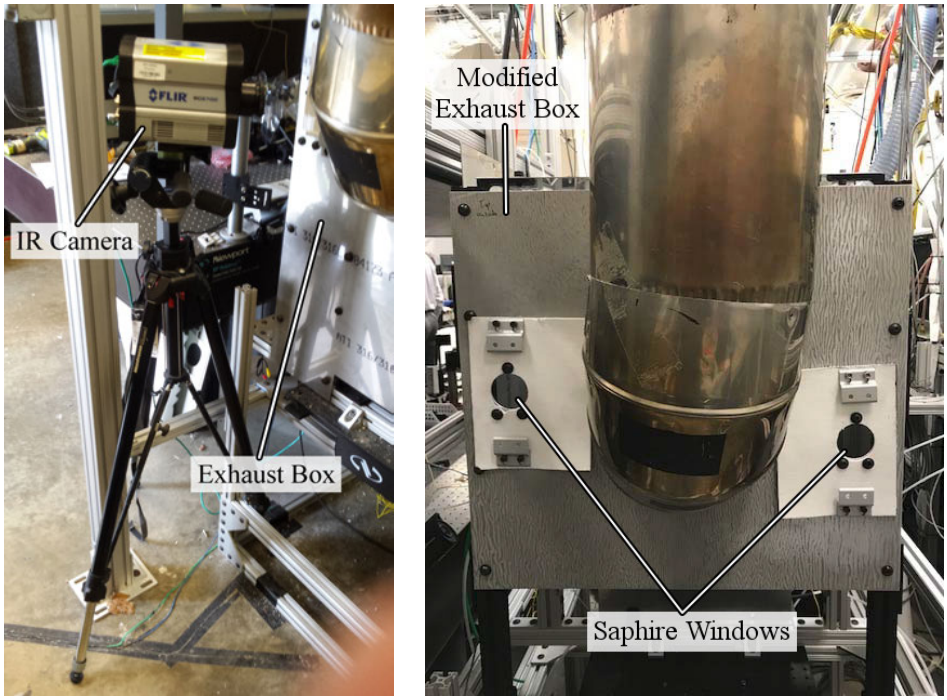

(a) IR Camera (b) Modified Exhaust Box

Figure 87. IR Thermography Setup

VI. Conclusions

This thesis explored three major aspects of a UCC, including flow dynamics, control, and film cooling. The first objective was to explore the modification of combustor components to change the flow dynamics within the CC. Components which constructed the CC were redesigned to modify the introduction of air and fuel in an aim to improve mixing of the reactants. The redesign also aimed to increase the bulk tangential velocity and the combustion stability of the UCC. The modifications to the UCC allowed increased control over the flow through the UCC and optimum flow splits and locations were identified. Therefore, the second objective was to generate an operating map which allowed understanding of the effects of different UCC control settings on the combustor's performance. The final objective explored was the design and manufacturing of a novel film cooling technique. This design is necessary for progressing UCC research from atmospheric to pressurized combustion. Without a film cooling design, the increased exit temperatures would melt the downstream components. This study reviewed the effects of manufacturing on the flow dynamics of a film cooled HGV.

6.1 Cavity Redesign Conclusions and Recommendations

Initial testing of the previous outer ring design, which consisted of radial fuel injection, revealed extensive fuel build up along the outer diameter and a reduction of bulk tangential velocity. The outer ring was redesigned to modify the flow dynamics, improving both mixing and centrifugal loading within CC. The redesigned outer ring, referred to as the 6-Step Ring, incorporated six backward facing steps which acted as tangential fluid injectors, aimed to increase the bulk velocity while also introducing air along the outer diameter. Due to the incorporation of fluid injectors in every backward

facing step, no recirculation regions were present within the cavity to anchor a flame and thus the combustion dynamics were undesirable. A second design, referred to as the 12-Step Ring, was designed which added a second set of six steps to act to produce a recirculation region, and thus stabilize combustion. The 12-Step design was evaluated first using CFD where results showed a 262% increase in centrifugal loading compared to the baseline design. This enabled a higher centrifugal loading of 1867 g's and therefore greater combustion rates, which is a benefit for a HGC [4]. The 12-Step Ring was then additively manufactured for experimental testing.

The performance of the 12-Step Ring was analyzed experimentally over cavity equivalence ratios from 0.72 to 1.73 and total air mass flow rates ranging from 0.056 kg/s to 0.120 kg/s. To evaluate the performance of the design, cavity and exit temperatures were recorded and compared to the baseline design. At a 74% core and 26% cavity airflow split as previously tested with the baseline design, the 12-Step Ring displayed undesirable cavity temperatures and reduced flame stability. Adjusting to an 80% core and 20% cavity airflow split resulted in both sustained combustion and a performance increase when compared to the baseline design. The 12-Step Ring was able to maintain high combustion stability and efficiency over a large range of cavity equivalence ratios from 0.12 to 1.73. This range represents a vast improvement over the stock design which operated mainly with a cavity equivalence ratio between 0.72 and 1.3. This allows for more overall fuel to be burned enabling higher overall equivalence ratios and thus higher exit temperatures to be achieved. With the rich cavity equivalence ratios, this design had the added benefit of lower cavity temperatures thus allowing for better life of this component. The 12-Step Ring cavity temperatures were found to be lower than the stock design, however the exit planes not only exhibited a 7% to 40% increase in average temperature, but they also had more desirable pattern factors ranging from 0.27 to 0.49, a 34% to 60% reduction from the previous design.

Overall the effects of the 12-Step design were beneficial to the performance of the UCC, however additional evaluation of the fluid dynamics and combustion event are recommended. The tangential velocity within the cavity needs to be experimentally measured using a flow visualization technique, such as particle streak emission velocimetry. This will confirm the centrifugal loading predicted in CFD. Then, the mapping and understanding of the combustion event within the cavity is recommended. The CFD results showed high temperature gradients within the CC which are difficult to measure and quantify experimentally using thermocouple point measurements. Therefore, a back plate should be constructed which gives full annular optical access to the CC, allowing the full combustion event to be mapped using techniques such as chemiluminescence or thin filament pyrometry. Results from these tests would reveal the flame front and cavity temperature profile providing more information on the cavity dynamics.

6.2 UCC Control Conclusions and Recommendations

The incorporation of the variable diffuser, 12-Step Ring, and new back plate allowed a new level of control over the performance of the UCC never before examined. The variable diffuser and 12-Step Ring allowed control over airflow percentages. The variable diffuser allowed control over the airflow percent between the core and cavity flow and the independent control of air injected through the outer ring allowed manipulation of the percent of the cavity airflow through the front plate and outer ring. The independent fuel control of the 12-Step Ring allowed control over the percent of fuel through the two step types. The incorporation of fuel inlets on the back plate allowed control over the percentage of total fuel introduced through the outer ring and back plate. These control parameters were examined to build an operating profile of the cavity. This led to an understanding of which controls provided the most

efficient overall fuel burn, highest exit temperatures, and desired pattern factors.

The operating map was tested at a 0.36 global equivalence ratio and total air mass flow rates from 0.60 kg/s to 0.120 kg/s and showed there was a region where the diffuser was unable to obtain the necessary flow condition and a region where flameout occurred. The limit of control from the variable diffuser was seen to be dictated by total airflow, cavity airflow, and combustion acoustics. It is theorized that because the diffuser operates on a pressure balance the cavity flow dynamics impact the diffuser range by back pressuring the front air driver plate holes. The flameout region was seen to be controlled by the air mass flow rate through the outer ring, where flameout occurred when this amount was greater than 9% of the total air mass flow rate through the entire UCC.

Evaluating the effects of controlling the fuel flow splits was done in two separate tests. The first test studied a range of total fuel percent through each step type. This revealed that the fuel split between the steps had little effect on the exit temperature. The next test repeated the operating map with a percentage of the total fuel injected through the back plate. These results showed various trends depending on the total mass flow rate.

At a 0.120 kg/s mass flow rate, the operating range of the UCC was at its minimum no matter the percentage of fuel injected through the back plate, although as it increased so did the exit temperatures by a nominal 7%. Decreasing the total air mass flow rate to 0.108 kg/s increased the operating range when no fuel was being injected through the back plate. However, with 10% and 20% of the fuel entering the cavity through the back plate, the operating range reduced to a size comparable to the 0.120 kg/s cases. Increasing the fuel flow through the back plate to 30% opens the operating range back up to what was seen with 0% back plate fuel flow with a nominal 11% increase in exit temperatures. Decreasing the total air mass flow rate

to 0.060 kg/s without back plate fuel flow reduced the operating range. Increasing to 10% fuel through the back plate resulted in the peak exit temperatures seen across all cases and opened the operating range to what was seen at a 0.108 kg/s total air mass flow rate with 0% and 30% fuel through the back plate. The size of the operating range stays constant as the back plate fuel is increased further, however the exit temperatures decrease by about 2%. These results show that at a 0.36 global equivalence ratio a 0.60 kg/s total air mass flow rate with 10% of the fuel injected through the back plate produces the widest operating range with the highest exit temperatures, with the peak temperature at 1006 K.

Future research in evaluating the acoustic characteristics and Rayleigh losses of the UCC operating points is necessary. Quantifying the acoustic characteristics and levels is necessary to develop a better understanding of their effects on the diffuser control. Measuring the pressure change through the device would allow verification that increasing the fuel flow through the back plate resulted in increased combustion within the HGV causing high Rayleigh losses. Both results would also aid in determining the preferred operating points for the UCC where both the acoustic levels and Rayleigh losses are minimized while the exit temperature is maximized.

6.3 Film Cooling Conclusions and Recommendations

The position of the HGV relative to the circumferential cavity allowed a novel technique for film cooling which did not require the additional ducting traditionally found within axial gas turbine engines. With this technique, the compressor exit flow was ingested at the leading edge of the HGV to be used as coolant, while the combustion products entered further downstream. The first step in this design was to control the amount of flow entering and exiting the vane to enable a high mass flow through the part while enabling the pressure inside the vane to rise above the

pressure outside the vane. This enables a favorable pressure gradient for film cooling to be applied to the external surface.

The complex shape and interior passages of the HGV required this coolant scheme to be additively manufactured. Ideally, the internal coolant passage would be hollow to minimize the pressure drop and allow coolant to be released onto the airfoil surface as soon as possible. Manufacturing requirements called for an internal support structure to prevent the HGV from deforming during production. Multiple design iterations for an internal support structure were evaluated for their ability to prevent part deformation while minimizing internal blockage. The final design selected consisted of a matrix of pins 2 mm in diameter and spread 3 mm apart.

A numerical evaluation was conducted to determine the effects of the internal pin structure on the coolant flow dynamics and effectiveness. The analysis included coupled fluid flow and chemical reactions to accurately model conjugate heat transfer within the vane. Several properties including pressure distributions, overall effectiveness, and blowing ratios were compared for three separate vane cooling arrangements to understand how the coolant could be distributed. Building off a previous study conducted by Bohan et al. [31], the locations of the cooling holes were more advantageously located. Comparisons showed a reduction in peak surface temperatures and hot steaks with the implementation of coolant holes after 50% axial chord. These holes also had little effect on the pressure distribution along the vane suction surface and coolant flowed out of each hole with a blowing ratio between 0.64 and 1.1.

The pins also played a role in the heat transfer within the part and affected the pressure drop through the part. The pressure differential between the external and internal flows was reduced which caused a 15% drop in the mass flow through the part. This resulted in a nominal 14% decrease in the blowing ratio. However the transition point of the pressure differential moved forward from 45% to 35% axial chord. This

indicates that coolant holes could be incorporated further upstream when the internal pins were in place. These additional cooling holes would be beneficial at breaking up the hot streak seen in the overall effectiveness profile which started at the CC and traveled downstream along the vane. By controlling the location of the coolant holes, the high heat transfer regions could be mitigated.

The current cooling scheme was developed to understand what was possible, and the results are promising. The next step will be to experimentally evaluate the film cooled HGV using IR thermography to evaluate the surface temperature and static pressure ports to evaluate the internal pressure. Once experimentally validated, an improved scheme could be developed that controls the heat distribution on the vane surface. More traditional design rules and tools can be applied to tailor the coolant. The high blowing ratios can be reduced by increasing the coolant hole diameters and shaped holes can be incorporated to keep the coolant jet closer to the surface. The low blowing ratios can be increased by adjusting hole diameters and strategically positioning the pins such that cooling holes are not in the wake region of a pin. These changes along with targeted hole placement would further increase the effectiveness of the cooling scheme which has the potential to cool the HGV for pressurized combustion. Overall, this novel concept of drawing in coolant directly into the vane leading edge shows promise as a new control feature. This concept specifically has application for the UCC configuration. It also opens the door to other locations in an engine where a similar scheme could be implemented.

Appendix A. IR Thermography Correlation Code

The recorded IR images was correlated to surface temperature using a MATLAB script which takes the output ".csv" files from the ExamineIR program, which controlled the IR camera, and produced surface temperature profiles. The script was saved with two additional files, shown in Figure 88: a text file, which dictated the colorbar colors for the output surface temperature profile, and an Excel file, which contained the pixel location of the thermocouples on the recorded IR images. Before running the script the thermocouple locations were saved in Excel, as shown in Figure 89. These locations corresponded to the pixel location, obtained through ExaminIR, of the thermocouple bead on the vane surface. Additional thermocouples were added by thermocouple number in Column A, X pixel location in Column B, and Y pixel location in Column C.

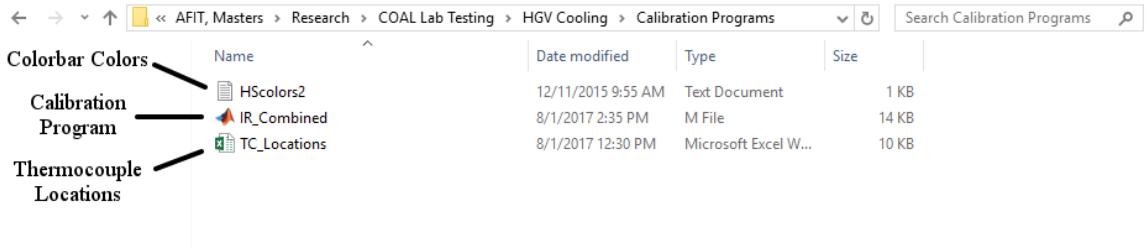

Figure 88. IR Correlation Code Save Folder

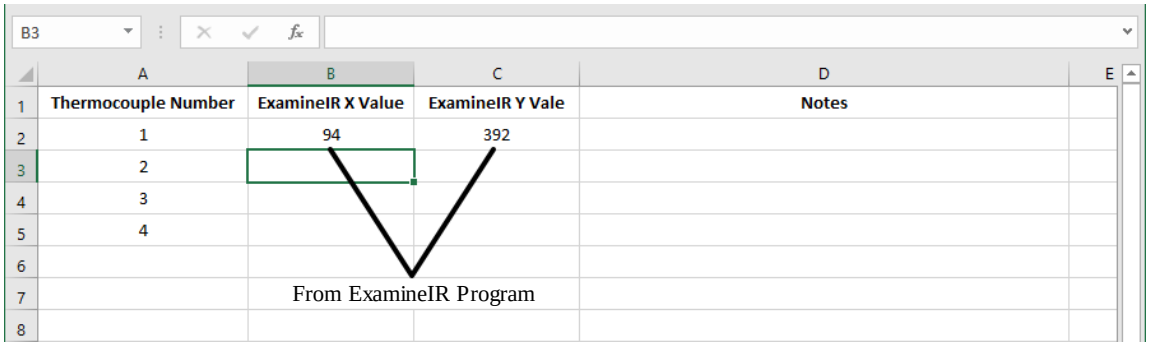

Figure 89. File For Surface Thermocouple Locations

The final step before running the MATLAB script was to save the average temperature for each surface thermocouple in an Excel file, as shown in Figure 90. The thermocouple number or name was input in Row 1 with the ability to add additional thermocouples. The values for each case were averaged from the recorded temperatures output by LabView, and saved in the appropriate row and column, where the row corresponded to the test case. The temperature units used in this file were the same as the output surface temperature profiles.

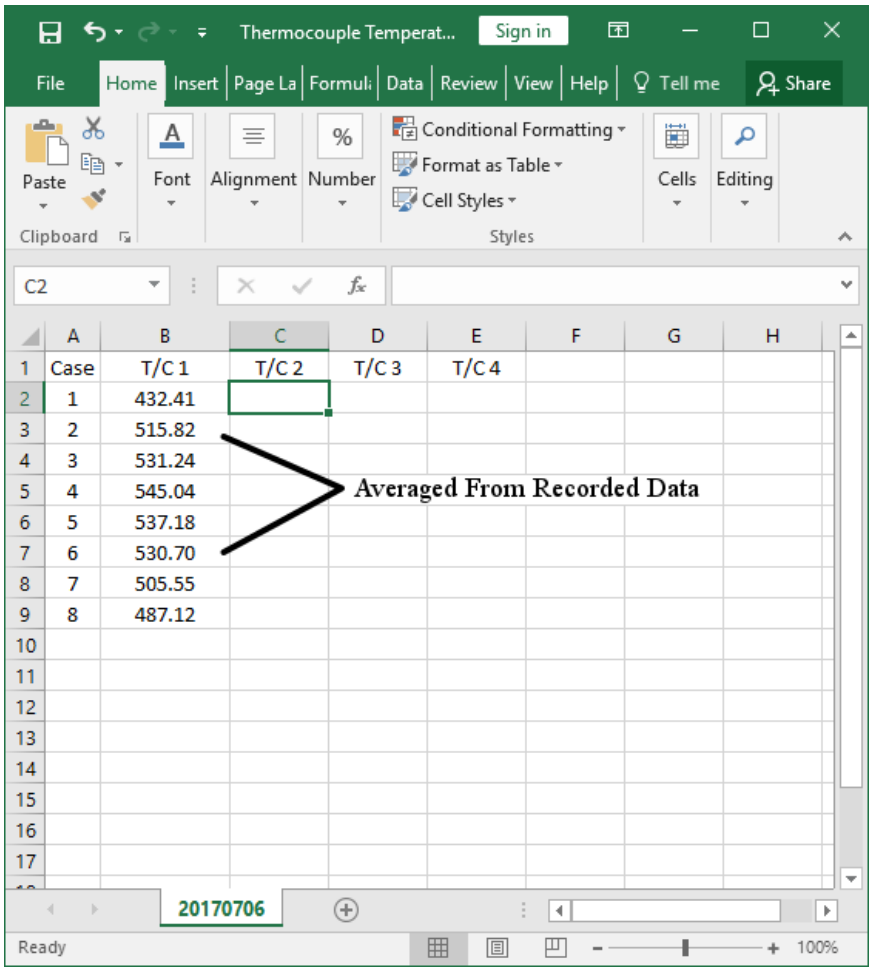

	A	B	C	D	E	F	G	H
1	Case	T/C 1	T/C 2	T/C 3	T/C 4			
2	1	432.41						
3	2	515.82						
4	3	531.24						
5	4	545.04						
6	5	537.18						
7	6	530.70						
8	7	505.55						
9	8	487.12						
10								
11								
12								
13								
14								
15								
16								
17								

Figure 90. File For Surface Thermocouple Temperatures

Once the thermocouple locations and temperatures were saved, the MATLAB script was ran and walked the user through the correlation process. The first section

of the program took the ".csv" file for each frame of the IR recordings and averaged them to a single file for each test case. The code for this section was as follows:

```
% The IR movie captured is split into frames using ExamineIR and saved
% as individual .csv files. These files need to be found and the first
% one selected.

% Prompt user for amount of test cases to calibrate by
prompt = 'Number of test cases to evaluate:';
dlg_title = 'Number of Test Cases';
num_cases = str2num(char(inputdlg(prompt,dlg_title,1,{'7'})));

% Check that the user entered a number
check = 0;
while check ~= 1;
if isempty(num_cases)
prompt = ['Entry was not a number.' sprintf('\n')...
'Number of test cases to evaluate:'];
num_cases = str2num(char(inputdlg(prompt,dlg_title,1,{'7'})));
else
check = 1;
end
end

% Loop for each case
for n=1:num_cases                              % (n)

% Stores path and name of the file selected
[File,Path]=uigetfile('*.csv','First IR File');

% Sets home path where averaged file is stored
HomePath=pwd;
cd(Path);
ParentPath=cd(cd('..'));

% Gather each file for that test
% Determines the common core through specified delimiter
CoreName=strtok(File,'_');
% List of all files in directory
TotalFileList=dir([CoreName '*.csv']);
% Counts number of .csv files to average
TotalFiles=length(TotalFileList);

% Determine number of files per case
% Get file name without file extension through delimiter '.'
PointCore=strtok(File,'.');
% Cut off delimiter '.'
PointCore=PointCore(1:end-1);
% All files for the case
PointList=dir(['*' PointCore '*.csv']);
% The number of files for the case
FilesPerPoint=length(PointList);
% Number of files to average
```

```
NumPoints=round(TotalFiles/FilesPerPoint);

% Assess size of image array
% reads the data in the the first file into matrix 'sample')
Sample=dlmread([Path File],',',52,0);
% Obtains the number of rows and columns of the sample
[Rows,Cols]=size(Sample);

% Read in files for every point, average, and write to new .csv file
% Loop from 1 through number of files to average (m)
for m=1:NumPoints
% Preallocate data variable, creates a matrix 'PointData'
% of dimensions (X,rows,colums)
PointData=NaN(FilesPerPoint,Rows,Cols);
% Loop through each file in the case
for j=1:FilesPerPoint
% Reads the data in the file into the matrix
PointData(j,:,:)=dlmread(TotalFileList(FilesPerPoint*(m-1)+j).name,...
',',52,0);
% End for loop through each file in the case (j)
end

% Average the single files
% Preallocate Matrix (1,Rows,Columns)
PointAvg=NaN(Rows,Cols);
% For loop over all rows (j)
for j=1:Rows
% For loop over all columns (k)
for k=1:Cols
% Averages all values at position (:,j,k)
PointAvg(j,k)=mean(PointData(:,j,k));
% End for loop over all columns (k)
end
% End for loop over all rows (j)
end

% Save the new averaged .csv file into parent directory of original
% selected file
% Cut off last 7 characters of core name
CoreName = CoreName(1:end-7);
% Convert current case number to a string for file naming
number = num2str(n);
csvwrite([ParentPath '\' CoreName '_' num2str(n) '.csv'],PointAvg);

% End for loop over number of files to average (m)
end
% End for loop over all cases (n)
end

% Inform the user all files have been averaged
waitfor(msgbox(['All ' num2str(num_cases) ' cases have been...
averaged.'],'Averaging Complete'));
```

First, the program asked the user for the number of test cases being evaluated. This then prompted the user to selected the "First IR File" which was the first ".csv" file of the first test case. As shown in Figure 91, the user navigated to the first case and selected the first ."csv" file. This process was repeated for each case until all cases have been selected and a completion dialogue box popped up.

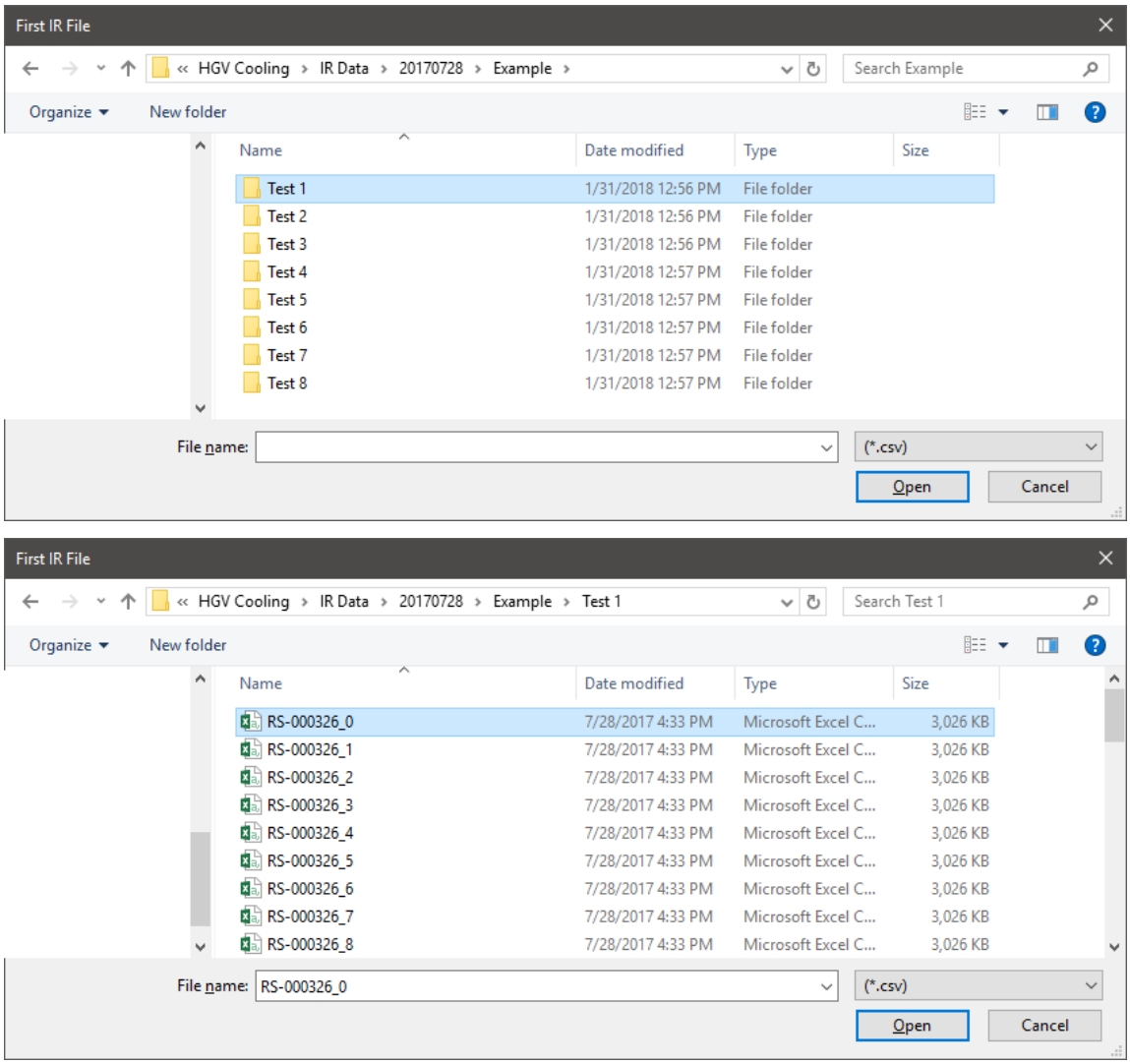

Figure 91. Selecting The First IR File

At this point the first section of the program was complete and a ".csv" file containing the average values for each case created and saved. The next step of the

program was to create the calibration curves using the surface thermocouple locations and temperatures. This section was as follows:

```
% A calibration curve for the camera and test environment must be
% constructed to convert the counts viewed by the camera into 2D
% temperature profiles.  This requires thermocouple locations and
% measured values.  The thermocouple values are read into the program
% via a user specified Excel file while the thermocouple locations are
% input through the Excel file labeled 'TC_Locations.xlsx'.

% Prompt user for desired prefix for saved files
prompt = 'Desired file prefix:';
dlg_title = 'Desire File Prefix';
prefix = inputdlg(prompt,dlg_title,1);
prefix = prefix{:};

% Prompt user for amount of thermocouples to calibrate by
prompt = 'Number of thermocouples:';
dlg_title = 'Number of Thermocouples';
num_TCs = str2num(char(inputdlg(prompt,dlg_title,1,{'1'})));

% Check that the user entered a number
check = 0;
while check ~= 1;
if isempty(num_TCs)
prompt = ['Entry was not a number.' sprintf('\n') 'Number of...
thermocouples:'];
num_TCs = str2num(char(inputdlg(prompt,dlg_title,1,{'1'})));
else
check = 1;
end
end

% Read thermocouple locations from Excel titled 'TC_Locations.xlsx'
range = ['B2:C' num2str(num_TCs+1)];
TC_loc = fliplr(xlsread([WrkSpc '\TC_Locations.xlsx'], range));

% Locate the data file
alphabet = 'ABCDEFGHIJKLMNOPQRSTUVWXYZ';
% Build range to read based off number of cases and thermocouples
range = ['B2:' alphabet(num_TCs+1) num2str(num_cases+1)];
% Stores path and name of the file selected
[File,Path]=uigetfile('*.xlsx','Data File',ParentPath);
% Read in the above selected Excel file
Data=xlsread([Path File], range);

% Locate the average .csv file created from the last section
% Stores path and name of the file selected
[File,Path]=uigetfile('*.csv','First Averaged IR File',ParentPath);
% Read in the above selected file as a sample
RepIR=csvread([Path File]);
[Rows,Cols]=size(RepIR);
clear RepIR;
```

```
% Sets home path where averaged file is stored
HomePath=pwd;
cd(Path);

% Read IR data
% Reads in all the averaged .csv files into a structure
FileList=dir('RS*.csv*');
% Determines the number of csv files: Y
NumPoints=length(FileList);
% Preallocats a matrix for the averaged files
IR=NaN(Rows,Cols,NumPoints);

% Import the data from all the averaged .csv files
% Loop over all averaged .csv files (n)
for n=1:NumPoints

% Generate file name
% Pull up file n from the FileList structure
File = FileList(n,1);
File = File.name;
% Split up file name in common core (Start) and individual part
% (Rest) including the ascending number
[Start,Rest]=strtok(File,'_');
% Cutting of the ascending number of the Rest of the file name
[Rest,End]=strtok(Rest,'-');
Rest;
End = '.csv';

% Generating the file name to be read in, names consists of common
% core (Start), ascending number (n) and individual rest (End)
IRFile=[Start '_' num2str(n) End];

% Read in data from the file
IR(:,:,n)=flipud(csvread([Path IRFile]));
% End for loop over all averaged .csv files (n)
end

% Find the average radiation intensity immediately around the
% thermocouple
% Prealocate matrix for the intensities
Intensity=NaN(num_TCs,NumPoints);
% Loop over all averaged .csv files (n)
for n=1:NumPoints
% Loop over number of thermocouples
for m=1:num_TCs
TCRow=TC_loc(m,1);
TCCol=TC_loc(m,2);
TCR(m,n)=TCRow;
TCC(m,n)=TCCol;

% Average the surrounding pixels
Intensity(m,n)=mean(mean(IR(TCRow-6:TCRow+6,TCCol-6:TCCol+6,n)));

% End for loop over number of thermocouples
end
% End for loop over all averaged .csv files (n)
```

```
end

% Find temperatures corresponding to the IR intensities
Temps=[Data(1:NumPoints)]';

% Save data with specified file prefix
save([prefix 'CalData.mat'],'Intensity','Temps');

% Develop calibration using all points, regardless of TC location
fo = fitoptions('Method','NonlinearLeastSquares');
ft = fittype('a*x^.25+b','options',fo);

% Develop curve fit
% Loop over all thermocouples (n)
for n=1:num_TCs
Temp(:,n)=[Temps(n,:)]';
Intens(:,n)=[Intensity(n,:)]';
% End for loop over all thermocouples (n)
end
% Fit a curve to the temperature and intensity values
[curve,gof]=fit(Intens,Temp,ft);

% Plot TC data (T^4) and curve fit vs. intensity
figure('name', 'Temperature Vs. Counts')
hold on;
plot(Intens,Temp,'k*');

% Sort temps to give appropriate curve shape
Intens=sort(Intens);
Curve=curve.a*Intens.^.25+curve.b;

plot(Intens,Curve,'-b');
Str1=['All TC''s'];
Str2=['Curve Fit'];
legend(Str1,Str2,'Location','northwest');
ylabel('T');
xlabel('Counts');

% Create textbox with curve fit equation
StrT=['T = ' num2str(curve.a) 'I^0^.^2^5 + ' num2str(curve.b)];

Str3={StrT,['R^2 = ' num2str(gof.rsquare)]};
dim=[.4,.2,.1,.1];
annotation('textbox',dim,'String',Str3,'EdgeColor','none');

% Save figure
FigFile=['AllTCCalibration.fig'];
savefig(FigFile);

% Compare individual calibrations
figure('name', 'Temperature^4 Vs. Counts')
hold on;
for n=1:num_TCs
scatter(Intensity(n,:),Temps(n,:).^4);
Legend{n} = strcat('TC', num2str(n));
end
```

```
plot(Intens,Curve.^4,'-b');
legend([Legend, 'Curve Fit'],'Location','northwest');
ylabel('T^4');
xlabel('Counts');

% Create textbox with curve fit equation
annotation('textbox',dim,'String',Str3,'EdgeColor','none');

% Save figure and curve fit
savefig('AllTCcalibration-IndivPts.fig');
save([prefix 'CalCurve.mat'],'curve','gof');
cd(HomePath);

% Inform the user a calibration curve has been created and is complete
waitfor(msgbox('Calibration curve created.', 'Calibration Completed'));
```

The user was first prompted to input a desired prefix for the output files and the number of thermocouples on the surface, which corresponded to the number of thermocouples in the Excel position and temperature files. From here, the user was prompted to select the Excel file containing the average thermocouple temperatures and the first averaged ".csv" file from the first section of the code, which was named "RS_1.csv". Using the thermocouple temperatures and the averaged ".csv" file, which contained the averaged count value for each pixel, the program them created a correlation curve, shown in Figure 92.

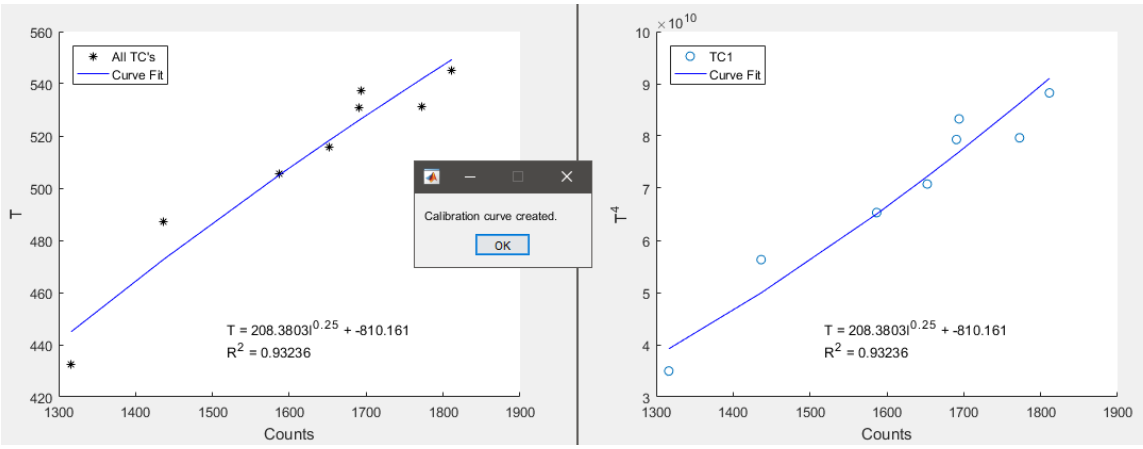

Figure 92. IR Correlation Curve

The correlation was then used to convert the IR image recorded by the camera in counts to the surface temperature profile. The program conducted this conversion using the following code:

```
% The program will now use the calibration curve generated in the
% previous section to convert the 2D counts profile to a 2D
% temperature profile for each case averaged in the first section.

% Load colorbar color scheme
ColorMap=(dlmread([WrkSpc '\HScolors2.txt']));

% User selects the first averaged .csv file
[File,Path]=uigetfile('*.csv','First Averaged IR File');
counts=csvread([Path File]);
Size=size(counts);
HomePath=pwd;
cd(Path);

% The program searches for the other averaged .csv files
IRFiles=dir([strtok(File,'_') '*.csv']);
NumPts=length(IRFiles);

% Calibration data
A=curve.a;
B=curve.b;

% Pixel size of IR image
x = [1:1:size(Sample,1)];
% Pixel size of IR image
y = [1:1:size(Sample,2)];

% Filename core
Core=strtok(File,'_');

% Loop over each case (n)
for n=1:num_cases

% Read in IR intensity data starting with case 1
File=[Core '_' num2str(n) '.csv'];
counts=rot90(flipud(csvread(File)));

% Trim off high counts (Large white areas) due to paint flaking
for i=1:432
for j=1:512
if counts(i,j)> 2500
counts(i,j) = 2500;
else
end
end
end

% Calculate temp based on measured intensity and calibration curve
```

```
T = A*counts.^(.25)+B;

% Display profiles
figure('Name', ['Case ' num2str(n) ' Intensity Profile'])
colormap(ColorMap);
contourf(x,y,counts,25);
axis('equal');
colorbar
savefig(['Case_' num2str(n) '_Counts_Profile.fig']);

figure('Name', ['Case ' num2str(n) ' Temperature Profile'])
colormap(ColorMap);
contourf(x,y,T,25);
axis('equal');
colorbar
savefig(['Case_' num2str(n) '_Temp_Profile.fig']);

% Save workspace values of importance
save(['Case_' num2str(n) '_Values.mat'],'counts','T','x','y');

% Save temperature to a .csv file
csvwrite(['Temp' '_' num2str(n) '.csv'],T);

% Clear looped workspace values
clear counts T

% End for loop over each case (n)
end
```

This final section of the program output both the profile contoured as counts and surface temperature, shown in Figure 93. The figures, along with the calibration curves, were also saved, as shown in Figure 94, for future use. Modifications of this section of code were were done including varying the number of contour lines on the resulting profiles and adding in a section to remove over-saturation. The over-saturation section, commented as "Trim off high counts", was added to account for white spots appearing on the counts image, resulting in loss of details in the final profile. The white spots were caused by the high temperature paint inadequately adhering to the vane surface resulting in portions to flake off. This could have been prevented with better surface preparation and the use of a primer before applying the high temperature paint.

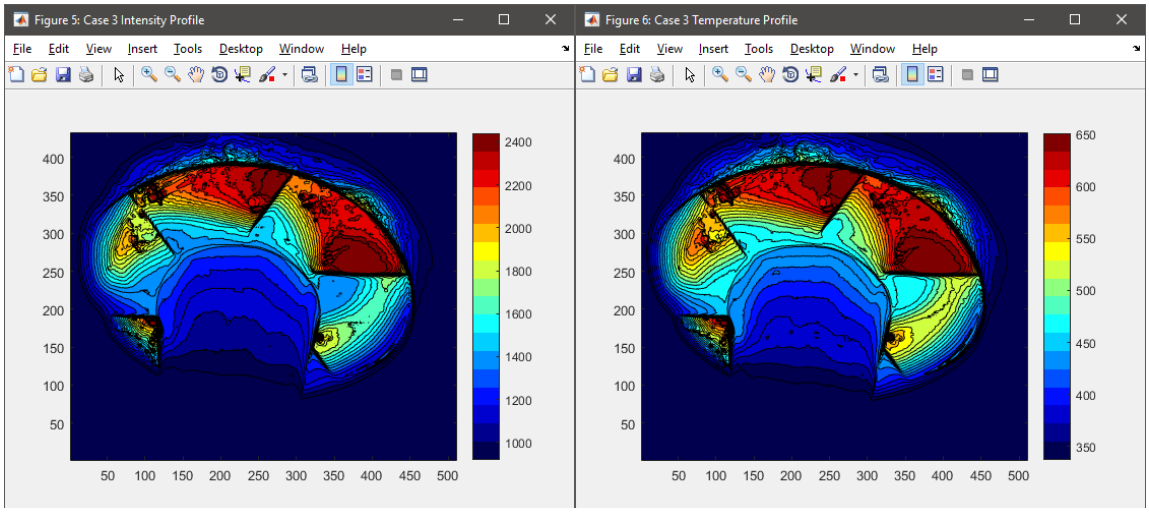

Figure 93. Output Profiles

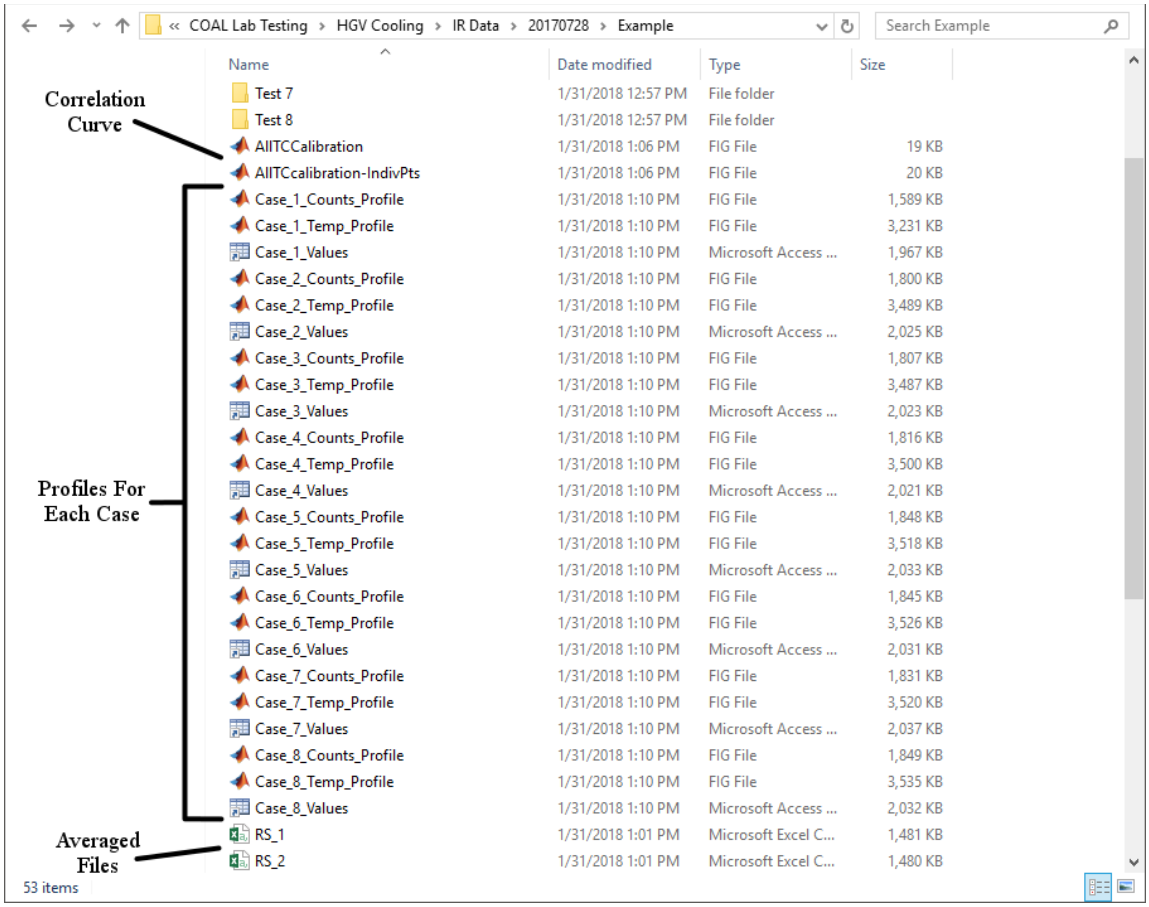

Figure 94. Output Files

Bibliography

1. Bohan, B. T., *Analysis of Flow Migration in an Ultra Compact Combustor*, Master's thesis, Air Force Institute of Technology, WPAFB, OH, 2011, AFIT/GAE/ENY/11-M02.

2. Lewis, G. D., "Swirling Flow Combustion - Fundamentals and Application," *Presented at AIAA/SAE 9th Propulsion Conference, Las Vegas, Nevada*, November 1973, AIAA Paper No. 73-1250.

3. Lewis, G. D., "Centrifugal-Force Effects on Combustion," *Symposium (International) on Combustion, Vol. 14, pp 413-419*, January 1973.

4. Briones, A. M., Sekar, B., and Erdmann, T., "Effect of Centrifugal Force on Turbulent Premixed Flames," *Journal of Engineering for Gas Turbines and Power*, Vol. 137, 2015, 011501-1.

5. Cottle, A. E., *Flow Field Dynamics in a High-g Ultra-Compact Combustor*, Ph.D. thesis, Air Force Institute of Technology, WPAFB, OH, 2016, AFIT-ENY-DS-16-S-057.

6. Turns, S. R., *An Introduction to Combustion*, McGraw-Hill, Inc, New York, 2012, 3rd Edition.

7. Mattingly, J. D., Heiser, W. H., and Pratt, D., *Aircraft Engine Design*, AIAA, Reston, Virginia, 2nd ed., 2002.

8. Hsu, K. Y., Goss, L. P., and Roquemore, W. M., "Characteristics of a Trapped-Vortex Combustor," *Journal of Propulsion and Power, Vol. 14, No. 1, pp 57-65*, January- February 1998.

9. Cottle, A. E., Polanka, M. D., Goss, L. P., and Goss, C. Z., "Investigation of Air Injection and Cavity Size Within a Circumferential Combustor to Increase G-Load and Residence Time," *ASME Journal of Engineering for Gas Turbines and Power*, 2017, 140(1): 011501-011501-12. doi:10.1115/1.4037578.

10. Zelina, J., Sturgess, G. J., and Shouse, D. T., "The Behavior of an Ultra-Compact Combustor (UCC) Based on Centrifugally-Enhanced Turbulent Burning Rates," *40th AIAA/ASME/SAE/ASEE Joint Propulsion Conference and Exhibit, Fort Lauderdale, FL*, July 2004, AIAA 2004-3541.

11. Williams, G. C., "Basic Studies on Flame Stabilization," *Journal of the Aeronautical Sciences, Vol. 16, No. 12, pp 714-722*, 1949.

12. Driscoll, J. F. and Temme, J., "Role of Swirl in Flame Stabilization," *49th AIAA Aerospace Sciences Meeting, Orlando, FL*, January 2011, AIAA-2011-108.

13. Lapsa, A. P. and Dahm, W. J. A., "Experimental Study on the Effects of Large Centrifugal Forces on Step-Stabilized Flames," *Proceedings of the 5th US Combustion Meeting, San Diego, CA*, 2007, H14.

14. Lapsa, A. P. and Dahm, W. J. A., "Hyperacceleration effects on turbulent combustion in premixed step-stabilized flames," *Proceedings of the Combustion Institute*, Vol. 32, 2009, pp. 1731–1738.

15. Bogard, D. G. and Thole, K. A., "Gas Turbine Film Cooling," *Journal of Propulsion and Power*, Vol. 22, March-April 2006, pp. 249–270.

16. Dittmar, J., Schulz, A., and Wittig, S., "Assessment of Various Film Cooling Configurations Including Shaped Holes and Compound Angle Holes Based on Large Scale Experiments," *Proceedings of ASME Turbo Expo 2002, June 3-6, 2002, Amsterdam, The Netherlands*, 2002, GT-2002-30176.

17. Bogard, D. G., "Airfoil Film Cooling," *The Gas Turbine Handbook*, National Energy Technology Laboratory, Department of Energy, Morgantown, WV, 2006, Sect. 4.2.2.1.

18. ASTM. 2010 F2792-10e1 Standard Terminology for Additive Manufacturing Technologies. American Society for Testing and Materials International.

19. Hofland, E. C., Baran, I., and Wismeijer, D. A., "Correlation of Process Parameters with Mechanical Properties of Laser Sintered PA12 Parts," *Advances in Materials Science and Engineering*, February 2017, pp 1-11.

20. Martiny, M., Schiele, R., Gritsch, M., and Wittig, S., "In Situ Calibration for Quantitative Infrared Thermography," *Quantitative InfraRed Thermography Journal, Vol. 96, pp 3-8*, June 1996, 99-GT-142.

21. Schulz, A., "Infrared Thermography as Applied to Film Cooling of Gas Turbine Components," *Measurement Science and Technology, Vol. 11, pp 948-956*, February 2000.

22. Ochs, M., Horbach, T., Schulz, A., Koch, R., and Bauer, H.-J., "A Novel Calibration Method for an Infrared Thermography System Applied to Heat Transfer Experiments," *Measurement Science and Technology, Vol. 20, No. 7*, June 2009, 075103.

23. Adrian, R. J., "Twenty Years of Particle Image Velocimetry," *Experiments in Fluids, Vol. 39, pp 159-169*, 2005.

24. Parks, A. K., *Desensitizing Flame Structure and Exhaust Emissions to Flow Parameters in an Ultra-Compact Combustor*, Master's thesis, Air Force Institute of Technology, WPAFB, OH, 2012, AFIT/GAE/ENY/12-M33.

25. Wilson, J. D., *Characterizing G-Loading, Swirl Direction, and Rayleigh Losses in an Ultra Compact Combustor*, Master's thesis, Air Force Institute of Technology, WPAFB, OH, 2013, AFIT-ENY-13-S-02.

26. Bohan, B. T., Polanka, M. D., and Goss, L. P., "Development and Testing of a Variable Geometry Diffuser in an Ultra-Compact Combustor," *Proceedings of AIAA SciTech 2017, Grapevine, TX*, 2017, AIAA 2017-0777.

27. Wilson, J. D. and Polanka, M. D., "Reduction of Rayleigh Losses in a High G-Loaded Ultra Compact Combustor," *Proceedings of the ASME Turbo Expo 2013*, 2013, GT2013-94795.

28. Samuelsen, S., "Conventional Type Combustion," *The Gas Turbine Handbook*, U.S. Department of Energy, Office of Fossil Energy, Nathional Energy Technology Laboratory, DOE/NETL-2006-1230, 2006.

29. Barringer, M., Thole, K., and Polanka, M., "Effects of Combustor Exit Profiles on High Pressure Turbine Vane Aerodynamics and Heat Transfer," *Proceedings of the ASME Turbo Expo 2006*, 2006, GT2006-90277.

30. Bills, J. D., *Liquid Fuel Film Cooling: A CFD Analysis With Hydrocarbon Fuel*, Master's thesis, Air Force Institute of Technology, WPAFB, OH, 2016, AFIT/GAE/ENY/16-M-199.

31. Bohan, B. T., Polanka, M. D., and Rutledge, J. L., "Computational Analysis of a novel cooling scheme for Ultra Compact Combustor Turbine Vanes," *Proceedings of the ASME Turbo Expo 2017: Turbine Technical Conference & Exposition, Charlotte, NC*, 2017, GT2017-63319.

32. Bohan, B. T., Polanka, M. D., and Goss, L. P., "Measurement of Temperature, Pressure, Velocity, and Frequency in an Ultra Compact Combustor," *56th AIAA Aerospace Sciences Meeting, SciTech Forum, Kissimmee, FL*, 2018.

33. Mattingly, J. D., Heiser, W. H., and Daley, D. H., *Aircraft Engine Design*, AIAA, Washington D.C., 1987.

34. Briones, A. M., Burrus, D., Erdmann, T., and Shouse, D. T., "Effect of Centrifugal Force on the Performance of High-G Ultra Compact Combustor," *Proceedings of ASME Turbo Expo, Montreal, Canada*, 2015, GT2015-43445.

35. Cottle, A. E. and Polanka, M. D., "Numerical and Experimental Results From a Common-Source High-G Ultra-Compact Combustor," *Proceedings of the ASME Turbo Expo 2016*, 2016, GT2016-56215.

36. FLUENT® Inc., *FLUENT 16.2 User's Guide*, 2016.

37. Gritsch, M., Schulz, A., and Wittig, S., "Adiabatic Wall Effectiveness Measurements of Film-Cooling Holes With Expanded Exits," *Journal of Turbomachinery*, Vol. 120, July 1998, pp. 549–556.

REPORT DOCUMENTATION PAGE

Form Approved
OMB No. 0704–0188

1. REPORT DATE *(DD–MM–YYYY)*	2. REPORT TYPE	3. DATES COVERED *(From — To)*
22-03-2018	Master's Thesis	August 2016 — March 2018

4. TITLE AND SUBTITLE

CONTROL, CHARACTERIZATION, AND COOLING OF AN ULTRA-COMPACT COMBUSTOR

5a. CONTRACT NUMBER

5b. GRANT NUMBER

5c. PROGRAM ELEMENT NUMBER

6. AUTHOR(S)

Kevin J. DeMarco, 2d Lt, USAF

5d. PROJECT NUMBER

5e. TASK NUMBER

5f. WORK UNIT NUMBER

7. PERFORMING ORGANIZATION NAME(S) AND ADDRESS(ES)

Air Force Institute of Technology
Graduate School of Engineering and Management (AFIT/EN)
2950 Hobson Way
WPAFB OH 45433-7765

8. PERFORMING ORGANIZATION REPORT NUMBER

AFIT-ENY-MS-18-M-250

9. SPONSORING / MONITORING AGENCY NAME(S) AND ADDRESS(ES)

Air Force Research Lab
Dr. Andrew Caswell
1790 Loop Road
Wright-Patterson AFB, OH 45433
andrew.caswell.4@us.af.mil

Air Force Office of Scientific Research
Dr. Chiping Li
875 North Randolph Street
Arlington, VA 22203
chiping.li@us.af.mil

10. SPONSOR/MONITOR'S ACRONYM(S)

AFRL, AFOSR

11. SPONSOR/MONITOR'S REPORT NUMBER(S)

12. DISTRIBUTION / AVAILABILITY STATEMENT

DISTRIBUTION STATEMENT A:
APPROVED FOR PUBLIC RELEASE; DISTRIBUTION UNLIMITED.

13. SUPPLEMENTARY NOTES

14. ABSTRACT

The outer ring and back plate of the Ultra-Compact Combustor (UCC) were redesigned to improve control of the fuel and air injection and subsequent mixing with the goal of maximizing the fuel burned within the combustion cavity. Evaluations using Computational Fluid Dynamics (CFD) were implemented to help guide the design and understand the combustion dynamics. The outer ring and back plate were then manufactured and tested to compare with the original design. These components allowed a new level of control over the UCC never before examined which was then characterized by developing an operating profile for the various controllable aspects. The redesign and unprecedented controllability allowed the UCC to operate at previously unobtainable equivalence ratios and produce a nominal 15% increase in exit temperatures. Similarly, CFD was utilized to guide the design of a film cooled hybrid guide vane which drew in compressor air at the stagnation region of the airfoil as the coolant. Using CFD the effects of the required internal supports on flow dynamics and cooling effectiveness were explored.

15. SUBJECT TERMS

Combustion, Combustor, Experimental, Computational, Ultra-Compact Combustor, Flame Stability, Film Cooling

16. SECURITY CLASSIFICATION OF:			17. LIMITATION OF ABSTRACT	18. NUMBER OF PAGES	19a. NAME OF RESPONSIBLE PERSON
a. REPORT	b. ABSTRACT	c. THIS PAGE			Dr. Marc Polanka, AFIT/ENY
U	U	U	U	157	19b. TELEPHONE NUMBER *(include area code)* (937) 255-3636, x4714; marc.polanka@afit.edu